REPORT DOCUMENTATION PAGE

Form Approved OMB NO. 0704-0188

1. REPORT DATE (DD-MM-YYYY)	2. REPORT TYPE	3. DATES COVERED (From - To)
26-10-2009	Final Report	1-Jul-2005 - 30-Jun-2009

4. TITLE AND SUBTITLE
NONSTANDARD AND HIGHER-ORDER FINITE-DIFFERENCE METHODS FOR ELECTROMAGNETICS

5a. CONTRACT NUMBER
W911NF-05-1-0292

5b. GRANT NUMBER

5c. PROGRAM ELEMENT NUMBER
611102

6. AUTHORS
Constantine A. Balanis, Bo Yang, Craig R. Birtcher

5d. PROJECT NUMBER

5e. TASK NUMBER

5f. WORK UNIT NUMBER

7. PERFORMING ORGANIZATION NAMES AND ADDRESSES
Arizona State University
Office of Research & Sponsored Projects Administration
Arizona State University
Tempe, AZ 85287 -3503

8. PERFORMING ORGANIZATION REPORT NUMBER

9. SPONSORING/MONITORING AGENCY NAME(S) AND ADDRESS(ES)
U.S. Army Research Office
P.O. Box 12211
Research Triangle Park, NC 27709-2211

10. SPONSOR/MONITOR'S ACRONYM(S)
ARO

11. SPONSOR/MONITOR'S REPORT NUMBER(S)
45747-EL.5

12. DISTRIBUTION AVAILIBILITY STATEMENT
Approved for Public Release; Distribution Unlimited

13. SUPPLEMENTARY NOTES
The views, opinions and/or findings contained in this report are those of the author(s) and should not contrued as an official Department of the Army position, policy or decision, unless so designated by other documentation.

14. ABSTRACT
The major objective of this dissertation is to design simple low-dispersion Finite-Difference Time-Domain (FDTD) methods for electromagnetics. Literature review indi-cated that the Nonstandard Finite Difference (NSFD) method exhibits great potentials in dispersion reduction. Different from the Standard Finite Difference (SFD) methods, the NSFD methods are derived directly based upon dispersion analysis. In this dissertation, the basic concepts of the NSFD methods are generalized to various extended finite-difference stencils. Furthermore, several improved NSFD

15. SUBJECT TERMS
Nonstand Finite Difference Methods, Finite-Difference Time-Domain, Higher Orders

16. SECURITY CLASSIFICATION OF:			17. LIMITATION OF ABSTRACT	15. NUMBER OF PAGES	19a. NAME OF RESPONSIBLE PERSON
a. REPORT	b. ABSTRACT	c. THIS PAGE			Constantine Balanis
UU	UU	UU	UU		19b. TELEPHONE NUMBER 480-965-3909

NONSTANDARD AND HIGHER-ORDER FINITE-DIFFERENCE METHODS FOR ELECTROMAGNETICS

by

Constantine A. Balanis
Bo Yang
Craig R. Birtcher

Department of Electrical Engineering
Arizona State University
Tempe, AZ 85287-5706

Funded by

Contract No. W911NF0510292

July 1, 2005 – June 30, 2009

U.S. Army Research Office

Research Triangle Park, NC

ABSTRACT

The major objective of this project is to design simple low-dispersion Finite-Difference Time-Domain (FDTD) methods for electromagnetics. Literature review indicated that the Nonstandard Finite Difference (NSFD) method exhibits great potentials in dispersion reduction. Different from the Standard Finite Difference (SFD) methods, the NSFD methods are derived directly based upon dispersion analysis. In this report, the basic concepts of the NSFD methods are generalized to various extended finite-difference stencils. Furthermore, several improved NSFD methods are presented based on the standard fourth-order stencil to mitigate the dispersion in multi-dimensional domains. The least square method is used to optimize the coefficients of the proposed stencils. Numerical simulations show that these schemes significantly reduce the dispersion error of their standard counterparts. Many technical issues in practical implementations, such as absorbing boundary conditions, stability conditions, and Gauss's Laws, are discussed and justified. Moreover, two special conditions are proposed for the extended stencils in the vicinity of the dielectric material discontinuities. It was demonstrated that the accuracy of the fourth-order stencil is fully restored by applying these conditions.

A very important electromagnetic interference (EMI) problem is also presented in this report. The problem concerns the effects of passengers on personal electronic device (PED) mutual coupling in a simplified Boeing 757 fuselage. The results predicted by FDTD are compared to the measurements performed in the Electro-Magnetic Anechoic Chamber (EMAC) of Arizona State University. It was found that the presence of the passengers significantly dampens the resonances in the fuselage, which lower the potential EMI threat to the on-board communication/navigation systems.

TABLE OF CONTENTS

Page

CHAPTER Page

CHAPTER Page

LIST OF TABLES

LIST OF FIGURES

Figure Page

Figure Page

Figure Page

CHAPTER 1

INTRODUCTION

Electromagnetic theory, one of the most important branches of physical science, studies the electric-magnetic fields generated by charges at rest or in motion (currents) [2]. The relations and variations between the electric-magnetic fields, charges and currents are governed by basic laws developed by a group of distinguished scientists: Faraday, Ampere, Gauss, Lenz, Coulomb, Gauss, Volta, and others. In 1873, Maxwell was able to mathematically combine these laws into a consistent set of vector equations, which are referred to as Maxwell's equations. The modern form of Maxwell's equations were formulated by Heaviside in the late 19th century [3]. Then Hertz completely validated the theory of Maxwell's by a series of experiments. Motivated by the practical applications, most importantly radar and wireless communications, electromagnetic theory has been developing for over 100 years. Today, electromagnetics has become an indispensable discipline of everyday life which covers a wide range of applications, such as antennas, scattering, microwave circuits and devices, radio-frequency and optical communications, broadcasting, geosciences and remote sensing, radar, radio astronomy, quantum electronics, solid state circuits and devices, eletromechanical energy conversion and computers.

Almost all electromagnetic phenomena can be well described by Maxwell's equations either in differential or integral forms, associated with appropriate boundary conditions. However, only a few canonical problems can be solved exactly. Closed-form solutions for most practical and complex electromagnetic problems are usually intractable. For example, some problems involve complex geometries that do not conform to any known orthogonal coordinate systems for which the scalar Helmholtz equation can be solved by the method of

the separation of variables. Also, many other problems may include nonlinear, anisotropic or dispersive materials. Consequently, many numerical methods have been developed to solve such problems.

With today's computer resources, numerical methods are drastically more efficient, if not the only way to solve complex practical electromagnetic problems. The most popular numerical methods include, high frequency asymptotic methods, Method of Moments (MoM), Finite Element Method (FEM) and Finite-Difference Time-Domain (FDTD) method, etc. Brief introductions to these methods follows.

High-frequency asymptotic methods use optical asymptotic techniques, such as Geometrical Optics (GO), Geometrical Theory of Diffraction (GTD), Physical Optics (PO), and Physical Theory of Diffraction (PTD). These methods calculate the incident, reflected and diffracted fields separately by introducing reflection and diffraction coefficients. The ultimate solution is a superposition of the contributions from each part. These methods provide physical insight into the radiation and scattering mechanisms and yield accurate results that compare well with the experiments. Pure high frequency methods are very useful in electrically large problems with simple materials, such as perfect electric conductor(PEC). However, these methods are usually more difficult to apply to complex geometries, especially those that involve complex materials. Thus, high-frequency asymptotic methods are usually hybridized with other numerical methods, such as MoM. An introduction to the methods can be found in [2].

Compared to the high-frequency asymptotic methods, MoM can handle objects of arbitrary geometries especially those of planar shapes. It casts the solution for the induced current density in the form of an integral equation, and expands the unknown quantity into

a set of basis functions. MoM has become popular since the pioneering work of Richmond and Harrington in 1960s. Since then, it has successfully solved a wide variety of practical electromagnetic problems, such as radiation from thin-wire antennas and scattering problems. However, MoM usually cannot easily deal with inhomogeneous and non-linear materials because of the difficulty to find the analytical Green's function. Details of the method can be found in [4].

FEM originates from material and structural analysis in mechanics and civil engineering. It was not used to solve practical electromagnetic problems until the late 1960s. The successfulness of FEM is due to its powerful capability to model general anisotropic, dispersive and nonlinear media. By volumetrically discretizing all space and transforming Maxwell's equations into a weak form of either the electric or magnetic field wave equation, FEM is able to solve more complex problems. The mathematical advantages of using the weak form of the wave equation are that its solutions do not have as restricted properties as the solutions of the standard wave equation. However, the method is not very efficient for electrically large problems because one has to solve an associated huge matrix system. More details about FEM can be found in [5].

Different from MoM and FEM, FDTD is a time-domain method. The currently standard FDTD method for electromagnetics was proposed by Yee in 1966 [6]. In Cartesian coordinates, both the time and space derivatives in Maxwell's equations in differential form are directly replaced by second-order central difference approximations. Moreover, Yee cleverly staggers the positions of the E and H fields to naturally model the physical curls of the fields. In the time domain, the leap-frog scheme is used to incrementally march the variation of the E and H fields. Despite the simplicity and elegance of Yee's algorithm, it

did not receive much interest immediately due to the inability to model an "open" problem and the lack of high performance computers. As the computational resources became more affordable, FDTD became more popular. Since the late 80s, the number of publications related to the FDTD method has experienced nearly exponential growth in [7]. Moreover, Berenger presented a Perfectly Matched Layer (PML) [8] – [9], which successfully truncated the simulation domain and increased the dynamic range of FDTD to more than 120 dB. Since then, FDTD has been extensively applied to almost every aspect of electromagnetics. As a numerical method, Yee's algorithm is explicit, robust and easy to implement. More importantly, Yee's algorithm is able to model more complex materials than any other numerical methods can do. However, this method suffers from dispersion errors which could contaminate the solutions with nonphysical artifacts. A comprehensive introduction on the Yee algorithm can be found in [10] – [14].

The continuous boost of the information industry during the last few decades has profoundly changed the daily life of everyone. The demands for better information products and services, such as high-definition televisions, the future wireless LAN, and the third-generation mobile communications, have been pushing the system operating frequency higher due to the following reasons [3]. First of all, the lower end of the electromagnetic spectrum are being rapidly depleted. The pursuit of higher bit rate, which requires more bandwidth, can only be achieved at higher frequencies. Secondly, the system miniaturization requires a smaller physical size of the antennas. However, the gain and bandwidth of an antenna are proportional to its electrical size. Therefore, high gain and bandwidth are only possible at a higher frequency. As a consequence of the general industry trend, the operating frequency will continuously increase.

A higher operating frequency means that the size of the platform that carries the devices, such as a mobile vehicle, a commercial or military aircraft, becomes electrically larger. This, however, presents challenges to the numerical methods due to the following:

- The simulations of the electrically large problems require to store vast, sometimes prohibitive, amount of variables in computer memories. For example, for the FDTD algorithms, the memory needed to store the electric and magnetic fields is proportional to the product of the number of cells in each direction ($N_x \times N_y \times N_z$).

- Even if one can afford the demand of the astonishing amount of memory, the execution time to run such a simulation for electrically large problems is extremely long.

- Even if one is patient enough to wait until the completion of the simulation, chances are the results are totally contaminated by the numerical errors, especially the phase errors due to the dispersion .

The currently standard FDTD algorithm (Yee's scheme) is only second-order accurate in both the space and time domains, and suffers from severe nonphysical dispersions. Based on many analytical analysis and numerical experiments [1], it has been found that a cell size of $\lambda/10 - \lambda/20$ provides acceptable accuracy for most problems with moderate electrical size. However, the phase errors generated by dispersion accumulate as the traveling distance of the wave and the simulation time increase. Consequently, for electrically large problems, this rule of thumb may not be valid since the accumulation of the phase errors due to the dispersion significantly deteriorate the accuracy. A simple way to reduce the dispersion errors is to use a finer mesh resolution. This yields an even larger simulation domain which aggravates the already heavy burden of the computer memory and CPU. In other

words, the available computer resources limit the electrical size of the problems that can be handled. Hence, the mesh refinement is not an efficient solution and sometimes not even an alternative.

In reality, the dispersion is one of the inherent characteristics related to the FDTD methods which cannot be completely eliminated. In order to minimize the dispersion, many alternative approaches were proposed. These methods, in the broadest sense, can be classified into two categories: the *Standard FDTD (SFD)* and the *Nonstandard FDTD (NSFD)*. The standard FDTD schemes are derived based upon the Taylor series expansion. The coefficients of the stencils are chosen to minimize the truncation error and maximize the order of accuracy. As a comparison, the nonstandard FDTD schemes consider the minimization of dispersion as the ultimate goal. Instead of using the Taylor series expansion, the coefficients of the NSFD stencils are derived directly from the dispersion relations.

Yee's algorithm is a typical standard FDTD scheme with second-order accuracy in both the time and space domains. Conventionally, an SFD method with Mth- and Nth-order accuracy in the time and space domains, respectively, is referred to as the FDTD(M,N) scheme. For example, Yee's algorithm can be also denoted as the FDTD(2,2) scheme. It is a natural consideration to attempt to reduce the dispersion by increasing the stencil's order of accuracy. In 1989, Fang presented a scheme which is second-order accurate in the time domain but fourth-order accurate in the space domain [15]. Fang's algorithm is also referred to as the FDTD(2,4) scheme. Since then, higher-order schemes quickly drew the attention of the FDTD researchers and became one of the most promising dispersion-reduction methods. Early exploration of Fang's algorithm and other high-order FDTD schemes includes [16]– [25]. A modified FDTD(2,4) scheme based on the integral form of

Maxwell's equations was introduced in [26], [27]. A second-order "isotropic" scheme using complex multi-dimensional stencils was proposed in [28]. Contributions in the time-domain discretization include: implicit time-integration schemes [29], [30] and higher-order time-integration schemes [31] – [32]. Some intuitive reviews and computational efficiency analysis of higher-order FDTD can be found in [33] – [36].

Another important type of method is the nonstandard FDTD (NSFD). The stencils of the NSFD may be similar to the stencils of the SFD. However, the NSFD coefficients are properly adjusted from their SFD counterparts for further dispersion reduction. Typically, the values of the NSFD coefficients are determined by the Fourier analysis based on the dispersion relation. The concept of the NSFD was first proposed by Mickens [37]. Applications of the NSFD in various mathematical and physical areas are summarized in [38], [39]. Cole did the pioneering work in applying the NSFD to solve the Maxwell's equations [40], [41]. To minimize the anisotropy of the NSFD for multi-dimensions, Cole proposed a complex stencil which is similar to the one used in [28]. Afterwards, the NSFD scheme is modified to be able to model the lossy and absorbing materials [42], [43]. A full dispersion and stability analysis for the 3D Cole's scheme can be found in [44], [45]. Furthermore, Cole's scheme is expanded to even more complex stencils and curvilinear coordinate systems in [46]– [52]. In order to reduce the average dispersion error without using the complex stencils, [53]– [55] uses dispersion centering technique originated in [1]. Then, a scheme that can control the dispersion level in a certain range of propagation angles was presented by introducing a filtering process [56], [57]. Although proposed independently by different research groups, [58]– [65] indicated that the dispersion error can be drastically reduced by using degenerated fourth-order stencils. That is, the coefficients of the fourth-order stencil are deliberately adjusted

to further reduce the dispersion. The cost is that the accuracy of the fourth-order stencil is degenerated to second-order. Comparisons of the dispersion properties of Cole's and other low-dispersion algorithms can be found in [66], [67].

In order to further decrease the dispersion error, the previously stated standard and nonstandard FDTD schemes both use extended stencils. The extended stencils represent those finite difference operators that involve more than two points. For example, Fang's FDTD(2,4) scheme is considered to be a simple extended stencil with four points. Typically, if more points are included into the stencil, more coefficients (degrees of freedom) can be used to mitigate the dispersion. The coefficients of the extended stencils can be derived using either the Taylor series expansion (SFD) or dispersion analysis (NSFD). In a homogeneous region, the schemes using the extended stencils work perfectly well. However, significant nonphysical errors will be generated at the material interface. These errors could be attributed to the field discontinuities along each side of the material interface. Many efforts have been devoted to restore the accuracy of the extended stencils across the material interface [68]– [71]. Moreover, a subgridding technique to hybridize the FDTD(2,2) and the FDTD(2,4) [72] – [76] was introduced. The FDTD(2,4) scheme is only used in the homogeneous regions. However, along the material interfaces and the domain boundaries, the FDTD(2,2) scheme is applied. Along the interface between the FDTD(2,2) and FDTD(2,4) domains, the fields are carefully coupled. This method does not require any special treatment for the material interface.

All of the conventional FDTD(2,2) truncation techniques, such as the PML, can be used without modifications. However, the hybrid scheme is still second-order accurate and the programming is cumbersome. Alternative approaches include the one-sided sten-

cils [77], [78]. The derivatives near the material interface are approximated using points only along one side of the interface. However, as reported in [77], the accuracy of the one-sided stencil degenerates quickly when the discontinuity is aggravated. Originated in [79], [80], a derivative matching method was proposed [81]. This method introduces fictitious points at both sides of the material interface and physically enforces the boundary conditions. Using this technique, consistent stencils can be applied throughout the entire domain. In [81], it has been shown that the accuracy of the schemes (up to eighth-order) are fully restored. Another method [82]– [84] is based on the Fourier analysis of the numerical reflection coefficient which is very similar as the derivation of the NSFD schemes. Although originally presented for Yee's algorithm, this method seems very promising for the extended stencils. Useful reviews on the state-of-art progresses in the extended stencil and the material interface treatments can be found in [85], [86].

It has been indicated that the dispersion can be reduced significantly by using the NSFD methods. However, the following technical issues still need to be considered.

- For multi-dimensional problems, the NSFD schemes still suffer from serious nonphysical anisotropic errors. Methods to decrease the anisotropy without significantly increasing the computational burden are still highly desired.

- The current available approaches to determine the values of the stencil coefficients become very cumbersome for more complex schemes. Simple approaches to solve the optimal coefficients are still needed.

- Some principal concerns for the NSFD algorithms, such as the Gauss's Law, have not been examined yet.

- The available techniques treating the material interface are far from practical. Ironically, it is usually much easier to design a very complex stencil than the corresponding interface conditions. Proper material interface conditions are still the greatest challenge in this area.

With the increase of the operating frequency, electromagnetic compatibility (EMC) and electromagnetic interference (EMI) issues become incrementally more important. One of the most critical EMI concern is that the aircraft navigation/communication antennas could be interfered by the radiation emission generated by on-board personal electronic devices (PEDs), such as cellphones, laptops, etc. That is the reason for switching off all the personal electronic devices during the take-off and landing, if not during the entire flight. This EMI issue has be studied by characterizing the mutual coupling between an on-board PED antenna and an aircraft antenna mounded on the exterior of a simplified Boeing 757 fuselage [72]. However, the fuselage cavity in the previous research was empty. In practice, the fuselage is always filled with various metallic frames, decoration materials and passengers. Among these materials, the human body could be the most important due to its highly dielectric and lossy property. The impact of the present passengers on the EMI characteristics still remains a question.

In this project, the major objective is to resolve or at least mitigate the aforementioned technical problems for the nonstandard FDTD methods. The passenger effects on the PED mutual coupling will also be examined. The structural organization of this report is now outlined. In Chapter 2, the fundamental principles of the electromagnetics will be first reviewed. Then the basic theory of the standard FDTD, including the FDTD(2,2) (Yee's)

and other higher-order schemes, will be presented. A detailed dispersion analysis, which forms the basis of the nonstandard FDTD, on various standard FDTD algorithms will also be discussed.

Chapter 3 is focused on the nonstandard FDTD. We will go through the fundamental of the one-dimensional NSFD algorithm. Dispersion analysis and numerical simulations will be presented to reveal the strength and weakness of the 1D NSFD. An NSFD(2,4) scheme will also be introduced by incorporating the concept of NSFD into the fourth-order stencil. The NSFD algorithms will then be extended to multi-dimensional cases. To reduce the average dispersion error, an improved NSFD algorithm will be presented. A simple least squares method will be used to determine the optimal stencil coefficients. Afterwards, the concept of the NSFD will be generalized. Dispersion analysis will be presented to demonstrate the performance of the generalized NSFD. Then, the Gauss's Laws in both the differential and integral forms will be examined for the NSFD algorithms. Finally, a material interface condition based on the concept of the NSFD will be proposed to decrease the errors caused by the material interface.

In Chapter 4, the passenger's effect on the PED mutual coupling will be investigated. The mutual coupling between the antennas is described by the *S*-parameters. A simplified passenger model was designed and built to fit into the fuselage model. The *S*-parameters will be simulated using the FDTD algorithm. To justify the simulations, same parameters are measured using the vector network analyzer in the electromagnetic anechoic chamber of Arizona State University. Finally, the *S*-parameters with and without passengers are compared to demonstrate the passenger's effect.

CHAPTER 2

THE STANDARD FINITE-DIFFERENCE METHODS

As indicated in the precious chapter, the Standard Finite-Difference Time-Domain Method (SFD) is an important type of FDTD schemes that is derived directly using the Taylor series expansion. The simplest SFD method, Yee's algorithm, is the currently most popular FDTD scheme that has been extensively applied to many electromagnetic boundary-value problems, for example, antenna modeling, radiation/scattering, microwave circuits design, and EMC/EMI analysis, etc. However, Yee's algorithm is only second-order accurate in both the time and space domain. Hence it suffers from severe dispersion error especially for the electrically larger problems. In order to reduce the dispersion error, one of the most promising methods is to use the higher-order SFD method (HOSFD). Usually, a central-difference space stencil using N points could achieve an order of accuracy up to N-th order. However, the accuracy of the entire scheme also depends on the time-domain discretization and the type of the problems. Moreover, due to the discontinuities of the fields, significant errors can be generated along the material interface which will deteriorate the accuracy of the entire HOSFD method to be similar as that of Yee's algorithm [85], [86]. Since increasing the number of points doses not achieve the desirable accuracy, many advances on the HOSFD only consider Fang's FDTD(2,4) scheme, which is second-order accurate in the time domain but fourth-order accurate in the space domain.

In this chapter, the fundamental principles of any numerical method, i.e. Maxwell's equations, will be first reviewed. Then the theory of Yee's algorithm will be introduced. A general procedure to derive the SFD stencils with high order of accuracy will follow. The stability conditions for the SFD methods will be discussed. Finally, a detailed dispersion

analysis for Yee's and Fang's algorithms, which are also the base of the nonstandard FDTD methods, will be presented.

2.1. Fundamental Principals

Time-varying electromagnetic phenomena are initial boundary-value problems. In a homogeneous region, these problems are fully described by Maxwell's equations. Along the material discontinuities, proper boundary conditions must be enforced. Maxwell's equations can be written either in differential or in integral form.

The differential form of Maxwell's equations is most widely used since it governs the relations between field vectors, current densities, and charge densities at any point in space at any time. For a homogeneous region, Maxwell's equations in differential form can be written as

$$\nabla \times \mathbf{E} = -\frac{\partial \mathbf{B}}{\partial t} - \mathbf{M}_c - \mathbf{M}_i \tag{2.1}$$

$$\nabla \times \mathbf{H} = \frac{\partial \mathbf{D}}{\partial t} + \mathbf{J}_c + \mathbf{J}_i \tag{2.2}$$

$$\nabla \cdot \mathbf{D} = q_e \tag{2.3}$$

$$\nabla \cdot \mathbf{B} = q_m \tag{2.4}$$

where $\mathbf{E}$ is the electric field intensity in (volts/meter), $\mathbf{H}$ is the magnetic field intensity in (amperes/meter), $\mathbf{D}$ is the electric flux density in (coulombs/square meter), $\mathbf{B}$ is the magnetic flux density in (webers/square meter), $\mathbf{J}_c$ and $\mathbf{J}_i$ are the conduction and impressed electric current densities, respectively, in (amperes/square meter), $\mathbf{M}_c$ and $\mathbf{M}_i$ are the conduction and impressed magnetic current densities, respectively, in (volts/square meter), q_e is the electric charge density in (coulombs/cubic meter), and q_m is the magnetic charge

density in (webers/cubic meter). Individually, (2.1)-(2.4) are also referred to as Faraday's Law, Ampere's Law, Gauss's Law for electric field, and Gauss's Law for magnetic field, after the names of their discoverers.

The integral form of Maxwell's equations describes relations of the field vectors, current densities, and charge densities over an extended region of space. The integral form of Maxwell's equations can be written as

$$\oint_C \mathbf{E} \cdot d\mathbf{l} = -\frac{\partial}{\partial t} \iint_S \mathbf{B} \cdot d\mathbf{s} - \iint_S \mathbf{M}_c \cdot d\mathbf{s} - \iint_S \mathbf{M}_i \cdot d\mathbf{s} \tag{2.5}$$

$$\oint_C \mathbf{H} \cdot d\mathbf{l} = \frac{\partial}{\partial t} \iint_S \mathbf{D} \cdot d\mathbf{s} + \iint_S \mathbf{J}_c \cdot d\mathbf{s} + \iint_S \mathbf{J}_i \cdot d\mathbf{s} \tag{2.6}$$

$$\oint_S \mathbf{D} \cdot d\mathbf{s} = Q_e \tag{2.7}$$

$$\oint_S \mathbf{B} \cdot d\mathbf{s} = Q_m \tag{2.8}$$

where Q_e and Q_m are the total electric and magnetic charges, respectively.

In materials with constitutive parameters that are independent of time, the electric and magnetic flux densities ($\mathbf{D}$ and $\mathbf{B}$) are related to the electric and magnetic field intensities $\mathbf{E}$ and $\mathbf{H}$ using the constitutive relations

$$\mathbf{D} = \epsilon \mathbf{E} \tag{2.9}$$

$$\mathbf{B} = \mu \mathbf{H} \tag{2.10}$$

where ϵ is the electrical permittivity of the medium in (Farad/meter) and μ is the magnetic permeability of the medium in (Henries/meter). For free space, ϵ and μ are constants which can be written as

$$\epsilon_0 = 8.854 \times 10^{-12} \quad (Farads/meter) \tag{2.11}$$

$$\mu_0 = 4\pi \times 10^{-7} \quad (Henries/meter) \tag{2.12}$$

Moreover, the conduction electric current density $\mathbf{J}_c$ and the conduction magnetic current density $\mathbf{M}_c$ are related to the electric and magnetic field intensities $\mathbf{E}$ and $\mathbf{H}$ using the Ohm's laws

$$\mathbf{J} = \sigma \mathbf{E} \tag{2.13}$$

$$\mathbf{M} = \sigma^* \mathbf{H} \tag{2.14}$$

where σ is the electrical conductivity in (Siemens/meter) and σ^* is the magnetic conductivity in (Ohms/meter).

In order to completely describe the electromagnetic phenomena, appropriate boundary conditions must be enforced along the interfaces where the media exhibit discontinuities. Assuming there are no sources present, along a interface formed by two media with electric properties (ϵ_1,μ_1) and (ϵ_2,μ_2), the boundary conditions can be expressed as

$$\hat{n} \times (\mathbf{E}_1 - \mathbf{E}_2) = 0 \tag{2.15}$$

$$\hat{n} \times (\mathbf{H}_1 - \mathbf{H}_2) = 0 \tag{2.16}$$

$$\hat{n} \cdot (\mathbf{D}_1 - \mathbf{D}_2) = 0 \tag{2.17}$$

$$\hat{n} \cdot (\mathbf{B}_1 - \mathbf{B}_2) = 0 \tag{2.18}$$

where $\hat{n}$ is the unit vector normal to the interface, pointing from medium 2 into medium 1. A very important special case is that medium 2 is a perfect electric conductor (PEC). Since the fields inside the PEC are zero, (2.15)-(2.16) reduce to

$$\hat{n} \times \mathbf{E}_1 = 0 \tag{2.19}$$

$$\hat{n} \times \mathbf{H}_1 = 0 \tag{2.20}$$

That is, along the PEC interface, the tangential components of the electric and magnetic fields are zero.

The two curl equations of (2.1)-(2.2) form the basis of the FDTD algorithm for solving 3D electromagnetic problems. Usually, the two Gauss's Laws of (2.3)-(2.4) will not be explicitly implemented in FDTD. However, to avoid the risk of introducing artificial charges into the domain, it is very important to check whether or not the two Gauss's laws are implicitly satisfied by any FDTD algorithm.

2.2. The Standard FDTD(2,2) (Yee's) Algorithm

As the simplest case of the SFD schemes, the FDTD(2,2) (Yee's) algorithm is second-order accurate in both the time and space domains. In other words, the time and space derivatives in Maxwell's equations are replaced by the second-order central difference approximations. Letting $f(\xi, t)$ represent an arbitrary function of space and time, this can be expressed as

$$\frac{\partial f(\xi,t)}{\partial \xi} = \frac{f(\xi + \Delta\xi/2, t) - f(\xi - \Delta\xi/2, t)}{\Delta\xi} + O\ (\Delta\xi^2), \quad \xi = x, y, z \tag{2.21}$$

$$\frac{\partial f(\xi,t)}{\partial t} = \frac{f(\xi, t + \Delta t/2) - f(\xi, t + \Delta t/2)}{\Delta t} + O\ (\Delta t^2) \tag{2.22}$$

Conventionally, the finite difference approximations (2.21)-(2.22) are also referred to as the space and time *stencils*, respectively. For example, the space stencil along the x-axis is illustrated in Fig. 2.1. As shown, in order to evaluate the partial derivative $\partial f/\partial x$ at the center point x, one needs to calculate the difference between the two neighboring values at $x - \Delta x/2$ and $x + \Delta x/2$; then divide it by the distance between them (Δx). The constants

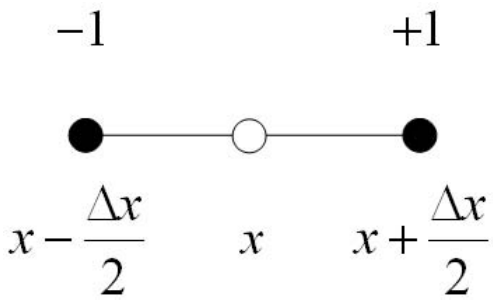

Fig. 2.1. Second-order central difference stencil along the x direction.

above each point are the weighting coefficients which can be derived from Taylor series expansion.

Before the introduction of Yee's algorithm, the notations that follows will be introduced and used repeatedly. In Cartesian coordinates, the space steps with respect to x, y, and z directions and the time increment are denoted as Δx, Δy, Δz, and Δt, respectively. The space position at $(i\Delta x, j\Delta y, k\Delta z)$ is represented by the space indices (i, j, k). The time instant $n\Delta t$ is represented by the time index n. Following these notations, an arbitrary grid function at time $t = n\Delta t$ can be expressed as $f|^n_{i,j,k}$.

To demonstrate Yee's algorithm, let us assume that a plane wave is traveling in the z direction in an unbounded, homogeneous medium $(\epsilon, \mu, \sigma, \sigma^*)$. Without loss of generality, we also assume that the plane wave has an E_x component and a magnetic field component H_y, as illustrated in Fig. 2.2.

In Cartesian coordinates, the plane wave can be modeled using the one-dimensional Maxwell's equations which can be written as

$$\frac{\partial E_x}{\partial t} = -\frac{1}{\epsilon}\left(\frac{\partial H_y}{\partial z} + \sigma E_x\right) \tag{2.23}$$

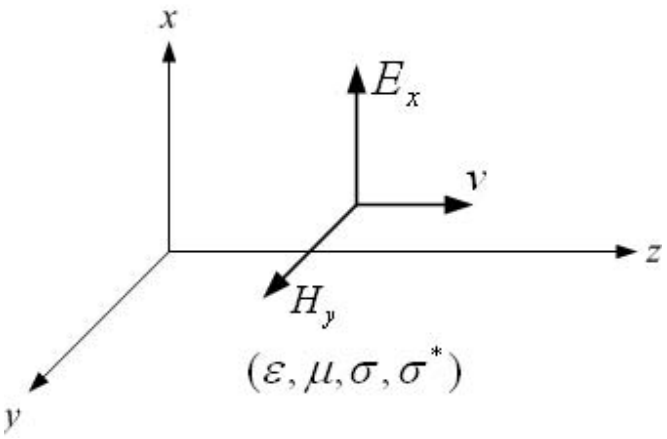

Fig. 2.2. One-dimensional plane wave.

$$\frac{\partial H_y}{\partial t} = -\frac{1}{\mu}\left(\frac{\partial E_x}{\partial z} + \sigma^* H_y\right) \tag{2.24}$$

The space and time derivatives in (2.23) and (2.24) can be approximated by the central differences introduced in (2.21),(2.22). Staggering the E and H fields by half-cell in the space domain and using the leapfrog scheme in the time domain, the one-dimensional Yee's algorithm can be expressed as [6], [1].

$$E_x|_k^{n+1/2} = C_a(k)\, E_x|_k^{n-1/2} - C_b(k)(\, H_y|_{k+1/2}^{n} - H_y|_{k-1/2}^{n}) \tag{2.25}$$

$$H_y|_{k+1/2}^{n+1} = D_a(k+1/2)\, H_y|_{k+1/2}^{n} - D_b(k+1/2)(\, E_x|_{k+1}^{n+1/2} - E_x|_k^{n+1/2}) \tag{2.26}$$

where

$$C_a(k) = \frac{1-(\sigma_k \Delta t)/(2\epsilon_k)}{1+(\sigma_k \Delta t)/(2\epsilon_k)} \tag{2.27}$$

$$C_b(k) = \frac{\Delta t/(\epsilon_k \Delta z)}{1+(\sigma_k \Delta t)/(2\epsilon_k)} \tag{2.28}$$

$$D_a(k) = \frac{1-(\sigma_k^* \Delta t)/(2\mu_k)}{1+(\sigma_k^* \Delta t)/(2\mu_k)} \tag{2.29}$$

$$D_b(k) = \frac{\Delta t/(\mu_k \Delta z)}{1+(\sigma_k^* \Delta t)/(2\mu_k)} \tag{2.30}$$

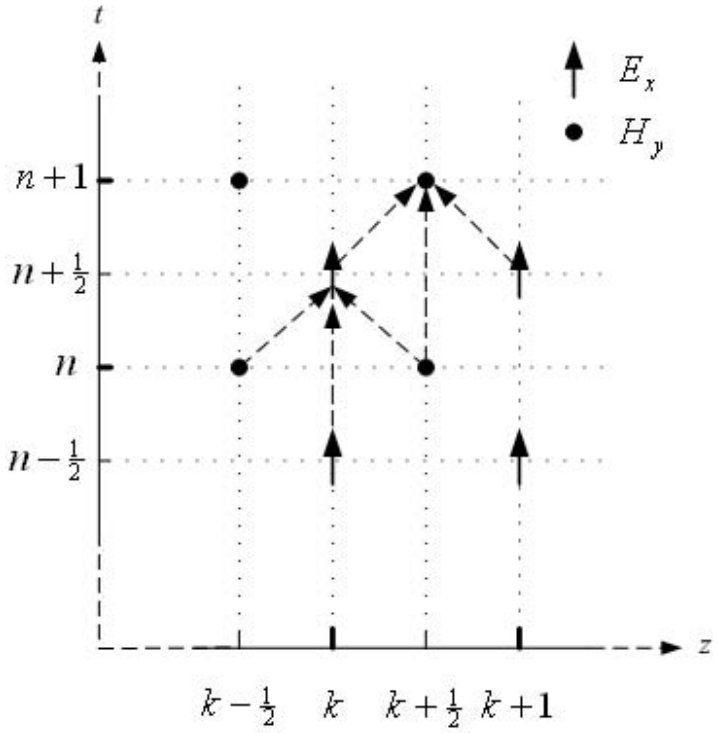

Fig. 2.3. Time-space chart for the one-dimensional Yee algorithm.

are the update coefficients. Notice that ϵ and σ take the values at the positions where the E fields are located and μ and σ^* take the values where the H fields are located.

Yee's algorithm can be also explained using a time-space chart illustrated in Fig. 2.3 [13]. As shown, to update the E_x field at $(k, n+1/2)$, one needs the E_x field at $(k, n-1/2)$ and the H_y fields at $(k-1/2, n)$ and $(k+1/2, n)$. After that, the updated E_x field at $(k, n+1/2)$, together with the E_x field at $(k+1, n+1/2)$ and the H_y field at $(k+1/2, n)$, will be used to update the H_y field at $(k+1/2, n+1)$. This progress continues until the time advance is terminated.

In two dimensions, electromagnetic boundary-value problems can be classified by two modes; i.e., TE^z and TM^z modes. In Cartesian coordinates, Maxwell's equations for TE^z

modes in general lossy media can be written as [2]

$$\frac{\partial E_x}{\partial t} = \frac{1}{\epsilon}\left(\frac{\partial H_z}{\partial y} - \sigma E_x\right) \tag{2.31}$$

$$\frac{\partial E_y}{\partial t} = -\frac{1}{\epsilon}\left(\frac{\partial H_z}{\partial x} + \sigma E_y\right) \tag{2.32}$$

$$\frac{\partial H_z}{\partial t} = \frac{1}{\mu}\left(\frac{\partial E_x}{\partial y} - \frac{\partial E_y}{\partial x} - \sigma^* H_z\right) \tag{2.33}$$

For the dual TM^z modes, Maxwell's equations can be expressed as [2]

$$\frac{\partial H_x}{\partial t} = -\frac{1}{\mu}\left(\frac{\partial E_z}{\partial y} + \sigma^* H_x\right) \tag{2.34}$$

$$\frac{\partial H_y}{\partial t} = \frac{1}{\mu}\left(\frac{\partial E_z}{\partial x} - \sigma^* H_y\right) \tag{2.35}$$

$$\frac{\partial E_z}{\partial t} = \frac{1}{\epsilon}\left(\frac{\partial H_y}{\partial x} - \frac{\partial H_x}{\partial y} - \sigma E_z\right) \tag{2.36}$$

Staggering the electric and magnetic fields in both the x and y directions, the two-dimensional Yee's grids for TE^z and TM^z modes are demonstrated in Figs. 2.4 and 2.5, respectively.

In the time domain, the leap-frog scheme is used to discretize the time derivatives. Following a similar procedure as for one-dimensional problems, the two-dimensional Yee's algorithms for and TE^z and TM^z modes take the form of [6], [1]

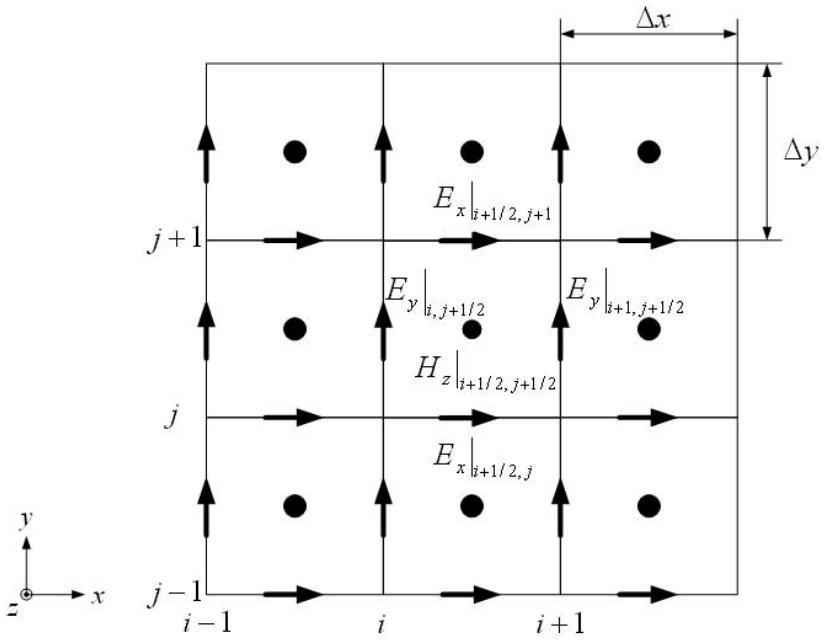

Fig. 2.4. Two-dimensional Yee's grids (TE^z).

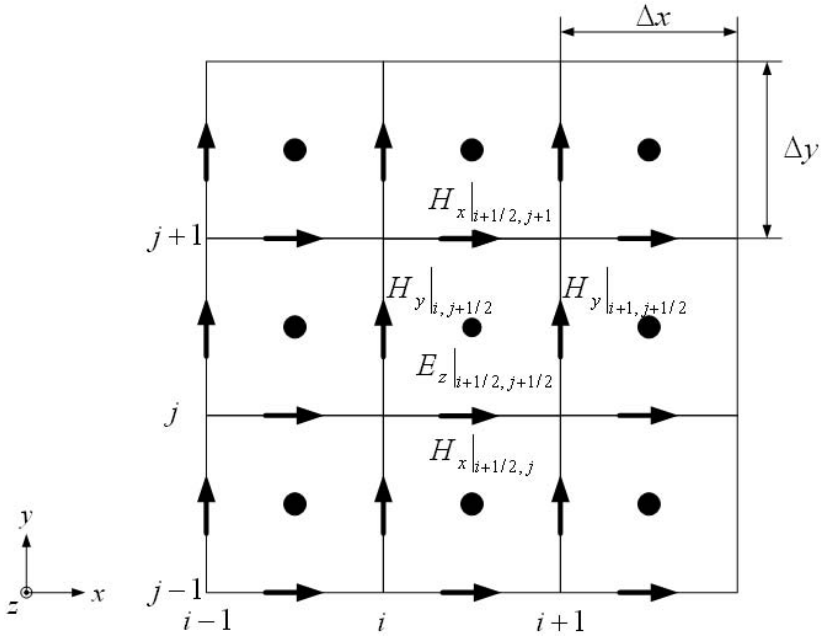

Fig. 2.5. Two-dimensional Yee's grids (TM^z).

$\underline{TE^z \text{ mode:}}$

$$
\begin{aligned}
E_x|^{n+1/2}_{i+1/2,j} &= C_a(i+1/2,j)\; E_x|^{n-1/2}_{i+1/2,j} \\
&+ C_{by}(i+1/2,j)(\,H_z|^{n}_{i+1/2,j+1/2} - H_z|^{n}_{i+1/2,j-1/2}) \qquad (2.37)\\
E_y|^{n+1/2}_{i,j+1/2} &= C_a(i,j+1/2)\; E_y|^{n-1/2}_{i,j+1/2} \\
&- C_{bx}(i,j+1/2)(\,H_z|^{n}_{i+1/2,j+1/2} - H_z|^{n}_{i-1/2,j+1/2}) \qquad (2.38)\\
H_z|^{n+1}_{i+1/2,j+1/2} &= D_a(i+1/2,j+1/2)\; H_z|^{n}_{i+1/2,j+1/2} \\
&+ D_{by}(i+1/2,j+1/2)(\,E_x|^{n+1/2}_{i+1/2,j+1} - E_x|^{n+1/2}_{i+1/2,j}) \\
&- D_{bx}(i+1/2,j+1/2)(\,E_y|^{n+1/2}_{i+1,j+1/2} - E_y|^{n+1/2}_{i,j+1/2}) \qquad (2.39)
\end{aligned}
$$

$\underline{TM^z \text{ mode:}}$

$$
\begin{aligned}
H_x|^{n+1}_{i+1/2,j} &= D_a(i+1/2,j)\; H_x|^{n}_{i+1/2,j} \\
&- D_{by}(i+1/2,j)(\,E_z|^{n+1/2}_{i+1/2,j+1/2} - E_z|^{n+1/2}_{i+1/2,j-1/2}) \qquad (2.40)\\
H_y|^{n+1}_{i,j+1/2} &= D_a(i,j+1/2)\; H_y|^{n}_{i,j+1/2} \\
&- D_{bx}(i,j+1/2)(\,E_z|^{n+1/2}_{i+1/2,j+1/2} - E_z|^{n+1/2}_{i-1/2,j+1/2}) \qquad (2.41)\\
E_z|^{n+1/2}_{i+1/2,j+1/2} &= C_a(i+1/2,j+1/2)\; E_z|^{n-1/2}_{i+1/2,j+1/2} \\
&- C_{by}(i+1/2,j+1/2)(\,H_x|^{n}_{i+1/2,j+1} - H_x|^{n}_{i+1/2,j}) \\
&- C_{bx}(i+1/2,j+1/2)(\,H_y|^{n}_{i+1,j+1/2} - H_y|^{n}_{i,j+1/2}) \qquad (2.42)
\end{aligned}
$$

where

$$C_a(i,j) = \frac{1-(\sigma_{i,j}\Delta t)/(2\epsilon_{i,j})}{1+(\sigma_{i,j}\Delta t)/(2\epsilon_{i,j})} \tag{2.43}$$

$$C_{b\xi}(i,j) = \frac{\Delta t/(\epsilon_{i,j}\Delta\xi)}{1+(\sigma_{i,j}\Delta t)/(2\epsilon_{i,j}}, \ \xi = x, y \tag{2.44}$$

$$D_a(i,j) = \frac{1-(\sigma^*_{i,j}\Delta t)/(2\mu_{i,j})}{1+(\sigma^*_{i,j}\Delta t)/(2\mu_{i,j})} \tag{2.45}$$

$$D_{b\xi}(i,j) = \frac{\Delta t/(\mu_{i,j}\Delta\xi)}{1+(\sigma^*_{i,j}\Delta t)/(2\mu_{i,j})}, \ \xi = x, y \tag{2.46}$$

In the three-dimensional Cartesian coordinates, Maxwell's equations of (2.1) and (2.2) reduce to a system of six coupled scalar equations which can be expressed as [2]

$$\frac{\partial H_x}{\partial t} = \frac{1}{\mu}\left(\frac{\partial E_y}{\partial z} - \frac{\partial E_z}{\partial y} - \sigma^* H_x\right) \tag{2.47}$$

$$\frac{\partial H_y}{\partial t} = \frac{1}{\mu}\left(\frac{\partial E_z}{\partial x} - \frac{\partial E_x}{\partial z} - \sigma^* H_y\right) \tag{2.48}$$

$$\frac{\partial H_z}{\partial t} = \frac{1}{\mu}\left(\frac{\partial E_x}{\partial y} - \frac{\partial E_y}{\partial x} - \sigma^* H_z\right) \tag{2.49}$$

$$\frac{\partial E_x}{\partial t} = \frac{1}{\epsilon}\left(\frac{\partial H_z}{\partial y} - \frac{\partial H_y}{\partial z} - \sigma E_x\right) \tag{2.50}$$

$$\frac{\partial E_y}{\partial t} = \frac{1}{\epsilon}\left(\frac{\partial H_x}{\partial z} - \frac{\partial H_z}{\partial x} - \sigma E_y\right) \tag{2.51}$$

$$\frac{\partial E_z}{\partial t} = \frac{1}{\epsilon}\left(\frac{\partial H_y}{\partial x} - \frac{\partial H_x}{\partial y} - \sigma E_z\right) \tag{2.52}$$

To solve three-dimensional problems, the space domain is discretized using the Yee's unit cell, as illustrated in Fig. 2.6. As shown, all the field components are located at different positions on the surface of the Yee cell. The E and H fields are staggered at a distance of half space-step which allows the explicit evaluation of the curls at each surface plane. Different constitutive parameters are locally assigned to each field component to model different materials. Using the leap-frog scheme in the time-domain, the three-dimensional

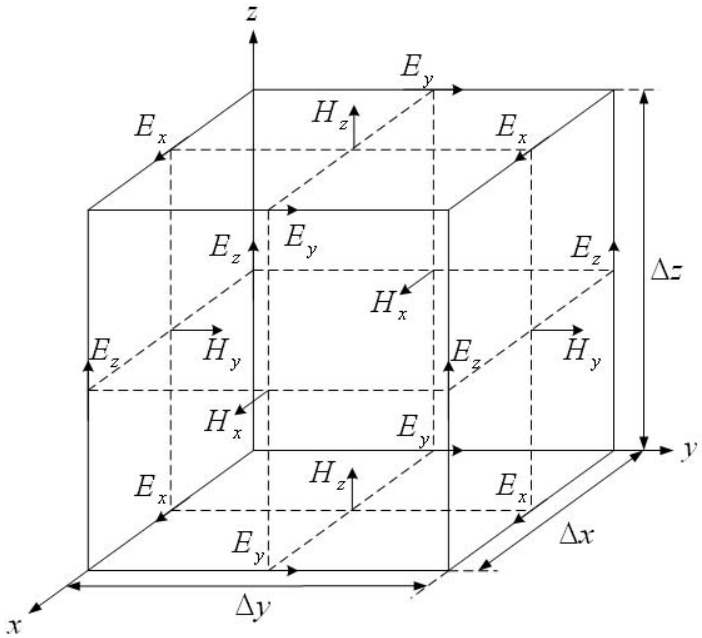

Fig. 2.6. The three-dimensional Yee's unit cell [1].

Yee update equations are given by [6], [1]

$$
\begin{aligned}
E_x|^{n+1/2}_{i+1/2,j,k} &= C_a(i+1/2,j,k)\; E_x|^{n-1/2}_{i+1/2,j,k} \\
&+ C_{by}(i+1/2,j,k)(\,H_z|^{n}_{i+1/2,j+1/2,k} - H_z|^{n}_{i+1/2,j-1/2,k}) \\
&- C_{bz}(i+1/2,j,k)(\,H_y|^{n}_{i+1/2,j,k+1/2} - H_y|^{n}_{i+1/2,j,k-1/2}) \qquad (2.53) \\
E_y|^{n+1/2}_{i,j+1/2,k} &= C_a(i,j+1/2,k)\; E_y|^{n-1/2}_{i,j+1/2,k} \\
&+ C_{bz}(i,j+1/2,k)(\,H_x|^{n}_{i,j+1/2,k+1/2} - H_x|^{n}_{i,j+1/2,k-1/2}) \\
&- C_{bx}(i,j+1/2,k)(\,H_z|^{n}_{i+1/2,j+1/2,k} - H_z|^{n}_{i-1/2,j+1/2,k}) \qquad (2.54) \\
E_z|^{n+1/2}_{i,j,k+1/2} &= C_a(i,j,k+1/2)\; E_z|^{n-1/2}_{i,j,k+1/2} \\
&+ C_{bx}(i,j,k+1/2)(\,H_y|^{n}_{i+1/2,j,k+1/2} - H_y|^{n}_{i-1/2,j,k+1/2}) \\
&- C_{by}(i,j,k+1/2)(\,H_x|^{n}_{i,j+1/2,k+1/2} - H_x|^{n}_{i,j-1/2,k+1/2}) \qquad (2.55)
\end{aligned}
$$

$$
\begin{aligned}
H_x|^{n+1}_{i,j+1/2,k+1/2} &= D_a(i,j+1/2,k+1/2)\; H_x|^{n}_{i,j+1/2,k+1/2} \\
&+ D_{bz}(i,j+1/2,k+1/2)(\,E_y|^{n+1/2}_{i,j+1/2,k+1} - E_y|^{n+1/2}_{i,j+1/2,k}) \\
&- D_{by}(i,j+1/2,k+1/2)(\,E_z|^{n+1/2}_{i,j+1,k+1/2} - E_z|^{n+1/2}_{i,j,k+1/2}) \qquad (2.56) \\
H_y|^{n+1}_{i+1/2,j,k+1/2} &= D_a(i+1/2,j,k+1/2)\; H_y|^{n}_{i+1/2,j,k+1/2} \\
&+ D_{bx}(i+1/2,j,k+1/2)(\,E_z|^{n+1/2}_{i+1,j,k+1/2} - E_z|^{n+1/2}_{i,j,k+1/2}) \\
&- D_{bz}(i+1/2,j,k+1/2)(\,E_x|^{n+1/2}_{i+1/2,j,k+1} - E_x|^{n+1/2}_{i+1/2,j,k}) \qquad (2.57) \\
H_z|^{n+1}_{i+1/2,j+1/2,k} &= D_a(i+1/2,j+1/2,k)\; H_z|^{n}_{i+1/2,j+1/2,k} \\
&+ D_{by}(i+1/2,j+1/2,k)(\,E_x|^{n+1/2}_{i+1/2,j+1,k} - E_x|^{n+1/2}_{i+1/2,j,k}) \\
&- D_{bx}(i+1/2,j+1/2,k)(\,E_y|^{n+1/2}_{i+1,j+1/2,k} - E_y|^{n+1/2}_{i,j+1/2,k}) \qquad (2.58)
\end{aligned}
$$

where

$$
\begin{aligned}
C_a(i,j,k) &= \frac{1-(\sigma_{i,j,k}\Delta t)/(2\epsilon_{i,j,k})}{1+(\sigma_{i,j,k}\Delta t)/(2\epsilon_{i,j,k})} && (2.59) \\
C_{b\xi}(i,j,k) &= \frac{\Delta t/(\epsilon_{i,j,k}\Delta\xi)}{1+(\sigma_{i,j,k}\Delta t)/(2\epsilon_{i,j,k}}, \;\xi = x,y,z && (2.60) \\
D_a(i,j,k) &= \frac{1-(\sigma^*_{i,j,k}\Delta t)/(2\mu_{i,j,k})}{1+(\sigma^*_{i,j,k}\Delta t)/(2\mu_{i,j,k})} && (2.61) \\
D_{b\xi}(i,j,k) &= \frac{\Delta t/(\mu_{i,j,k}\Delta\xi)}{1+(\sigma^*_{i,j,k}\Delta t)/(2\mu_{i,j,k})}, \;\xi = x,y,z && (2.62)
\end{aligned}
$$

Despite its second-order accuracy, Yee's algorithm is the most popular FDTD method for computational electromagnetics. For years, it has been successfully applied to solve numerous practical electromagnetic problems. There is a large collection of models simulated by Yee's grid, from a small IC package to a large fuselage. When a dispersion-reduction method is designed, it is usually desired that the new algorithm is able to take advantage of the available geometry library. In other words, the new dispersion-reduction scheme must also use Yee's grid. One of the most promising approaches is to use the standard

higher-order schemes.

2.3. The Standard Higher-Order Schemes

The standard higher-order schemes denote those methods which use the finite-difference approximations with accuracy higher than second-order. Higher-order stencils can be used to discretize the derivatives in both the time- and the space-domain. For clarity, we only consider the space-domain higher-order stencils. In the time domain, the second-order stencil is still used. Hence, the standard higher-order methods in this report can be referred to as the FDTD(2,N) schemes. Notice that, for the central difference stencils, N is always an even integer. To be compatible to the the available geometry file, Yee's grids are used for the space discretization.

Before the discussion of the characteristics of the higher-order stencils, the method to derive these stencils will be introduced. For example, to approximate the derivative at the center point, the central difference approximation involving four neighboring points can be expressed as

$$\begin{aligned} f'(\xi) &\approx \frac{C_1 f\left(\xi - \frac{3\Delta\xi}{2}\right) + C_2 f\left(\xi - \frac{\Delta\xi}{2}\right) + C_3 f\left(\xi + \frac{\Delta\xi}{2}\right) + C_4 f\left(\xi + \frac{3\Delta\xi}{2}\right)}{\Delta\xi} \\ \xi &= x, y, z \end{aligned} \tag{2.63}$$

where the four coefficients C_1, C_2, C_3, and C_4 are undetermined. Expanding the function

values at the four neighboring points yields

$$
\begin{aligned}
f\left(\xi-\frac{3\Delta\xi}{2}\right) &= f(\xi)-\frac{3\Delta\xi}{2}f'(\xi)+\frac{9\Delta\xi^2}{8}f''(\xi)-\frac{9\Delta\xi^3}{16}f'''(\xi)+\frac{27\Delta\xi^4}{128}f^{(4)}(\xi) \\
&- \frac{81\Delta\xi^5}{1280}f^{(5)}(\xi)+\cdots \qquad (2.64)\\
f\left(\xi-\frac{\Delta\xi}{2}\right) &= f(\xi)-\frac{\Delta\xi}{2}f'(\xi)+\frac{\Delta\xi^2}{8}f''(\xi)-\frac{\Delta\xi^3}{48}f'''(\xi)+\frac{\Delta\xi^4}{384}f^{(4)}(\xi) \\
&- \frac{\Delta\xi^5}{3840}f^{(5)}(\xi)+\cdots \qquad (2.65)\\
f\left(\xi+\frac{\Delta\xi}{2}\right) &= f(\xi)+\frac{\Delta\xi}{2}f'(\xi)+\frac{\Delta\xi^2}{8}f''(\xi)+\frac{\Delta\xi^3}{48}f'''(\xi)+\frac{\Delta\xi^4}{384}f^{(4)}(\xi) \\
&+ \frac{\Delta\xi^5}{3840}f^{(5)}(\xi)+\cdots \qquad (2.66)\\
f\left(\xi+\frac{3\Delta\xi}{2}\right) &= f(\xi)+\frac{3\Delta\xi}{2}f'(\xi)+\frac{9\Delta\xi^2}{8}f''(\xi)+\frac{9\Delta\xi^3}{16}f'''(\xi)+\frac{27\Delta\xi^4}{128}f^{(4)}(\xi) \\
&+ \frac{81\Delta\xi^5}{1280}f^{(5)}(\xi)+\cdots \qquad (2.67)
\end{aligned}
$$

Substituting (2.64)-(2.67) into (2.63) and collecting terms leads to

$$
\begin{aligned}
f'(\xi) &\approx (C_1+C_2+C_3+C_4)\frac{1}{\Delta\xi}f(\xi) \\
&+ (-3C_1-C_2+C_3+3C_4)\frac{1}{2}f'(\xi) \\
&+ (9C_1+C_2+C_3+9C_4)\frac{\Delta\xi}{8}f''(\xi) \\
&+ (-27C_1-C_2+C_3+27C_4)\frac{\Delta\xi^2}{48}f'''(\xi) \\
&+ (81C_1+C_2+C_3+81C_4)\frac{\Delta\xi^3}{384}f^{(4)}(\xi) \\
&+ (-243C_1-C_2+C_3+243C_4)\frac{\Delta\xi^4}{3840}f^{(5)}(\xi) \\
&+ \cdots \qquad (2.68)
\end{aligned}
$$

In order to approximate the derivative, the coefficient of the second term in (2.68) must be unity. Furthermore, to achieve the accuracy as high as possible, the coefficients for the

first, third and fourth terms must be zero. This leads to the following matrix equation

$$\begin{bmatrix} 1 & 1 & 1 & 1 \\ -3 & -1 & 1 & 3 \\ 9 & 1 & 1 & 9 \\ -27 & -1 & 1 & 27 \end{bmatrix} \cdot \begin{bmatrix} C_1 \\ C_2 \\ C_3 \\ C_4 \end{bmatrix} = \begin{bmatrix} 0 \\ 2 \\ 0 \\ 0 \end{bmatrix} \tag{2.69}$$

Solving (2.69), the unknown coefficients C_1, C_2, C_3, and C_4 are determined to be $1/24, -9/8, 9/8$, and $-1/24$, respectively. The resultant stencil of fourth-order accuracy can thus be written as

$$\begin{aligned} f'(\xi) &= \frac{9}{8}\frac{[f(\xi+\Delta\xi/2)-f(\xi-\Delta\xi/2)]}{\Delta\xi} \\ &- \frac{1}{24}\frac{[f(\xi+3\Delta\xi/2)-f(\xi-3\Delta\xi/2)]}{\Delta\xi} - \frac{3\Delta\xi^4}{640}f^{(5)}(\xi)+\cdots \\ &= \frac{9}{8}\frac{[f(\xi+\Delta\xi/2)-f(\xi-\Delta\xi/2)]}{\Delta\xi} \\ &- \frac{1}{24}\frac{[f(\xi+3\Delta\xi/2)-f(\xi-3\Delta\xi/2)]}{\Delta\xi} + O\left(\Delta\xi^4\right), \\ \xi &= x, y, z \end{aligned} \tag{2.70}$$

where the $(-3\Delta\xi^4)f^{(5)}(\xi)$ is the leading truncation error which mainly determines the order of accuracy of the stencil. For example, the fourth-order stencil in the x direction is illustrated in Fig. 2.7. Apparently, in order to evaluate the derivative at the center point, one needs to use the function values of the four neighboring values. The number above each point is the weighting coefficient for the summation. The method summarized in (2.63)-(2.70) is referred to as the *method of the undetermined coefficients* [87]. In general, this method can be used to evaluate the derivative not only at the central point, but also at an arbitrary position in the grid.

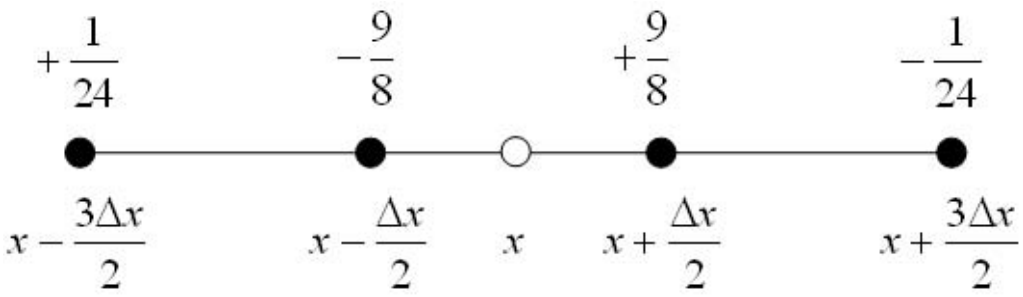

Fig. 2.7. Fourth-order central difference stencil along the x direction.

From observation, for central difference, the only difference of the coefficients at the symmetrical points is a minus sign. Therefore, a central difference stencil of N-th order (N is an even integer) can be expressed as [15], [86]

$$f'(\xi) \approx \frac{1}{\Delta\xi} \sum_{n=1}^{N/2} C_n \{ f[\xi + (2n-1)\Delta\xi] - f[\xi - (2n-1)\Delta\xi] \} \tag{2.71}$$

Applying the method of the undetermined coefficients leads to the following $N/2 \times N/2$ linear system

$$\begin{bmatrix} 1 & 3 & \cdots & N-1 \\ 1 & 3^3 & \cdots & (N-1)^3 \\ \vdots & \vdots & \ddots & \vdots \\ 1 & 3^{N-1} & \cdots & (N-1)^{N-1} \end{bmatrix} \cdot \begin{bmatrix} C_1 \\ C_2 \\ \vdots \\ C_{N/2} \end{bmatrix} = \begin{bmatrix} 1 \\ 0 \\ \vdots \\ 0 \end{bmatrix} \tag{2.72}$$

The solution of (2.72) can be written in close form as [86]

$$C_n = \frac{(-1)^{n-1}(N-1)!!^2}{2^{N-2}(N/2+n-1)!(N/2-n)!(2n-1)^2} \tag{2.73}$$

where $x!!$ represents $x(x-2)(x-4)\ldots$. The leading truncation error can be written as

$$Err^T = \frac{\Delta\xi^N f^{(N+1)}(\xi)}{2^N (N+1)!} \sum_{n=1}^{N/2} C_n (2n-1)^{N+1} \tag{2.74}$$

The coefficients and the truncation errors for the central difference stencils up to eighth-order accurate are summarized in Table 2.1 [67], [86].

Table 2.1. Coefficients and Truncation Errors of the Central Difference Stencils

N	C_1	C_2	C_3	C_4	Err^T
2	1	0	0	0	$\frac{\Delta\xi^2}{24}f^{(3)}(\xi)$
4	$\frac{9}{8}$	$-\frac{1}{24}$	0	0	$-\frac{3\Delta\xi^4}{640}f^{(5)}(\xi)$
6	$\frac{75}{64}$	$-\frac{25}{384}$	$\frac{3}{640}$	0	$\frac{5\Delta\xi^6}{7168}f^{(7)}(\xi)$
8	$\frac{1225}{1024}$	$-\frac{245}{3072}$	$\frac{49}{5120}$	$-\frac{5}{7168}$	$-\frac{35\Delta\xi^8}{294912}f^{(9)}(\xi)$

Notice that the truncation errors all have the similar structure which can be expressed as [87]

$$Err^T(\Delta\xi) \approx C\Delta\xi^N \tag{2.75}$$

where C is a constant determined by the $(N+1)$-th derivative. Taking the logarithm of both sides of (2.75) yields

$$\log\left[Err^T(\Delta\xi)\right] \approx \log C + N\log\Delta\xi \tag{2.76}$$

That is, $\log[Err^T(\Delta\xi)]$ is a linear function of $\log\Delta\xi$ with slope N. For example, let us approximate the derivative of $f(\xi) = \cos(\xi)$ at $\xi = 1$. The log-log plots of the truncation errors in Table 2.1 versus $1/(\Delta\xi)$ are shown in Fig. 2.8. It is evident that the slopes of the lines agree with the corresponding order of accuracy. For this case, increasing the order of accuracy greatly reduces the errors.

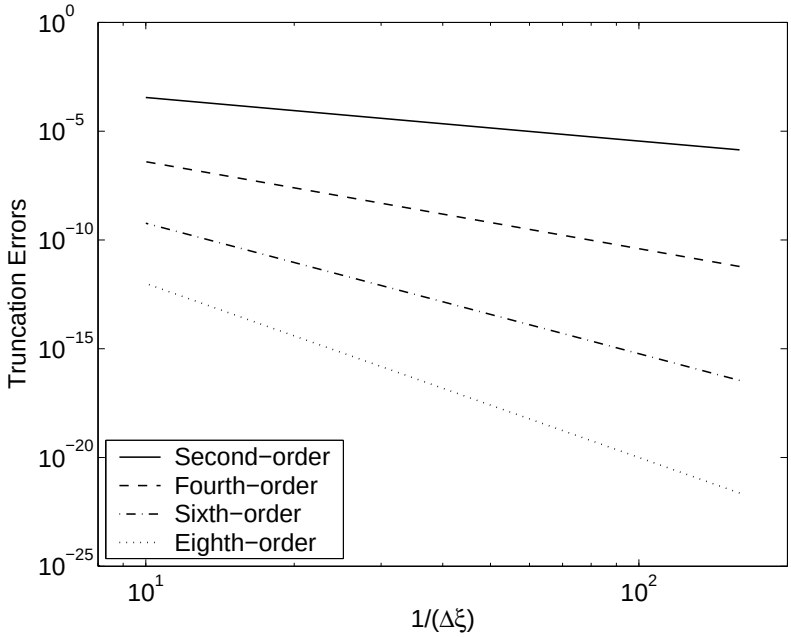

Fig. 2.8. Truncation error of the central difference stencils.

To apply the higher-order scheme, one only need to replace the second-order space-domain stencils in Yee's update equations (2.53) - (2.58) by the higher-order stencils (2.71). The leap-frog scheme and Yee's grids remain the same.

2.4. Stability Condition

In order to guarantee the convergence of the numerical solution, the time step Δt must be bounded. This bound is usually referred to as the *Courant Stability Condition* [1]. Using the complex analysis of the dispersion relation [1] or the classical Von Neumann method [88], [14], the stability conditions for the one-, two-, and three-dimensional Yee algorithms can be expressed as

One-dimension:

$$\Delta t \leq \frac{\Delta x}{c} \tag{2.77}$$

Two-dimensions:

$$\Delta t \leq \frac{1}{c\sqrt{\frac{1}{\Delta x^2}+\frac{1}{\Delta y^2}}} \tag{2.78}$$

Three-dimensions:

$$\Delta t \leq \frac{1}{c\sqrt{\frac{1}{\Delta x^2}+\frac{1}{\Delta y^2}+\frac{1}{\Delta z^2}}} \tag{2.79}$$

where Δt is the time step, c is the speed of light, and $\Delta x, \Delta y, \Delta z$ are space steps with respect to x, y, z axes, respectively. For the cubic mesh where ($\Delta x = \Delta y = \Delta z = \Delta s$), the stability conditions of (2.77)-(2.79) reduce to

One-dimension:

$$S = \frac{c\Delta t}{\Delta s} \leq 1 \tag{2.80}$$

Two-dimensions:

$$S = \frac{c\Delta t}{\Delta s} \leq \frac{1}{\sqrt{2}} \tag{2.81}$$

Three-dimensions:

$$S = \frac{c\Delta t}{\Delta s} \leq \frac{1}{\sqrt{3}} \tag{2.82}$$

where the constant S is the *Courant number* which describes the relation between c, Δt, and Δs.

The stability conditions for the higher-order schemes have to be derived individually. Here, the stability condition for the important FDTD(2,4) scheme is summarized [1]

One-dimension:

$$\Delta t \leq \frac{6}{7}\frac{\Delta x}{c} \tag{2.83}$$

Two-dimensions:

$$\Delta t \leq \frac{6}{7} \frac{1}{c\sqrt{\frac{1}{\Delta x^2} + \frac{1}{\Delta y^2}}} \tag{2.84}$$

Three-dimensions:

$$\Delta t \leq \frac{6}{7} \frac{1}{c\sqrt{\frac{1}{\Delta x^2} + \frac{1}{\Delta y^2} + \frac{1}{\Delta z^2}}} \tag{2.85}$$

For the cubic mesh, (2.83) - (2.85) reduce to

One-dimension:

$$S = \frac{c\Delta t}{\Delta s} \leq \frac{6}{7} \tag{2.86}$$

Two-dimensions:

$$S = \frac{c\Delta t}{\Delta s} \leq \frac{6}{7} \frac{1}{\sqrt{2}} \tag{2.87}$$

Three-dimensions:

$$S = \frac{c\Delta t}{\Delta s} \leq \frac{6}{7} \frac{1}{\sqrt{3}} \tag{2.88}$$

2.5. Dispersion Analysis

The standard FDTD algorithms are the discrete conterparts of Maxwell's equations. It is inevitable that, when the continuous derivatives and domains are discretized, some numerical errors are generated. Among these errors, the numerical dispersion is the most critical. Dispersion is a nonphysical numerical effect meaning that the numerical phase velocity of the wave is a function of the grid discretization, operating frequency, and propagation angles. As indicated in [1]: "A useful way to view this phenomenon is that the FDTD algorithm effectively embeds the electromagnetic wave interaction structure of interest in a tenuous 'numerical aether' having a permittivity very close to vacuum, but not quite. This 'aether' causes propagating waves to accumulate delay or phase errors that can lead

to non-physical results, such as broadening and ringing of single-pulse waveforms, imprecise cancelation of multiple scattered waves, spurious anisotropy, and pseudo-refraction." Thus the accumulation of the dispersion error can be significant to destroy the final results, especially for problems that contain electrically large structures or need very long simulation time. Fourier analysis has been used to investigate the the numerical dispersion of a variety of FDTD algorithms [1], [66], [67]. In this section, the dispersion characteristics of the standard FDTD schemes will be reviewed.

2.5.1. The FDTD(2,2) Scheme

Let us consider the one-dimensional Yee algorithm in a free-space region. An 1D monochromatic numerical wave can be expressed as

$$E_x = E_0 e^{j(\omega n\Delta t - \tilde{k}K\Delta z)} \tag{2.89}$$

$$H_y = H_0 e^{j(\omega n\Delta t - \tilde{k}K\Delta z)} \tag{2.90}$$

where $\tilde{k}$ is the numerical wave number, K is the space index in the z-direction used to distinguish itself from the wave number. Substituting (2.89)-(2.90) into the finite difference equations (2.25)-(2.26) for the free-space case and combining the resultant equations yields

$$\left(\frac{\Delta z}{c\Delta t}\right)^2 \sin^2\left(\frac{\omega\Delta t}{2}\right) = \sin^2\left(\frac{\tilde{k}\Delta z}{2}\right) \tag{2.91}$$

Such a nonlinear equation that describes the relationship between the numerical wave number $\tilde{k}$ (or numerical phase speed) and the angular frequency ω is referred to as the *dispersion relation*. Apparently, the numerical wave number is no longer a linear function of the angular frequency as is the case in the continuous world.

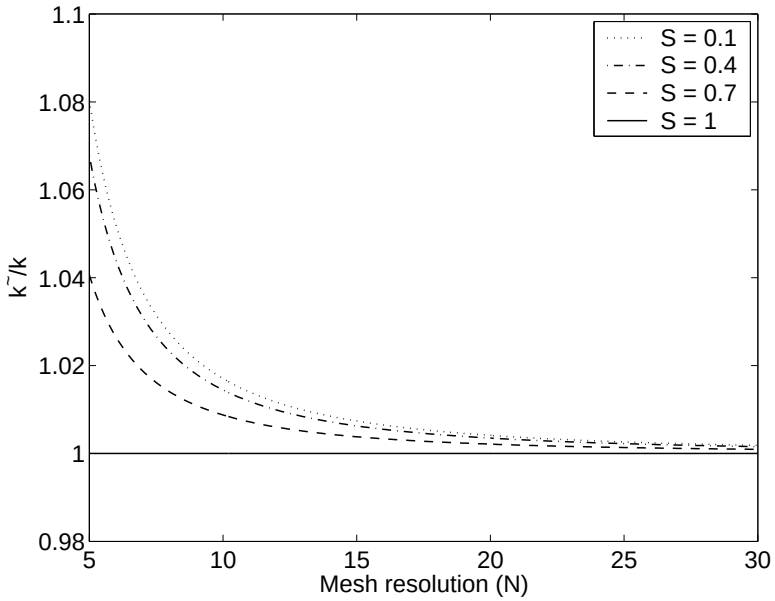

Fig. 2.9. One-dimensional dispersion of the Yee algorithm.

Using S and N to denote the Courant number $c\Delta t/\Delta z$ and the mesh resolution $\lambda/\Delta z$ (where λ is the exact wavelength), (2.91) can be rewritten in a more convenient form [1], [66] as

$$\frac{1}{S^2}\ \sin^2\left(\frac{\pi S}{N}\right) = \sin^2\left(\frac{\pi}{N}\frac{\tilde{k}}{k}\right) \tag{2.92}$$

where $\tilde{k}/k$ is the ratio of the numerical wave number to the exact wave number, which describes the amount of discrepancy between them. Notice that $\tilde{k}/k = 1$ represents the ideal no-dispersion case. For one-dimension, the dispersion relation (2.92) reduces to

$$\frac{\tilde{k}}{k} = \frac{N}{\pi}\sin^{-1}\left[\frac{1}{S}\sin\left(\frac{\pi S}{N}\right)\right] \tag{2.93}$$

For different S values, $\tilde{k}/k$ versus N is plotted in Fig. 2.9. As shown, $\tilde{k}/k$ is always greater than unity. In other words, the numerical wave simulated by Yee's algorithm always

propagates slower than the speed of light in the continuous space. Also notice that, as N increases, $\tilde{k}/k$ approaches unity. That is, the discrepancy between the numerical and exact wave number becomes smaller when a finer mesh resolution is used. When S is unity (Courant stability limit), $\tilde{k}$ is always equal to k for all Ns. This is an ideal situation where there is no dispersion error. The corresponding time-step $\Delta t = \Delta z/c$ is sometimes referred to as the "magic time-step" [1]. Unfortunately, even if the "magic time-step" is used, the dispersion only vanishes along certain directions due to the anisotropy for multi-dimensional cases. The anisotropy of the dispersion can be demonstrated in 2D and 3D dispersion analyses.

Following a similar procedure as for the 1D case, the two-dimensional dispersion relation can be obtained by substituting a monochromatic traveling-wave trial solution into the 2D Yee's algorithms of (2.37)-(2.39) or (2.40)-(2.42) and combining the resultant equations. Both the TE^z and TM^z cases lead to the same dispersion relation of

$$\left(\frac{1}{c\Delta t}\right)^2 \sin^2\left(\frac{\omega\Delta t}{2}\right) = \frac{1}{\Delta x^2}\sin^2\left(\frac{\tilde{k}_x\Delta x}{2}\right) + \frac{1}{\Delta y^2}\sin^2\left(\frac{\tilde{k}_y\Delta y}{2}\right) \tag{2.94}$$

where

$$\tilde{k}_x = \tilde{k}\cos\phi,\ \tilde{k}_y = \tilde{k}\sin\phi$$

Notice that, in two dimensions, the dispersion relation is also a function of the propagation angle ϕ. For the square mesh ($\Delta x = \Delta y = \Delta s$), the two-dimensional dispersion relation can be rewritten as

$$\frac{1}{S^2}\ \sin^2\left(\frac{\pi S}{N}\right) = \sin^2\left(\frac{\pi\cos\phi}{N}\frac{\tilde{k}}{k}\right) + \sin^2\left(\frac{\pi\sin\phi}{N}\frac{\tilde{k}}{k}\right) \tag{2.95}$$

The two-dimensional dispersion relation in (2.95) is a transcendental function which has no close form solution for $\tilde{k}/k$. However, since the derivative of the transcendental function is

readily obtained, (2.95) can be numerically solved using the *Newton-Raphson's* method [89]. The procedure is summarized below.

Letting $x = \tilde{k}/k$, $a = \pi \cos\phi/N$, $b = \pi \sin\phi/N$, and $d = \sin^2(\pi S/N)/S^2$, (2.95) can be rewritten as

$$f(x) = \sin^2(ax) + \sin^2(bx) - d^2 = 0 \tag{2.96}$$

The root x of (2.96) can be solved by performing the following iteration

$$x_{i+1} = x_i - \frac{f(x_i)}{f'(x_i)} \tag{2.97}$$

where $f'(x)$ is the derivative of $f(x)$ which takes the form of

$$f'(x) = a\sin(2ax) + b\sin(2bx) \tag{2.98}$$

Performing the iteration of (2.97), $\tilde{k}/k$ can be readily solved.

Setting $S = 0.5$, $\tilde{k}/k$s versus the propagation angle ϕ for various mesh resolutions N is plotted in Fig. 2.10. Since the dispersion is 90° periodic, only the curves within the first quadrant are plotted. It is evident that all the dispersion curves are anisotropic (functions of propagation angles) which possess their maxima along the principal axes 0° and 90° and the minima along the diagonal axes 45°. Similar to the one-dimensional case, the dispersion decreases as the mesh resolution N increases.

When the mesh resolution is fixed at $N = 10$, $\tilde{k}/k$ versus the propagation angle ϕ for various S are plotted in Fig. 2.11. As S approaches the 2D stability limit $(1/\sqrt{2})$, the dispersion curve shifts down in parallel towards unity. In other words, all the curves maintain the same shape for different S. When $S = 1/\sqrt{2}$, the dispersion eventually vanishes along the diagonal axis $\phi = 45°$.

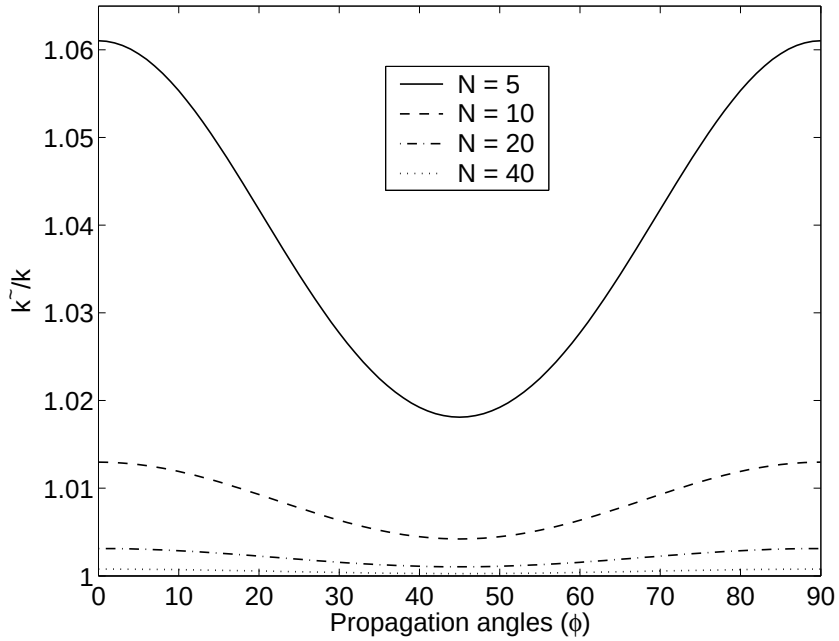

Fig. 2.10. Two-dimensional dispersion of the Yee algorithm ($S = 0.5$).

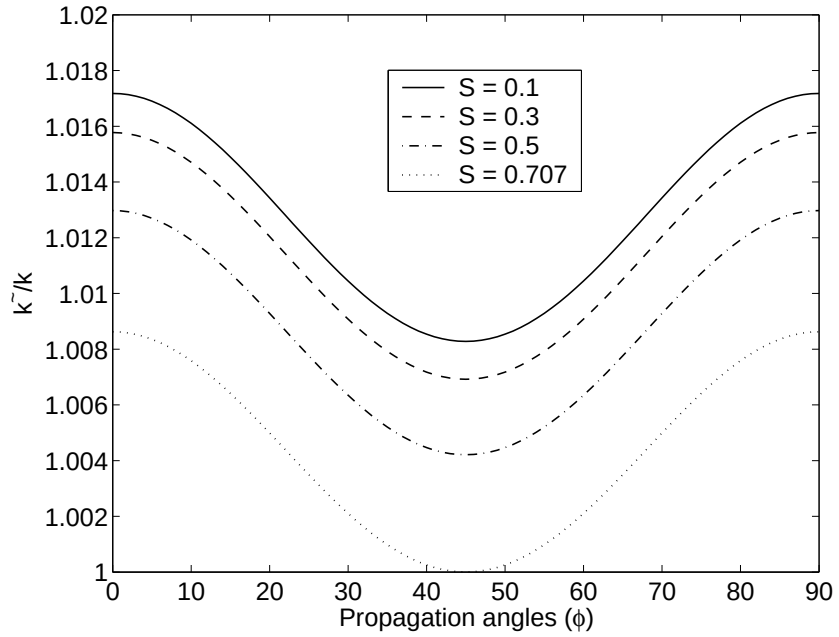

Fig. 2.11. Two-dimensional dispersion of the Yee algorithm ($N = 10$).

The three-dimensional dispersion relation of Yee's algorithm can be readily derived and written as

$$\left(\frac{1}{c\Delta t}\right)^2 \sin^2\left(\frac{\omega\Delta t}{2}\right) = \frac{1}{\Delta x^2}\sin^2\left(\frac{\tilde{k}_x\Delta x}{2}\right) + \frac{1}{\Delta y^2}\sin^2\left(\frac{\tilde{k}_y\Delta y}{2}\right) + \frac{1}{\Delta z^2}\sin^2\left(\frac{\tilde{k}_z\Delta z}{2}\right) \quad (2.99)$$

where

$$\tilde{k}_x = \tilde{k}\cos\phi\sin\theta,\ \tilde{k}_y = \tilde{k}\sin\phi\sin\theta,\ \tilde{k}_z = \tilde{k}\cos\theta,$$

For the cubic mesh ($\Delta x = \Delta y = \Delta z = \Delta s$), (2.99) can be rewritten in the form of

$$\frac{1}{S^2}\sin^2\left(\frac{\pi S}{N}\right) = \sin^2\left(\frac{\pi\cos\phi\sin\theta}{N}\frac{\tilde{k}}{k}\right) + \sin^2\left(\frac{\pi\sin\phi\sin\theta}{N}\frac{\tilde{k}}{k}\right) + \sin^2\left(\frac{\pi\cos\theta}{N}\frac{\tilde{k}}{k}\right) \quad (2.100)$$

For a fixed Courant number $S = 0.4$, $\tilde{k}/k$ versus propagation angles (θ, ϕ) for $N = 5$ and $N = 10$ is plotted in Figs. 2.12 and 2.13, respectively. As N increases, the absolute value and the anisotropy of the dispersion are significantly reduced.

For a fixed mesh resolution $N = 10$, $\tilde{k}/k$s versus propagation angles (θ, ϕ) for different Courant numbers ($S = 0.1$ and $S = 0.577$) is plotted in Figs. 2.14 and 2.15, respectively. It is evident that the shapes of the dispersion for different S are identical. As S approaches the Courant limit $(1/\sqrt{3})$, the $\tilde{k}/k$ distribution shifts down towards unity.

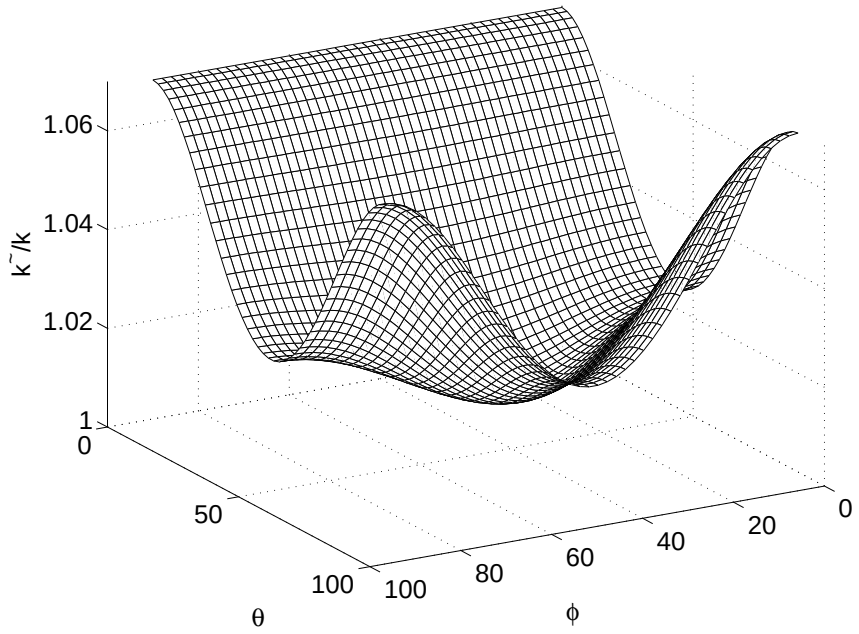

Fig. 2.12. Three-dimensional dispersion of the Yee algorithm ($S = 0.4, N = 5$).

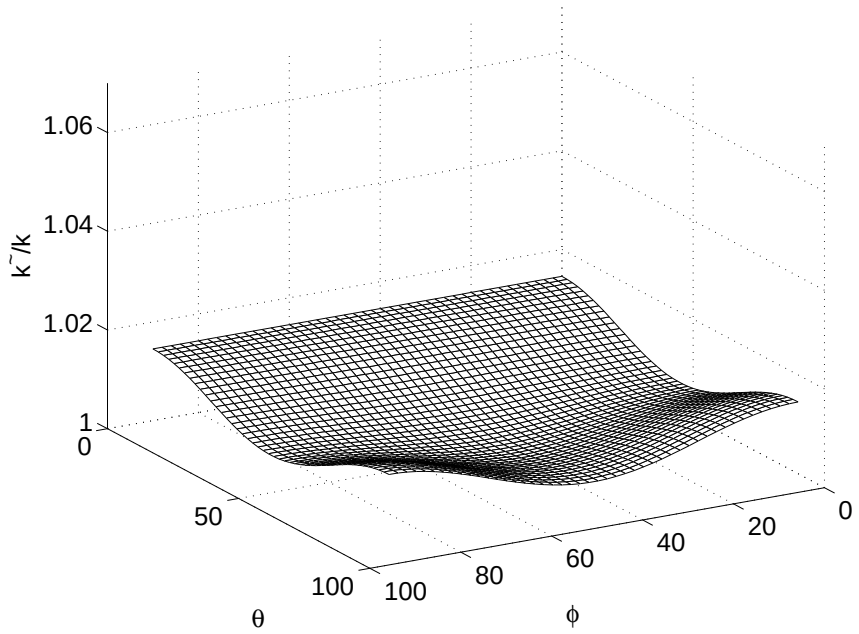

Fig. 2.13. Three-dimensional dispersion of the Yee algorithm ($S = 0.4, N = 10$).

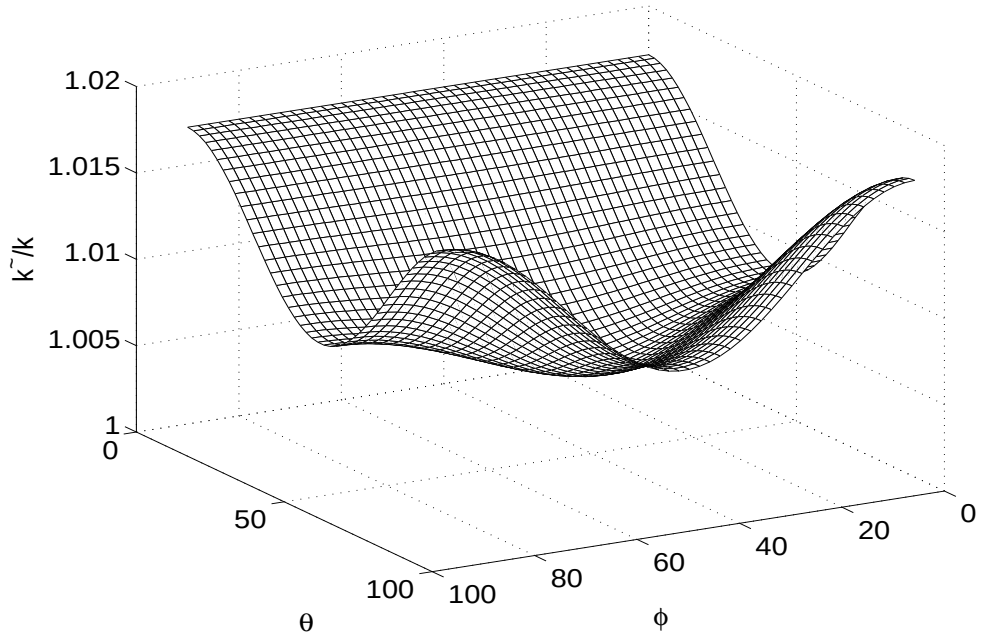

Fig. 2.14. Three-dimensional dispersion of the Yee algorithm ($S = 0.1, N = 10$).

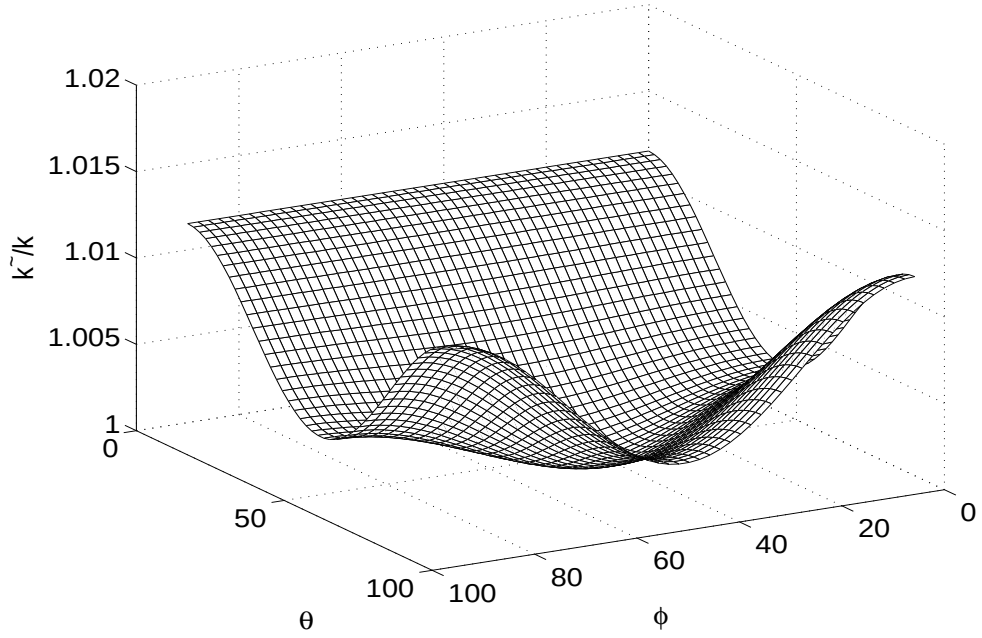

Fig. 2.15. Three-dimensional dispersion of the Yee algorithm ($S = 0.577, N = 10$).

2.5.2. The FDTD(2,4) Scheme

For conciseness, only the three-dimensional dispersion of FDTD(2,4) is discussed in this section. The 3D dispersion relation for the FDTD(2,4) scheme can be written as

$$\begin{aligned}\left(\frac{1}{c\Delta t}\right)^2 \sin^2\left(\frac{\omega\Delta t}{2}\right) &= \frac{1}{\Delta x^2}\left[\frac{9}{8}\sin\left(\frac{\tilde{k}_x\Delta x}{2}\right)-\frac{1}{24}\sin\left(\frac{3\tilde{k}_x\Delta x}{2}\right)\right]^2 \\ &+ \frac{1}{\Delta y^2}\left[\frac{9}{8}\sin\left(\frac{\tilde{k}_y\Delta y}{2}\right)-\frac{1}{24}\sin\left(\frac{3\tilde{k}_y\Delta y}{2}\right)\right]^2 \\ &+ \frac{1}{\Delta z^2}\left[\frac{9}{8}\sin\left(\frac{\tilde{k}_z\Delta z}{2}\right)-\frac{1}{24}\sin\left(\frac{3\tilde{k}_z\Delta z}{2}\right)\right]^2 \end{aligned} \quad (2.101)$$

where

$$\tilde{k}_x = \tilde{k}\cos\phi\sin\theta,\ \tilde{k}_y = \tilde{k}\sin\phi\sin\theta,\ \tilde{k}_z = \tilde{k}\cos\theta,$$

For the cubic mesh ($\Delta x = \Delta y = \Delta z = \Delta s$), (2.101) can be rewritten in the form of

$$\begin{aligned}\frac{1}{S^2}\sin^2\left(\frac{\pi S}{N}\right) &= \left[\frac{9}{8}\sin\left(\frac{\pi\cos\phi\sin\theta}{N}\frac{\tilde{k}}{k}\right)-\frac{1}{24}\sin\left(\frac{3\pi\cos\phi\sin\theta}{N}\frac{\tilde{k}}{k}\right)\right]^2 \\ &+ \left[\frac{9}{8}\sin\left(\frac{\pi\sin\phi\sin\theta}{N}\frac{\tilde{k}}{k}\right)-\frac{1}{24}\sin\left(\frac{3\pi\sin\phi\sin\theta}{N}\frac{\tilde{k}}{k}\right)\right]^2 \\ &+ \left[\frac{9}{8}\sin\left(\frac{\pi\cos\theta}{N}\frac{\tilde{k}}{k}\right)-\frac{1}{24}\sin\left(\frac{3\pi\cos\theta}{N}\frac{\tilde{k}}{k}\right)\right]^2 \end{aligned} \quad (2.102)$$

Notice that the two-dimensional dispersion relation can be readily obtained by forcing $\theta = 90^\circ$ in (2.101) or (2.102). The one-dimensional dispersion relation can be obtained by forcing ($\theta = 90^\circ, \phi = 0^\circ$) in (2.101) or (2.102). The one-dimensional dispersions versus mesh resolution N for different S are plotted in Fig. 2.16. As shown, all the curves approach unity when N increases. However, the dispersion characteristic of the FDTD(2,4) scheme is very different from that of the FDTD (2,2) scheme. There is an optimum S value (S_{opt}) for each N where the dispersion is minimized to zero [66]. When S deviates from S_{opt}, the

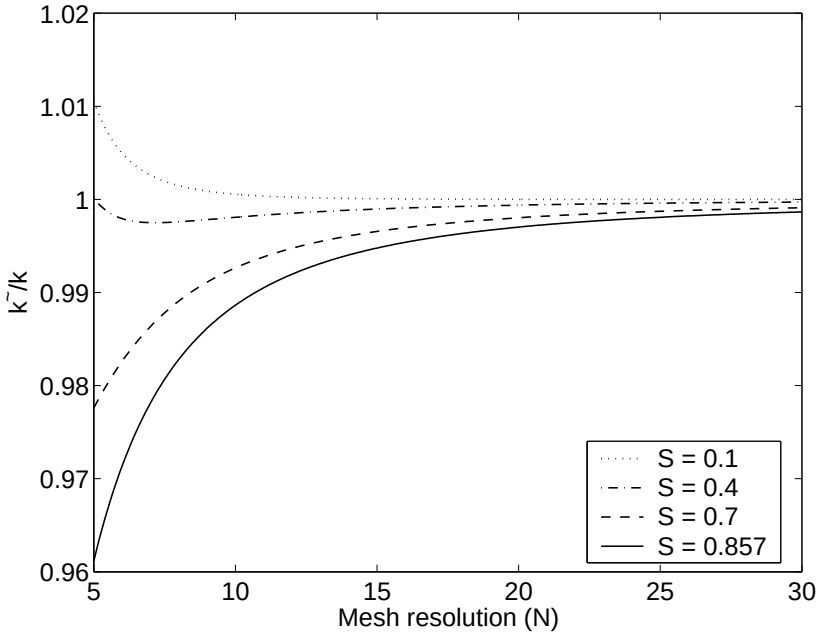

Fig. 2.16. One-dimensional dispersion of the FDTD(2,4) algorithm.

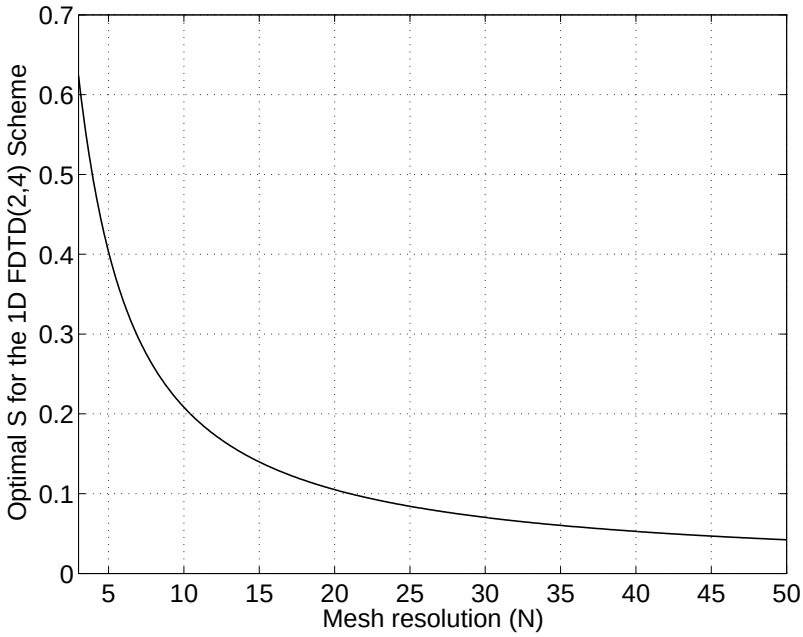

Fig. 2.17. Optimal S for the 1D FDTD(2,4) algorithm.

discrepancy between $\tilde{k}$ and k increases. Also notice that if $S < S_{opt}$, $\tilde{k} > k$; if $S > S_{opt}$, $\tilde{k} < k$. The optimum S value can be found by forcing $\tilde{k} = k$ in the dispersion relation and solving the resultant nonlinear equation. For the 1D FDTD(2,4), S_{opt} versus N is plotted in Fig. 2.17. Notice that the expected fourth-order convergence is not observed in Fig. 2.16. The convergence rate of the FDTD(2,4) is only second-order. This can be attributed to the fact that the error generated by the time-domain discretization is still second order, which deteriorates the accuracy of the entire scheme unless Δt is sufficiently small.

Next, the 2D dispersion of the FDTD(2,4) scheme will be discussed. For $S = 0.5$, the 2D dispersion versus propagation angles for different N is plotted in Fig. 2.18. Different from Yee's algorithm, the maximum discrepancy occurs along 45°, and the minima are along the principal axes. As N increases, the absolute value of the dispersion and the anisotropy decreases. For a fixed mesh resolution $N = 10$, the dispersion versus propagation angles for different S is plotted in Fig. 2.19. Similar as the FDTD(2,2) case, the shapes of all curves remain identical. When S deviates the optimum value, the dispersion curves shifts away from unity.

To complete the discussion, the 3D dispersion plots of the standard FDTD(2,4) scheme are also presented. Firstly, the Courant number is fixed to $S = 0.4$, $\tilde{k}/k$ versus propagation angles for $N = 5$ and $N = 10$ is plotted in Figs. 2.20 and 2.21, respectively. It is evident that using a finer mesh resolution greatly reduces the anisotropy of the dispersion. Secondly, when the mesh resolution is fixed to $N = 10$, $\tilde{k}/k$ versus propagation angles for $S = 0.49$ and $S = 0.15$ is plotted in Figs. 2.22 and 2.23, respectively. As shown, the shapes of dispersion are identical but they are shifted.

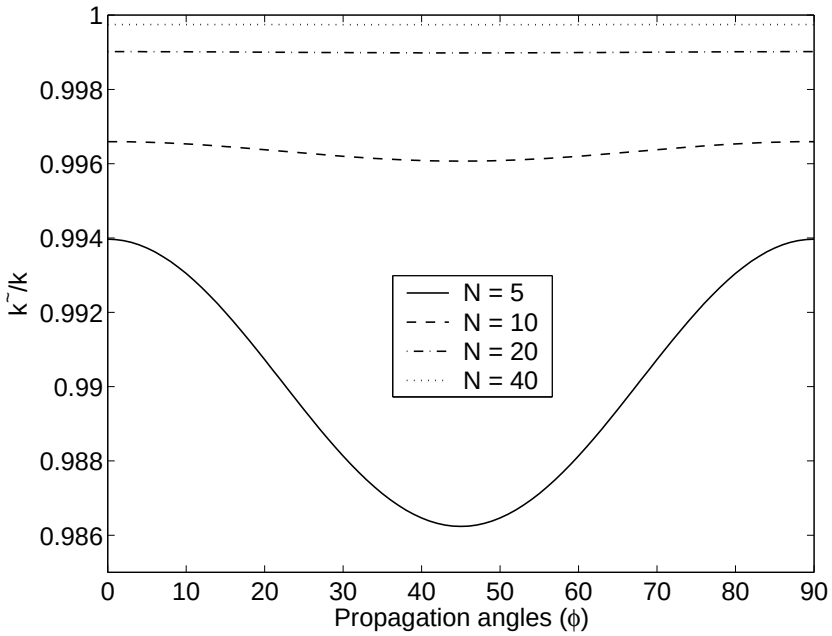

Fig. 2.18. Two-dimensional dispersion of Fang's algorithm ($S = 0.5$).

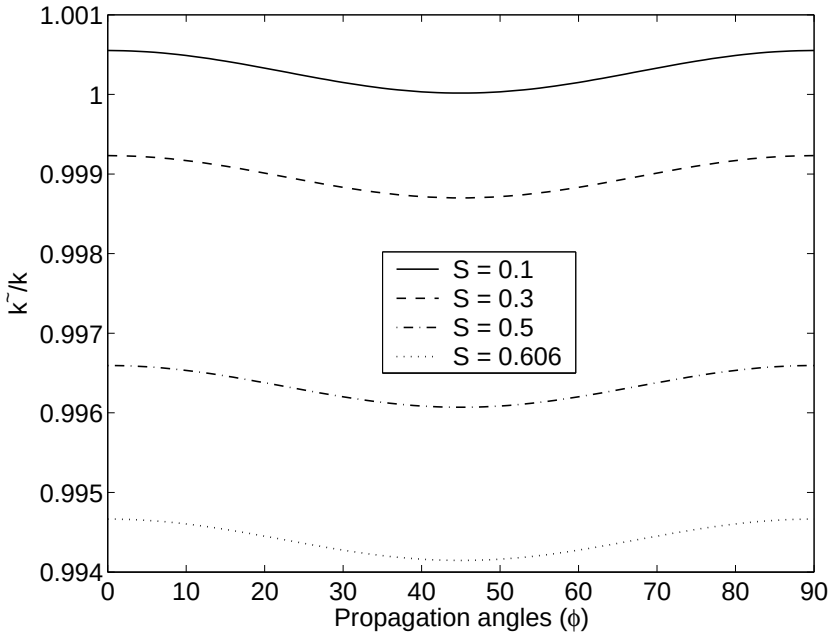

Fig. 2.19. Two-dimensional dispersion of Fang's algorithm ($N = 10$).

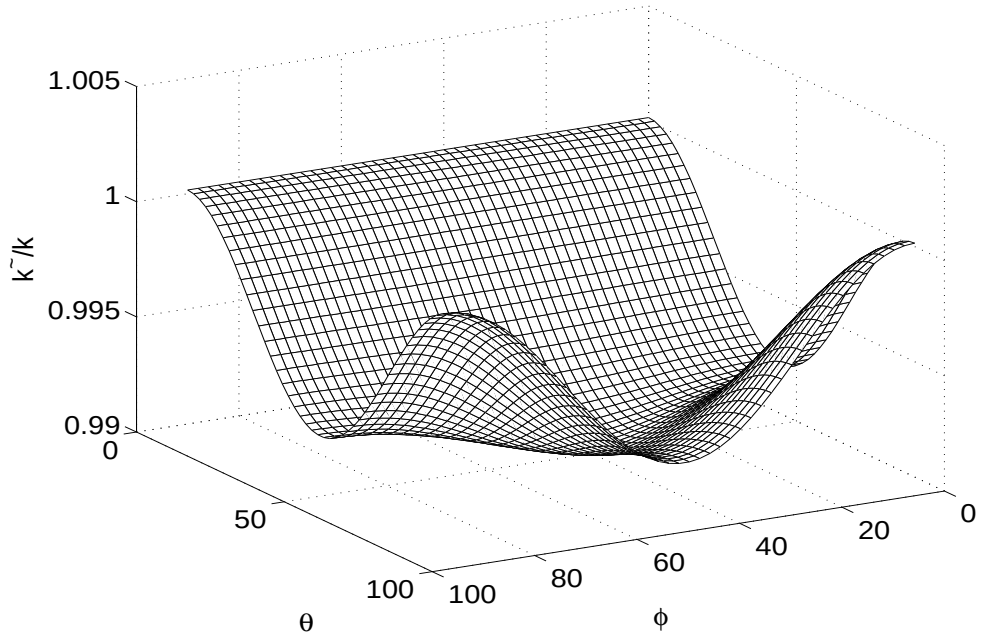

Fig. 2.20. Three-dimensional dispersion of the FDTD(2,4) algorithm ($N = 5$).

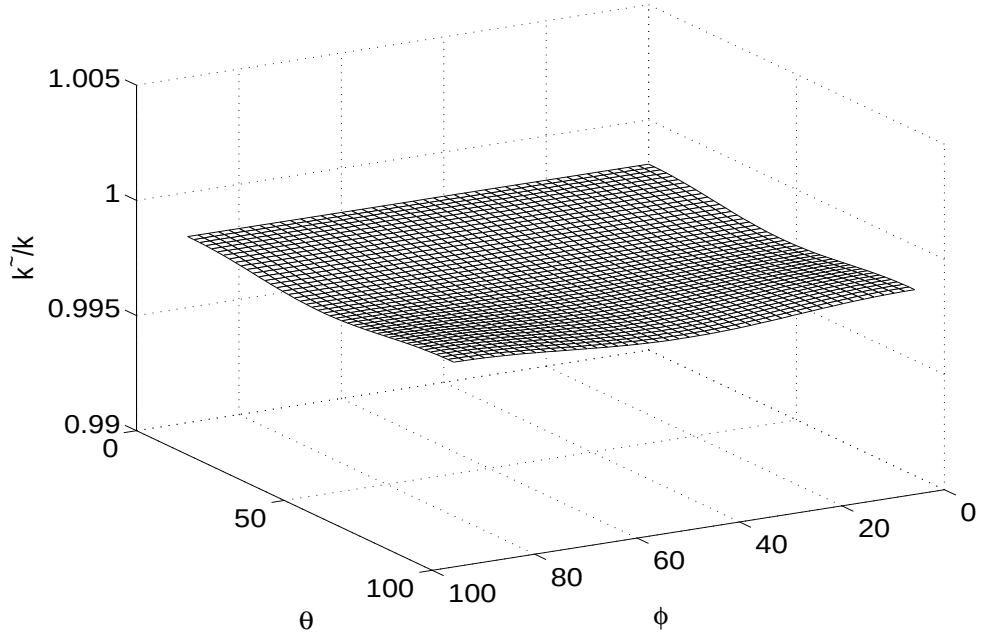

Fig. 2.21. Two-dimensional dispersion of the FDTD(2,4) algorithm ($N = 10$).

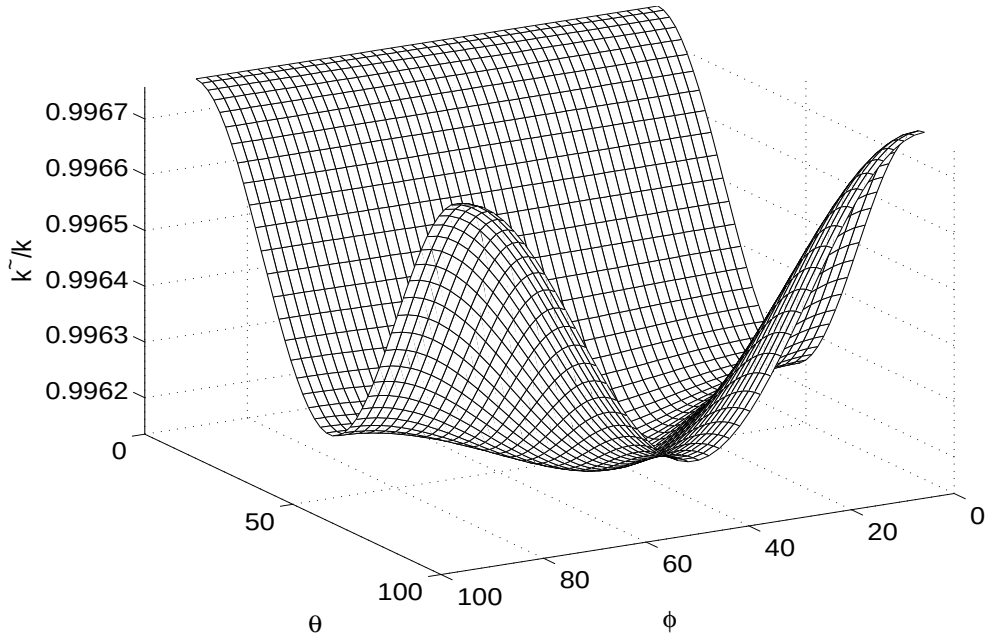

Fig. 2.22. Three-dimensional dispersion of the FDTD(2,4) algorithm ($S = 0.49$).

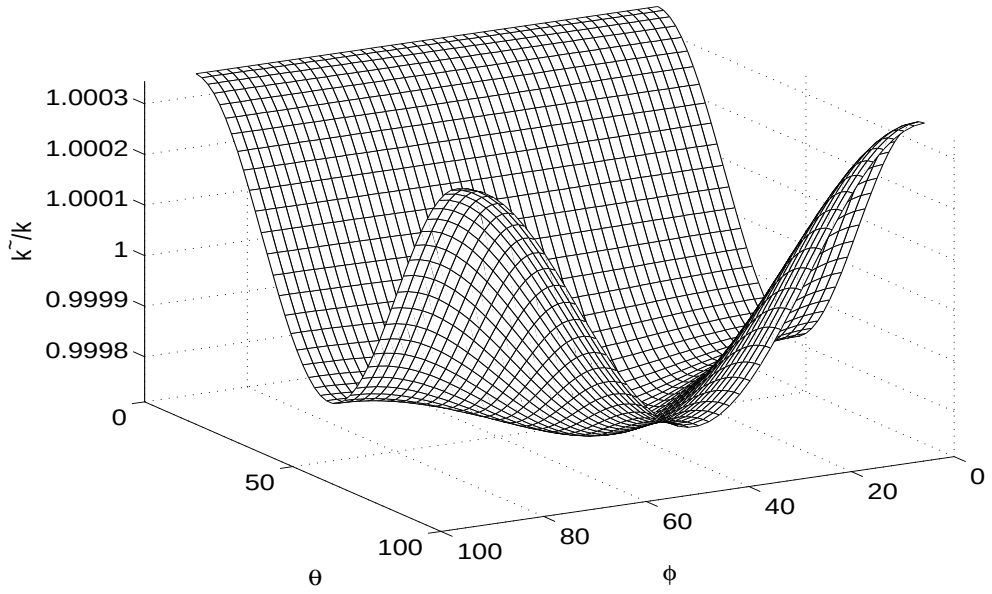

Fig. 2.23. Two-dimensional dispersion of the FDTD(2,4) algorithm ($S = 0.15$).

2.5.3. The FDTD(2,N) Schemes

The dispersion relation for any FDTD(2,N) scheme can be expressed as [86]

$$\left(\frac{1}{c\Delta t}\right)^2 \sin^2\left(\frac{\omega\Delta t}{2}\right) = \sum_{\xi=x,y,z} \frac{1}{\Delta\xi^2} \left\{ \sum_{n=1}^{N/2} C_n \sin\left[\frac{(2n-1)\tilde{k}_\xi \Delta\xi}{2}\right] \right\}^2 \tag{2.103}$$

The left-hand-side of (2.103) depicts the time-domain discretization error while the right-hand-side describes the error generated by the space-domain discretization. For the standard FDTD(2,N) algorithms, three important arguments can be made:

- Both the space and time discretization errors contribute to the total dispersion of the scheme. In order to achieve the highest possible accuracy, it is important to balance the orders of accuracy of the time- and space-discretizations.

- The time-domain discretization errors are identical along any propagation direction (isotropic). The effect of varying the Courant number is to shift the dispersion curve. Depending on the schemes, there is an optimum S value that minimize the dispersion for each mesh resolution.

- The errors generated by the space discretization are anisotropic. The use of a finer mesh resolution decreases the anisotropy.

In order to achieve a high accuracy, ideally the time domain scheme needs to be at least N-th order. However, for simplicity, a popular treatment is to use an FDTD(2,N) scheme with a small time-step [33]. Moreover, the space domain scheme is more critical since it controls both the absolute value and the anisotropy of the dispersion.

In summary, the derivation of the standard FDTD schemes are based on the Taylor series expansion. The coefficients of the stencils are selected to minimize the leading

truncation error. These coefficients might not be the optimal in terms of the dispersion error. Alternative methods, with the ultimate goal of minimizing the dispersion error are still highly desirable. Such methods include the nonstandard FDTD schemes which are constructed directly based on the dispersion analysis. In the following chapter, the fundamental theory of the nonstandard FDTD schemes will be introduced.

CHAPTER 3

THE NONSTANDARD FINITE-DIFFERENCE METHODS

In Chapter 2, we introduced the fundamental theory of the Standard Finite-Difference Methods (SFD), from the simplest Yee's algorithm to the more complex Higher-Order FDTD (HOFDTD). Using the Taylor series expansion, the coefficients for the SFD stencils are derived by minimizing the leading truncation error. Usually, the advantage of the HOFDTD becomes obvious only if the mesh resolution is refined. However, for electrically large problems, a very coarse mesh resolution usually has to be used due to the tight budget of the available computer memories. In addition, for the unbalanced schemes, such as the FDTD(2,4) scheme, the gain of accuracy in the space domain could be deteriorated by the large time-domain errors unless a sufficiently small time step is used. Consequently, it is questionable whether or not the coefficients for the SFD stencils are optimal in terms of dispersion. Instead of the pursuit of the higher-order, alternative methods with the ultimate goal of low-dispersion are more practical. The Nonstandard Finite-Difference Methods (NSFD) are such schemes that are constructed directly based upon the dispersion analysis. The concept of the NSFD was first proposed by Mickens [37]. Then, Cole applied the NSFD to solve the Maxwell's equations [40], [41]. In this report, the NSFD methods refer, in its broadest sense, to those schemes which are modified based upon the SFD schemes to further reduce the dispersion. To distinguish with the SFD methods, an NSFD scheme using M- and N-point stencils in the time and space domains will be designated as the (NS)MN scheme. Notice, (M, N) no longer represents the order of accuracy.

In this chapter, the fundamentals of the NSFD method will be first reviewed for the 1D case. Then the performance of the basic 1D NS22 scheme and its direct extension, the

NS24 scheme, will be discussed. For multi-dimensional cases, an improved NSFD method (INS) will be presented. Furthermore, the concept of the NSFD will be generalized to construct a more General NSFD method (GNS). Both the dispersion analysis and the numerical simulations will be demonstrated. Afterwards, Gauss's Law for the NSFD methods will be examined. Finally, to reduce the errors generated at the material discontinuities, two material interface conditions will be developed for the NSFD methods with extended stencils.

3.1. The One-Dimensional NS22 Scheme

For clarity, the discussion of the NSFD methods starts with the one-dimensional NS22 scheme, which uses a two-point stencil in both the time and space domains.

3.1.1. Fundamental of the NS22 scheme

The standard way to approximate a partial derivative is to use the second-order central-difference operator introduced in Chapter 2. For example, the space derivative with respect to x can be written as

$$\frac{\partial}{\partial x} f_i \approx \frac{f_{i+1/2} - f_{i-1/2}}{\Delta x} = \left(\frac{\tilde{d}_x^{2nd}}{\Delta x} \right) f_i \tag{3.1}$$

where $\tilde{d}_x^{2nd}$ represents the numerator of the standard second-order central-difference. If one substitutes the monochromatic wave-equation solution $f_0 = e^{-jk_0x}$ into $\tilde{d}_x^{2nd}$, it turns out [37], [40]

$$\begin{aligned} \tilde{d}_x^{2nd}(e^{-jk_0x}) &= \left[\frac{2}{k_0} \sin\left(\frac{k_0 \Delta x}{2} \right) \right] \cdot (-jk_0 e^{-jk_0x}) \\ &= sk_{x0}^2 \cdot \left[\frac{\partial}{\partial x}(e^{-jk_0x}) \right] \end{aligned} \tag{3.2}$$

where

$$sk_{x0}^2 = \frac{2}{k_0}\sin\left(\frac{k_0\Delta x}{2}\right)$$

Clearly, the result on the right hand side is the exact solution multiplied by a constant sk_{x0}^2. Dividing both sides of (3.2) by sk_{x0}^2 yields

$$\left(\frac{\tilde{d}_x^{2nd}}{sk_{x0}^2}\right)(e^{-jk_0x}) = \frac{\partial}{\partial x}(e^{-jk_0x}) \tag{3.3}$$

That is, the new operator $D_x^{ns22} = [(\tilde{d}_x^{2nd})/(sk_{x0}^2)]$ gives the exact solution at one single frequency (k_0) along the x axis. Based on this observation, the *space-domain* NS22 operators are defined as

$$D_\xi^{ns22} f_\xi = \frac{f_{\xi+1/2} - f_{\xi-1/2}}{sk_{\xi0}^2}, \xi = x, y, z \tag{3.4}$$

where

$$sk_{\xi0}^2 = \frac{2}{k_0}\sin\left(\frac{k_0\Delta\xi}{2}\right)$$

A similar procedure is followed to derive the *time-domain* NS22 operator which can be expressed as

$$D_t^{ns22} f^n = \frac{f^{n+1/2} - f^{n-1/2}}{s\omega_0^2} \tag{3.5}$$

where

$$s\omega_0^2 = \frac{2}{\omega_0}\sin\left(\frac{\omega_0\Delta t}{2}\right) \tag{3.6}$$

Notice that $sk_{\xi0}^2$ depends on k_0 and $\Delta\xi(\xi = x, y, z)$; $s\omega_0^2$ is determined by ω_0 and Δt. Thus, the correction parameters $sk_{\xi0}^2$ and $s\omega_0^2$ can be considered, respectively, as the *frequency-optimized space and time increments*. To apply the NS22 algorithm, one only needs to replace the space and time steps $(\Delta\xi, \Delta t)$ in Yee's algorithm by their frequency-optimized counterparts sk_0^2 and $s\omega_0^2$, respectively.

3.1.2. Dispersion Analysis

In this section, we will explore the basic properties of the 1D NS22 scheme by analyzing its dispersion characteristics. Following a similar procedure introduced in Section 2.5, the 1D dispersion relation for the NS22 scheme can be derived and written as

$$\sin^2\left(\frac{k_0\Delta z}{2}\right)\sin^2\left(\frac{\omega\Delta t}{2}\right) = \sin^2\left(\frac{\omega_0\Delta t}{2}\right)\sin^2\left(\frac{\tilde{k}\Delta z}{2}\right) \tag{3.7}$$

where ω_0 is the design angular frequency and k_0 is the corresponding exact wave number at the design frequency. Equation (3.7) can be rewritten as

$$\sin^2\left(\frac{\pi}{N_0}\right)\sin^2\left(\frac{\pi S}{N}\right) = \sin^2\left(\frac{\pi S}{N_0}\right)\sin^2\left(\frac{\pi}{N}\frac{\tilde{k}}{k}\right) \tag{3.8}$$

where $S = c\Delta z/\Delta t$ is the Courant number; N and N_0 represent the mesh resolution at an arbitrary and at a design frequency, respectively. Notice that when $N = N_0$, the two terms containing S in (3.7) cancel out, which imply zero dispersion ($\tilde{k}/k = 1$) at $N = N_0$.

To better demonstrate the characteristic of the dispersion, the local dispersion error is defined as

$$E_{loc} = \left(1 - \frac{\tilde{k}}{k}\right) \tag{3.9}$$

Fig. 3.1 illustrates the absolute values of the local dispersion errors, for a fixed design mesh resolution $N_0 = 10$ and various Courant numbers S. The local dispersion errors of Yee's algorithm are also plotted as references. The figure clearly shows that, for the NS22 scheme, the dispersion error is extremely low at $N = N_0$. However, compared to the errors generated by Yee's algorithm, this excellent low-dispersion performance only presents in the vicinity of N_0. If N is increased from N_0 to infinity, the dispersion error of the NS22 scheme could be even worse than that of Yee's algorithm. Similar to the Yee algorithm, using a Courant

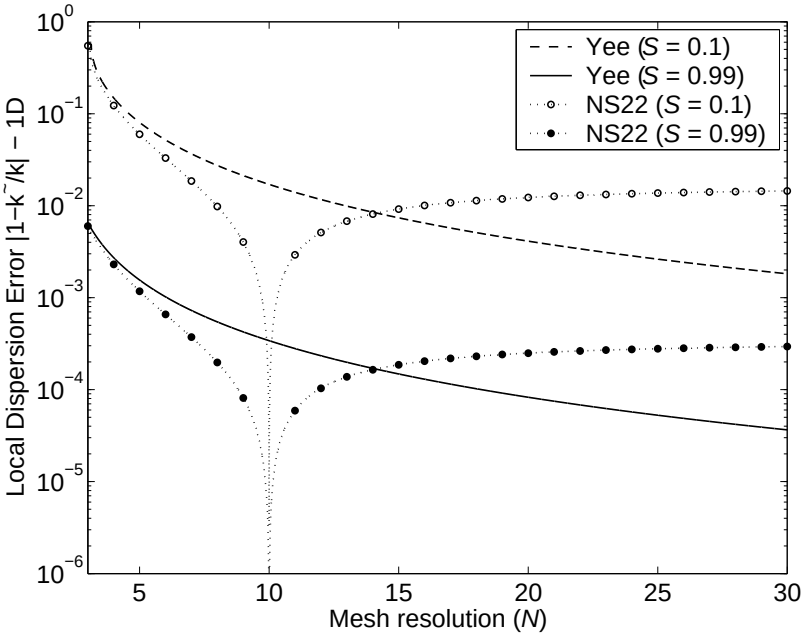

Fig. 3.1. One-dimensional local dispersion error of the NS22 scheme ($N_0 = 10$).

number which is as close as possible to the Courant limit helps reduce the overall dispersion error of the NS22 scheme. Therefore, the NS22 scheme is a *narrow-band* algorithm in terms of the dispersion, which is suitable for single-frequency simulations. The local dispersion errors versus N for a fixed Courant number $S = 0.5$ and $N_0 = 10, 20$ are plotted in Fig. 3.2. It is evident that the dispersion null of the NS22 scheme can be readily shifted by choosing different N_0. As N_0 approaches infinity, the NS22 curve asymptotically approaches the curve of Yee's algorithm. Notice that, for $N < N_0$ (higher frequency region for a fixed space step), the dispersion error of the 1D NS22 scheme is always smaller than that of the Yee algorithm. Bearing in mind that the higher-frequency signals usually generate greater dispersion error. This fact indicates that the NS22 scheme still can be used for the broad-band simulations if one selects an appropriate N_0.

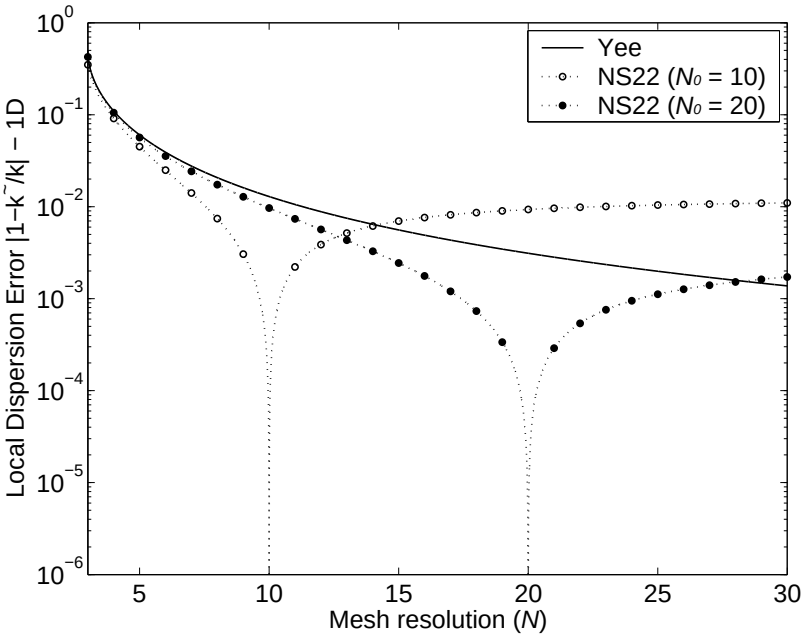

Fig. 3.2. One-dimensional local dispersion error of the NS22 scheme ($S = 0.5$).

3.1.3. Numerical Simulations

In this section, the characteristics of the 1D NS22 scheme will be demonstrated through numerical simulations. As a first example, a continuous sinusoid wave with $f_0 = 2$GHz is generated at the center of an 1D free-space region. The 1D space is large enough so that the traveling waves will never reach the domain boundaries within the duration of interest. The space step and the Courant number are set to $\Delta z = 0.01$ m ($\lambda/15$ at f_0) and $S = 0.5$, respectively. A snapshot is taken for the magnitude of the E field at $t = 1000\Delta t$. The snapshots for both the Yee and the NS22 schemes are zoomed near $200\Delta z$ and plotted in Fig. 3.3. It is evident that the solution predicted by the NS22 has an excellent agreement with the analytical solution. However, the results provided by Yee's algorithm exhibits a phase lag of about 24°. For a longer simulation time, this phase discrepancy is even greater

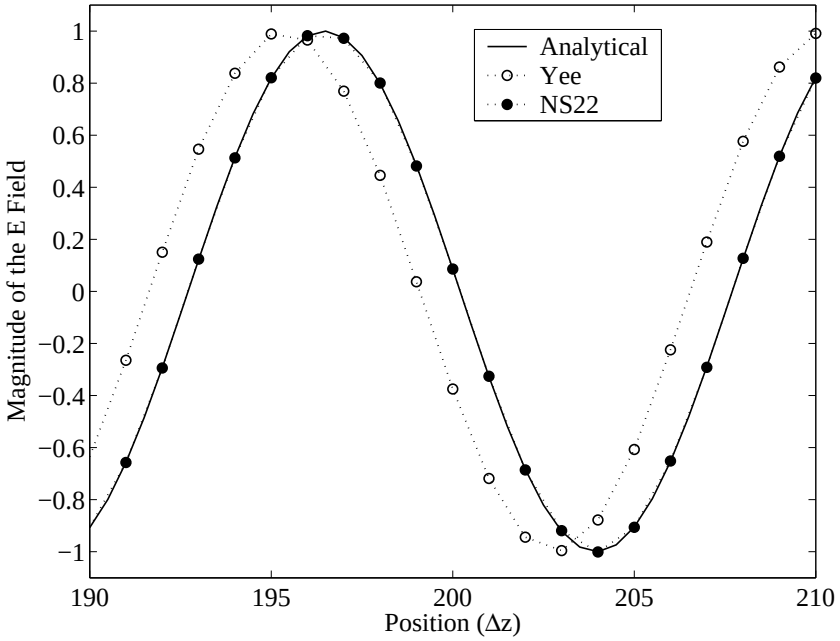

Fig. 3.3. Propagation of the 1D sinusoid waves ($\Delta z = 0.01$m,$S = 0.5$).

due to the accumulation of the dispersion. However, if $S = 1$, the 1D Yee's algorithm and NS22 scheme both produce the exact solution.

A second simulation is a half-wavelength dielectric slab ($\epsilon_r = 16$) in a free-space region [37]. The space step and the Courant number are set to $\Delta z = 0.0025$m and $S = 0.99$ in terms of the speed of light in free-space region, respectively. The incident wave is a sequence of a sinusoid wave with $f_0 = 3$GHz, as shown in the first subplot of Fig. 3.4. Ideally, there is no reflection if the sequence is infinitely long. An average permittivity is applied along the material interface. Notice that there is almost no dispersion in the free-space region since S is very close to the "magic time step" $S = 1$. The errors are dominated by the phase error inside the slab and the nonphysical errors generated by the material discontinuities. The reflected and the transmitted E fields at $t = 1100\Delta t$, predicted by the Yee and the NS22

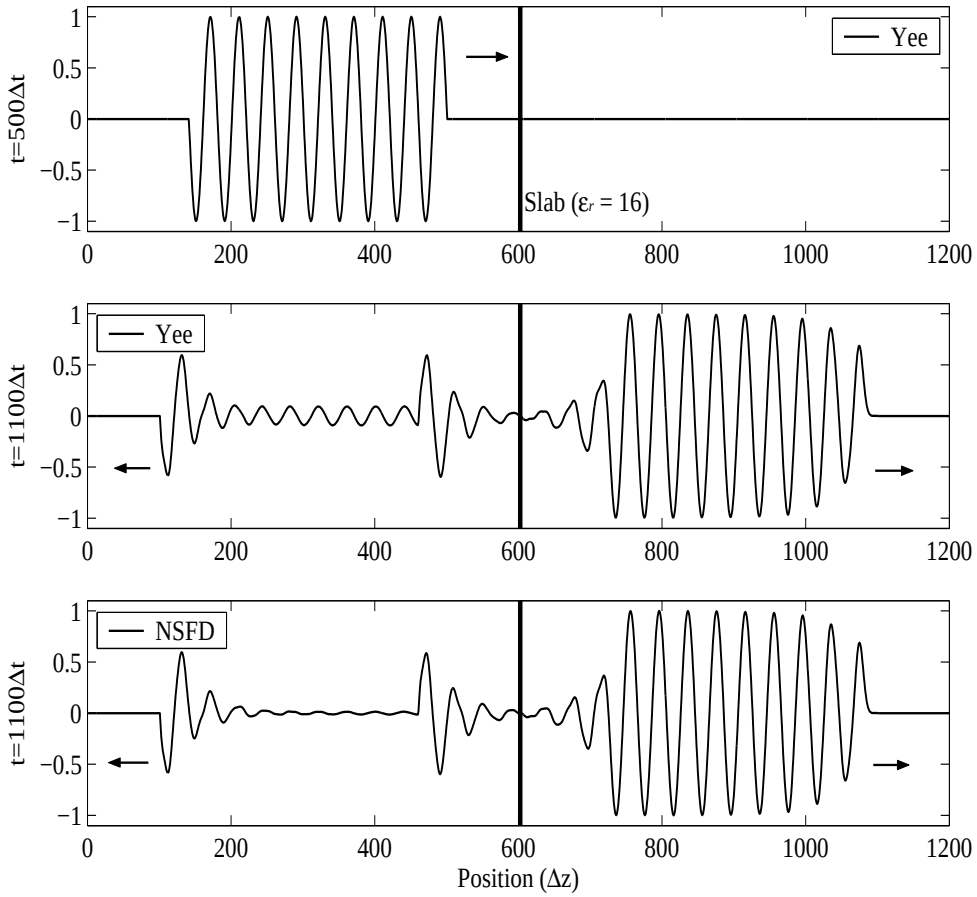

Fig. 3.4. The reflection and transmission due to the dielectric slab ($\Delta z = 0.0025$m,$S = 0.99$).

schemes, are plotted in the second and third subplots of Fig. 3.4. As shown, large reflections are observed at both ends of the reflected sequence due to the signal discontinuities there. As shown, the results predicted by Yee's algorithm exhibit large reflection along the center part of the reflected wave. This can be attributed by the dispersion of Yee's algorithm which makes the thickness of the slab no longer half wavelength. However, the NS22 scheme has the freedom to choose the sk value inside the material which automatically adjust the phase speed. It is evident, the results predicted by the NS22 scheme present much smaller reflections. Based on the above observations, NSFD algorithm is suitable for problems which require accurate phase cancelation at a single operating frequency.

Both of the previous examples are single-frequency simulations. However, whether the NSFD algorithm is capable of simulating broad-band signals remains a question. To explore the broad-band performance of the NSFD algorithm, a Gaussian pulse with $(\alpha = 30, \beta = 10)$ is generated in the 1D free-space region. The space step and the Courant number are set to $\Delta z = 0.01$m and $S = 0.5$, respectively. The frequency spectrum of the Gaussian pulse is plotted in Fig. 3.5. As shown, the Gaussian pulse contains significant low-frequency components. The -3dB frequency of the Gaussian pulse is located at about $f_{3dB} = 1.6$ GHz. For the NS22 scheme, the design frequency is set to f_{3dB}. The snapshots of the E field at $t = 500\Delta t$ for the Yee and the NS22 schemes are plotted in Fig. 3.6. As shown, the pulses predicted by the Yee and NS22 schemes suffer from similar level of phase errors. This example suggests that, by properly choosing a design mesh resolution, the NSFD algorithm may generate dispersion errors no worse than Yee's algorithm.

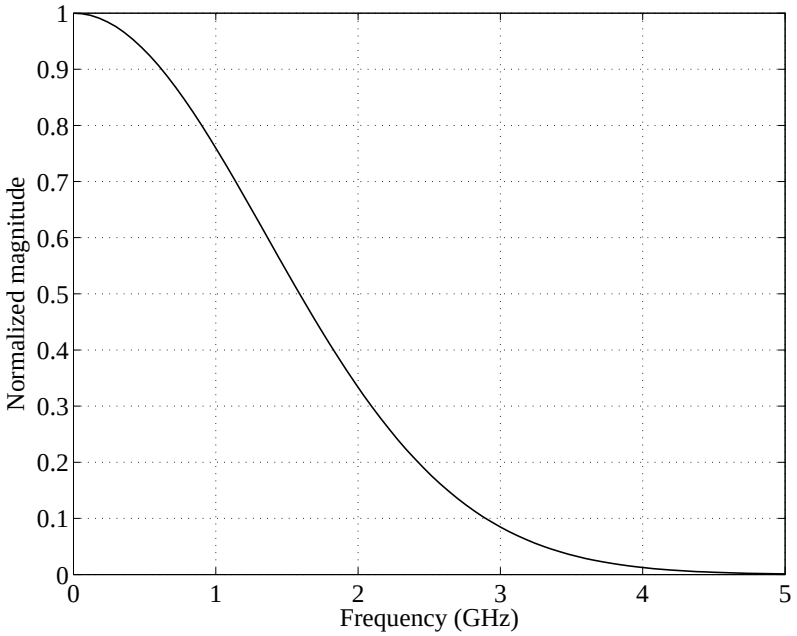

Fig. 3.5. Frequency spectrum of a Gaussian pulse ($\alpha = 30, \beta = 10$).

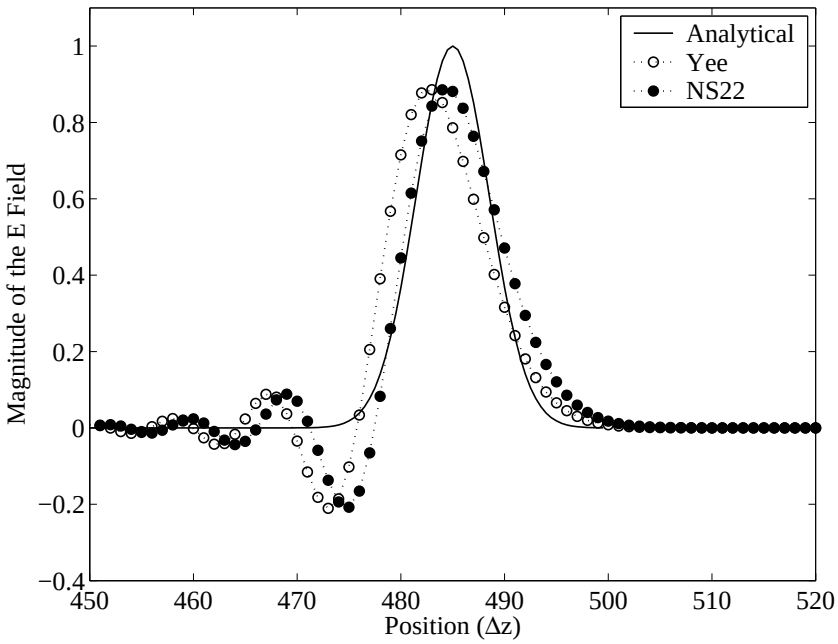

Fig. 3.6. Propagation of the 1D Gaussian pulse ($\Delta z = 0.01$m,$S = 0.5$)

3.2. The One-Dimensional NS24 Scheme

The basic concept of the NS22 scheme can be readily extended to Fang's FDTD (2,4) algorithm [15] to construct a NS24 scheme [90], [91]. Following a similar procedure, the space-domain NS24 operator can be defined as

$$D_{\xi}^{ns24} f_{\xi} = \frac{\frac{27}{24}(f_{\xi+1/2} - f_{\xi-1/2}) - \frac{1}{24}(f_{\xi+3/2} - f_{\xi-3/2})}{sk_{\xi 0}^4},\ \xi = x, y, z \tag{3.10}$$

where

$$sk_{\xi 0}^4 = \frac{2}{k_0} \sin\left[\frac{27}{24} \sin\left(\frac{k_0 \Delta\xi}{2}\right) - \frac{1}{24} \sin\left(\frac{3k_0 \Delta\xi}{2}\right)\right] \tag{3.11}$$

Similar to the NS22 case, $sk_{\xi 0}^4$ can be considered as the frequency-optimized space step. Since the same second-order stencil is used in the time domain, the time-domain NS24 operator remains the same as in (3.5). To apply the NS24 algorithm, one needs to replace the space and time steps $(\Delta\xi, \Delta t)$ in the regular FDTD (2,4) algorithm by their frequency-optimized counterparts sk_0^4 and $s\omega_0^2$, respectively.

The dispersion relation of the 1D NS24 scheme can be readily derived and expressed as

$$\left[\frac{9}{8} \sin\left(\frac{k_0 \Delta z}{2}\right) - \frac{1}{24} \sin\left(\frac{3k_0 \Delta z}{2}\right)\right]^2 \sin^2\left(\frac{\omega \Delta t}{2}\right) = \sin^2\left(\frac{\omega_0 \Delta t}{2}\right) \left[\frac{9}{8} \sin\left(\frac{\tilde{k} \Delta z}{2}\right) - \frac{1}{24} \sin\left(\frac{3\tilde{k} \Delta z}{2}\right)\right]^2 \tag{3.12}$$

Comparing to the dispersion relation of the 1D NS22 scheme in (3.7), the only difference is the first term on the left hand side. Similarly, the dispersion relation of (3.12) can be

rewritten as

$$\left[\frac{9}{8}\sin\left(\frac{\pi}{N_0}\right)-\frac{1}{24}\sin\left(\frac{3\pi}{N_0}\right)\right]^2\sin^2\left(\frac{\pi S}{N}\right) = \sin^2\left(\frac{\pi S}{N_0}\right)\left[\frac{9}{8}\sin\left(\frac{\pi}{N}\frac{\tilde{k}}{k}\right)-\frac{1}{24}\sin\left(\frac{3\pi}{N}\frac{\tilde{k}}{k}\right)\right]^2 \tag{3.13}$$

It can be expected that the dispersion error curve of the NS24 scheme will present a null which is located at $N = N_0$. It has been indicated in Section 2.5 that, for the FDTD(2,4) scheme, there could be a second null which is controlled by the Courant number S. To control the position of the two nulls of the NS24 scheme, we can specify two design mesh resolutions N_0 and N_1. The desired S value can be found as follows. Firstly, $\tilde{k}/k$ is forced to unity in (3.13). Then substituting $N = N_1$ into (3.13) yields

$$\left[\frac{9}{8}\sin\left(\frac{\pi}{N_0}\right)-\frac{1}{24}\sin\left(\frac{3\pi}{N_0}\right)\right]^2\sin^2\left(\frac{\pi S}{N_1}\right) = \left[\frac{9}{8}\sin\left(\frac{\pi}{N_1}\right)-\frac{1}{24}\sin\left(\frac{3\pi}{N_1}\right)\right]^2\sin^2\left(\frac{\pi S}{N_0}\right) \tag{3.14}$$

Solving (3.14) using the Newton-Ralphson method, the desired S value can be readily obtained. Notice that, due to the symmetry of the equation, switching N_0 and N_1 in (3.14) will not affect the result. The computed S values for various (N_0 and N_1) combinations are summarized in Table 3.1.

Table 3.1. Computed S values for various N_0 and N_1

	N_0	N_1	S
Case 1	17.5	17.5	0.1693
Case 2	15	20	0.1745
Case 3	25	10	0.2243

The local dispersion errors of each of the Case in Table 3.1 are plotted in Figs. 3.7 - 3.9, respectively. It is evident that the dispersion nulls are located precisely at the design mesh

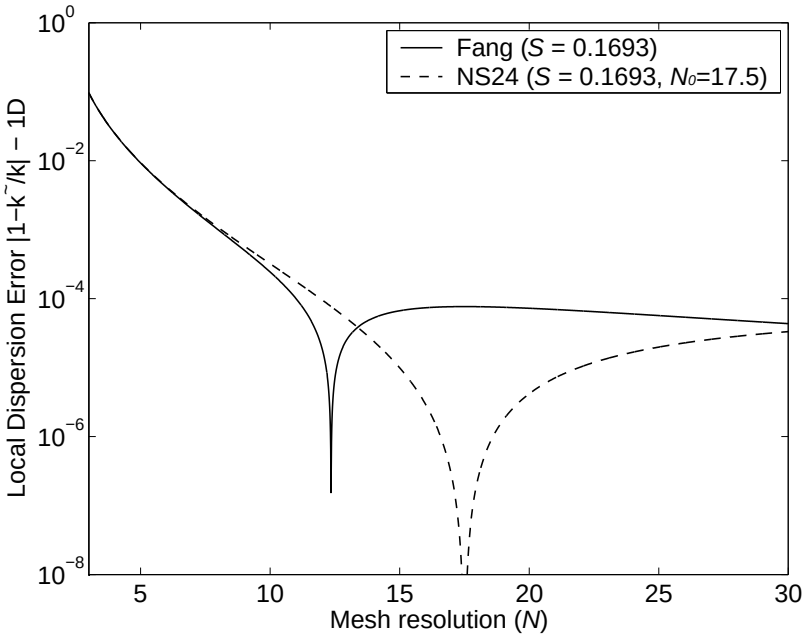

Fig. 3.7. One-dimensional local dispersion error of the NS24 scheme ($N_0 = 17.5, S = 0.1693$).

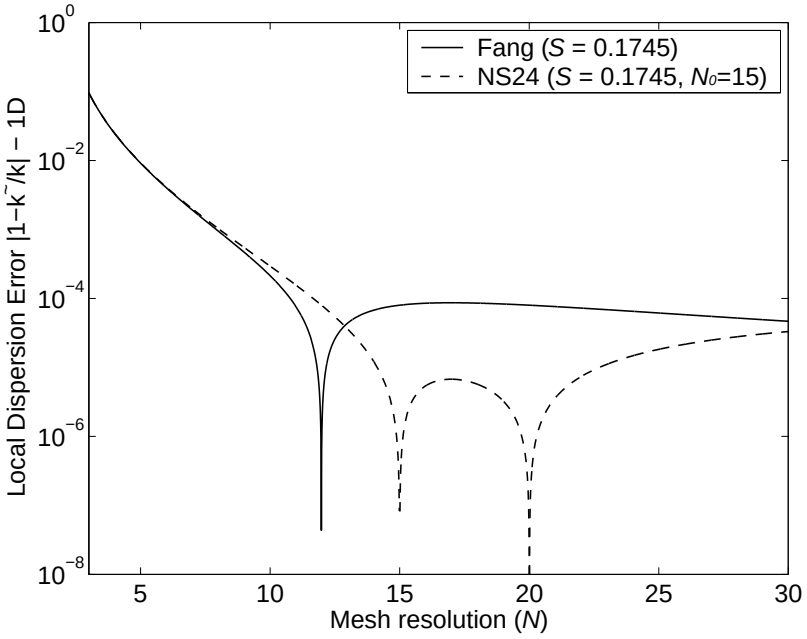

Fig. 3.8. One-dimensional local dispersion error of the NS24 scheme ($N_0 = 15, S = 0.1745$).

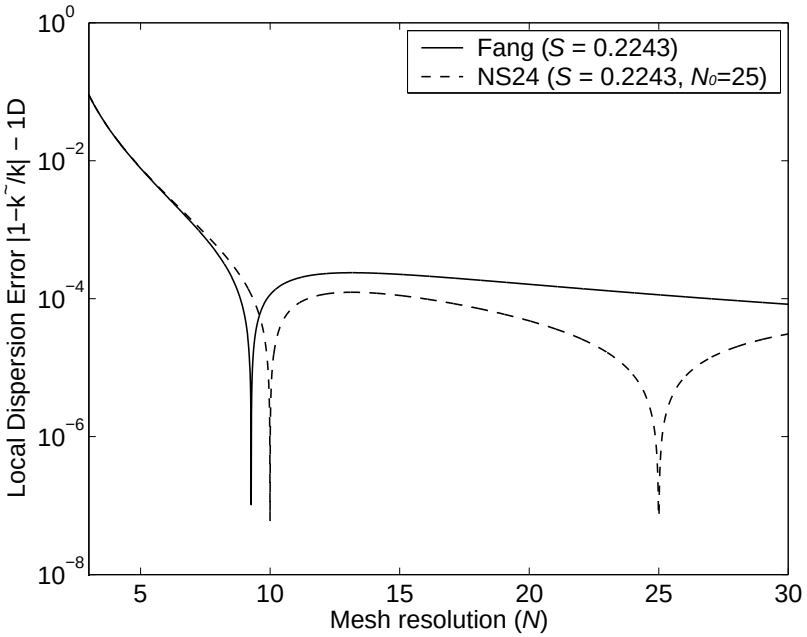

Fig. 3.9. One-dimensional local dispersion error of the NS24 scheme ($N_0 = 25, S = 0.2243$).

resolutions (N_0 and N_1). By choosing different combinations of N_0 and N_1, it is possible to control the low-dispersion band width for the 1D NS24 scheme.

3.3. The Anisotropy for the Multi-Dimensional NSFD schemes

The NSFD algorithms discussed so far are limited to the one-dimensional domain. For the multi-dimensional cases, the ideal performance of the 1D NSFD schemes could be totally deteriorated by another nonphysical artifact: the anisotropy. To best demonstrate this issue, we start the discussion with the dispersion analysis for the multi-dimensional NS22 scheme.

The multi-dimensional NSFD schemes are constructed by simply replacing the time and space increments (Δt and $\Delta \xi$) by their nonstandard counterparts. Following a similar

procedure, the dispersion relations of the multi-dimensional NSFD schemes can be readily obtained. The general 3D dispersion relation of the NS22 scheme can be expressed as

$$\frac{1}{\sin^2\left(\omega_0\Delta t/2\right)}\ \sin^2\left(\frac{\omega\Delta t}{2}\right)=\sum_{\xi=x,y,z}\frac{1}{\sin^2\left(k_0\Delta\xi/2\right)}\sin^2\left(\frac{\tilde{k}_\xi\Delta\xi}{2}\right) \tag{3.15}$$

where

$$\tilde{k}_x=\tilde{k}\cos\phi\sin\theta,\ \tilde{k}_y=\tilde{k}\sin\phi\sin\theta,\ \tilde{k}_z=\tilde{k}\cos\theta.$$

For the cubic mesh case ($\Delta x=\Delta y=\Delta z=\Delta s$), this relation reduces to

$$\frac{1}{\sin^2\left(\pi S/N_0\right)}\ \sin^2\left(\frac{\pi S}{N}\right)=\frac{1}{\sin^2\left(\pi/N_0\right)}\sum_{\xi=x,y,z}\sin^2\left(\frac{\pi}{N}\frac{\tilde{k}_\xi}{k}\right) \tag{3.16}$$

where $\tilde{k}/k$ is the ratio of the numerical wave number to the exact wave number; $N_0=\lambda_0/\Delta s$ is the design mesh resolution. The 2D dispersion relations can be readily obtained by forcing $\phi=0^\circ$ in (3.16). Clearly, the dispersion error for the multi-dimensional NSFD schemes is also a function of ϕ.

The 2D local dispersion errors versus the ϕ for the 2D Yee and NS22 schemes are plotted in Fig. 3.10. Only the first quarter is plotted since all the curves are 90° periodic. Although, the NS22 scheme exhibits zero dispersion along the principle axes (0° and 90°), it still suffers from a similar level of anisotropy as does the Yee algorithm.

3.4. The Improved NSFD Schemes

In order to reduce the average dispersion error, a family of methods [1], [53]– [55], [60] was constructed based on shifting the symmetrical center of the dispersion error curve to zero at a design mesh resolution. Using a similar approach, an *improved NSFD method* (INS) [91] is presented in this section. By introducing extra degrees of freedom into the

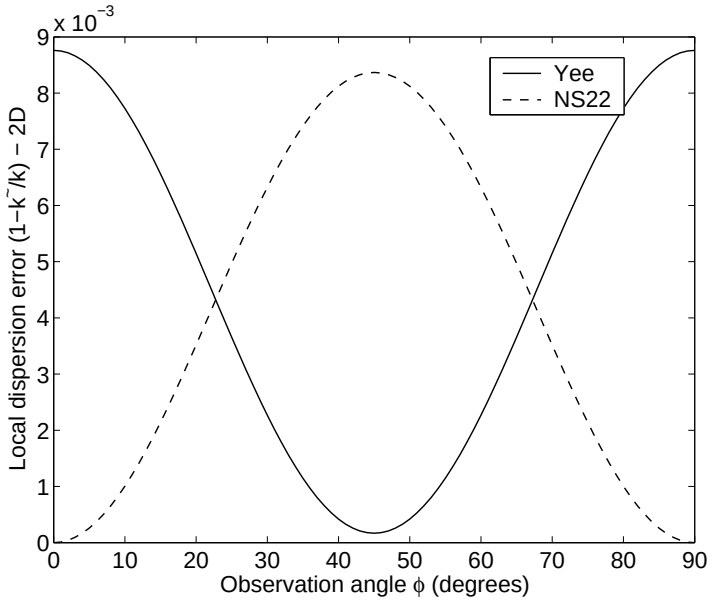

Fig. 3.10. Two-dimensional local dispersion error of the NS22 scheme ($N = N_0 = 10, S = 0.7$).

spatial operators of the regular NSFD methods (the NS22 and INS24 schemes), the INS22 and INS24 methods are able to mitigate the average dispersion error.

3.4.1. The INS22 and INS24 Schemes

Since the derivation of the regular NSFD schemes only considers the plane-wave propagating along the principle axes, $sk_{\xi 0}^2$ and $sk_{\xi 0}^4$ may not be the optimal space steps for waves traveling in other directions. To achieve the optimal correction parameters in the global sense, one can introduce extra degrees of freedom into (3.4) and define the space-domain

INS22 operators as

$$D_x^{ins22} f_x = \frac{f_{x+1/2} - f_{x-1/2}}{a \cdot sk_{x0}^2} \tag{3.17}$$

$$D_y^{ins22} f_y = \frac{f_{y+1/2} - f_{y-1/2}}{b \cdot sk_{y0}^2} \tag{3.18}$$

$$D_z^{ins22} f_z = \frac{f_{z+1/2} - f_{z-1/2}}{c \cdot sk_{z0}^2} \tag{3.19}$$

where a, b, and c are extra free parameters. For simplicity, we only consider the cubic mesh where $\Delta x = \Delta y = \Delta z = \Delta s$. In that case, the free parameters are identical ($a = b = c = 1$). Thus the space domain INS22 operators in (3.17) - (3.19) reduce to

$$D_\xi^{ins22} f_\xi = \frac{f_{\xi+1/2} - f_{\xi-1/2}}{q \cdot sk_{\xi0}^2}, \quad \xi = x, y, z \tag{3.20}$$

Following a similar procedure, the space-domain INS24 operators can be expressed as

$$D_\xi^{ins24} f_\xi = \frac{\frac{9}{8}\left(f_{\xi+1/2} - f_{\xi-1/2}\right) - \frac{1}{24}\left(f_{\xi+3/2} - f_{\xi-3/2}\right)}{q \cdot sk_{\xi0}^4}, \quad \xi = x, y, z \tag{3.21}$$

Notice that the regular NSFD schemes are special cases of the improved NSFD schemes when the free parameter $q = 1$. The values of q can be determined based on the dispersion analysis that follows.

3.4.2. Dispersion Analysis for INS22

The two-dimensional dispersion relation of the INS22 scheme can be found by substituting a harmonic solution to the 2D INS22 update equations. Following a similar notation as in [67], the 2D INS22 dispersion relation can be written as

$$\frac{\sin^2(\pi/N_0)}{\sin^2(\pi S/N_0)} \sin^2\left(\frac{\pi S}{N}\right) = \frac{1}{q^2}\left[\sin^2\left(\frac{\pi \cos\phi}{N}\frac{\tilde{k}}{k}\right) + \sin^2\left(\frac{\pi \sin\phi}{N}\frac{\tilde{k}}{k}\right)\right] \tag{3.22}$$

where $\tilde{k}$ is the numerical wave number, k is the exact wave number, N represents the actual cell numbers per wavelength, N_0 represents the cell numbers per wavelength at the design frequency, and $S = (c\Delta t)/\Delta s$ is the Courant number.

Ideally at the design mesh resolution N_0, we desire the dispersion error to be equal to zero for all propagation angles. That is, in (3.22), $\tilde{k}$ should be equal to k for all angles in the range of $\phi = 0^\circ \sim 90^\circ$ (note that the dispersion curve is 90° periodic) at $N = N_0$. For a finite number of angles (I), this leads to an overdetermined linear system (the number of the equations is greater than the number of the unknowns). Assuming the angles are uniformly sampled with $\Delta\phi = \pi/[2(I-1)]$, the resultant I equations can be expressed as

$$\begin{aligned} F_i(q) &= q^2 - \frac{a_i}{b} = 0, i = 1, 2, \cdots, I \\ a_i &= \sin^2\left[\frac{\pi}{N_0}\cos(\phi_i)\right] + \sin^2\left[\frac{\pi}{N_0}\sin(\phi_i)\right] \\ b &= \sin^2\left(\frac{\pi}{N_0}\right) \end{aligned} \tag{3.23}$$

where $\phi_i = (i-1)\Delta\phi$. Notice that there is no exact solution for (3.23).

To solve (3.23), the square error is defined as [92]

$$\|F(q)\|^2 = \sum_{i=1}^{I} [F_i(q)]^2 = \sum_{i=1}^{I} \left(q^2 - \frac{a_i}{b}\right)^2 \tag{3.24}$$

The least squares approximation to the solution can be found by minimizing (3.24), which is equivalent to forcing the derivative of (3.24) with respect to q to zero. This can be expressed as

$$\frac{\partial\|F(q)\|^2}{\partial q} = \sum_{i=1}^{I} 4q\left(q^2 - \frac{a_i}{b}\right) = 4q\left(Iq^2 - \frac{1}{b}\sum_{i=1}^{I} a_i\right) = 0 \tag{3.25}$$

Solving (3.25), q is obtained by

$$q = \frac{1}{\sqrt{Ib}}\sqrt{\sum_{i=1}^{I} a_i} \tag{3.26}$$

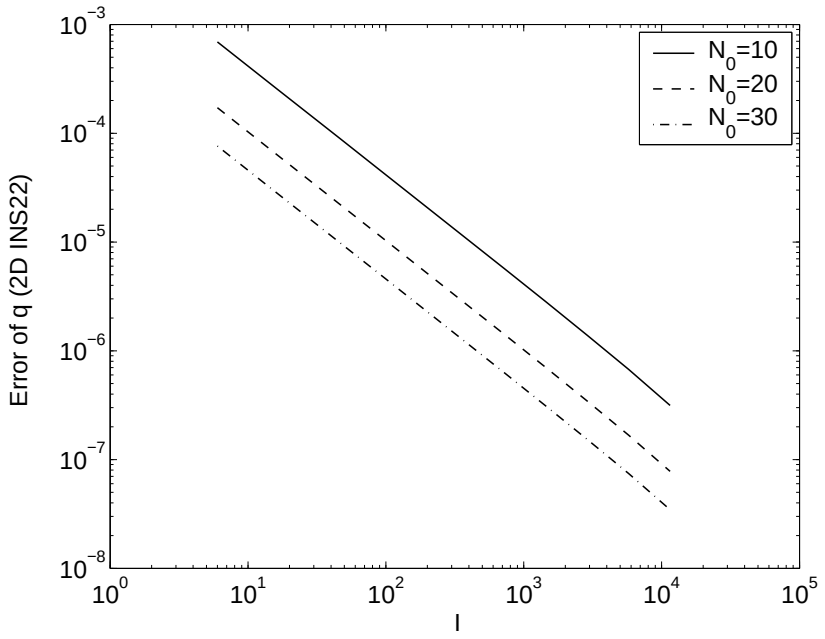

Fig. 3.11. Errors of q for the 2D INS22 scheme.

Notice that when $N = N_0$, the two terms containing S in the left-hand-side of (3.22) cancel out which makes q independent of Δt.

A remaining question is how many angles we need to calculate q? Using the q value with large I ($I = 90,001$) as a reference, the errors of q versus different I are plotted in Fig. 3.11. As shown, the error of q decreases as I or N_0 increases. For $N_0 = 10$, to achieve an error for q smaller than 10^{-5}, I must be larger than 400 ($I > 400$).

The local dispersion errors of the three (2,2) algorithms are plotted in Fig. 3.12. Only the curves between 0° and 90° are plotted because all the curves are 90° periodic. As shown, the average dispersion error of NS22 is smaller than that of Yee's algorithm. Also, the 2D NS22 scheme has zero dispersion along 0° and 90°. For the 2D INS22 scheme, the dispersion vanishes at 22.5° and 67.5° due to the symmetry. The effect of the free parameter q in the INS22 scheme is to shift the average error down to zero. However, the maximum phase

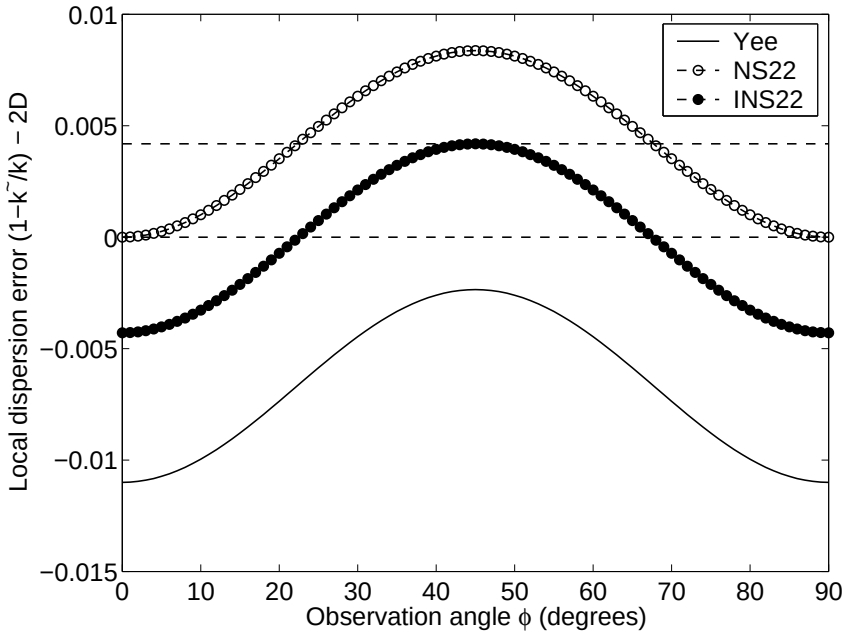

Fig. 3.12. Two-dimensional local dispersion errors of the (2,2) schemes [$S = 0.6, N = N_0 = 10, q(I = 401) = 1.00414816$].

errors (peak-to-peak) of the above three schemes are the same.

Similar to [1], [53]– [55], [60], forcing $\tilde{k} = k$ at $N = N_0$ along a zero dispersion angle (ϕ_0) in (3.22) leads to

$$q = \frac{\sqrt{\sin^2(\pi \cos \phi_0/N_0) + \sin^2(\pi \sin \phi_0/N_0)}}{\sin(\pi/N_0)} \tag{3.27}$$

The parameter q in (3.27) is Δt independent. In other words, q does not need to be re-calculated if the time step is changed. The reason we still use the least squares solution is that, for the 3D case, the zero dispersion angle is not obvious and may still have to be numerically calculated. Substituting $\phi_0 = 22.5^\circ$ into (3.27), the difference of q between the analytical solution (3.27) and the reference solution (3.26) with large I [$|q(analytical) - q(reference)|$] is plotted in Fig. 3.13. As shown, for practical mesh resolution, the reference solution obtained using the least squares method is a good approximation to the analytical

solution.

Now, let us re-examine the least squares solution of (3.26). Substituting a_i and b into (3.26) yields

$$q = \frac{1}{\sqrt{Ib}}\sqrt{\sum_{i=1}^{I} a_i} = \frac{\sqrt{\frac{1}{I}\sum_{i=1}^{I}\left[\sin^2(\pi\cos\phi_i/N_0)+\sin^2(\pi\sin\phi_i/N_0)\right]}}{\sin(\pi/N_0)} \tag{3.28}$$

which reveals the similarity between the least squares solution and the analytical solution of (3.27). As I approaches infinity, the term under the square root in (3.28) can be rewritten as

$$\lim_{I\to\infty}\frac{1}{I}\sum_{i=1}^{I} a(\phi_i) = \lim_{I\to\infty}\frac{2}{\pi}\sum_{i=1}^{I} a(\phi_i)\frac{\pi}{2I} = \frac{2}{\pi}\int_0^{\pi/2} a(\phi)d\phi \tag{3.29}$$

which is the average of $a(\phi)$ for $\phi \in [0, \pi/2]$. For a continuous function $a(\phi)$, using the integral mean value theorem, we obtain

$$\frac{2}{\pi}\int_0^{\pi/2} a(\phi)d\phi = \frac{2}{\pi}a(\phi_0)\int_0^{\pi/2} d\phi = a(\phi_0) \tag{3.30}$$

for a constant $\phi_0 \in [0, 2\pi]$, which agrees with the formulation in (3.27). This suggests that the zero dispersion angle ϕ_0 can be found by solving

$$a(\phi_0) = \frac{2}{\pi}\int_0^{\pi/2} a(\phi)d\phi \tag{3.31}$$

The integral in (3.31) still needs to be evaluated numerically.

Besides the local dispersion error defined in (3.9), the 2D global dispersion error is defined as

$$E_{glb}^{2D} = \int_0^{2\pi}\left|1-\frac{\tilde{k}}{k}\right| d\phi \tag{3.32}$$

In Fig. 3.14, we plot the global dispersion error when the design mesh resolution of NS22 and INS22 is set to 10. As shown, near the design mesh resolution, the INS22 scheme

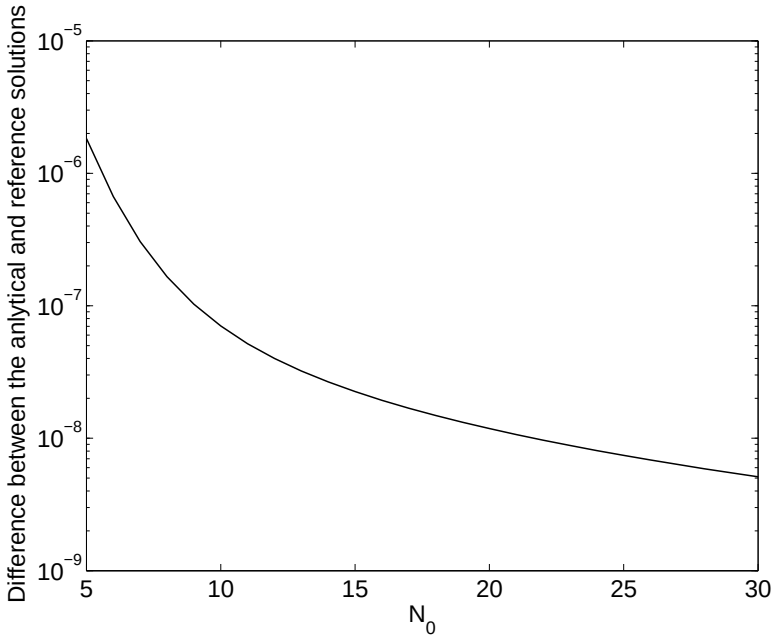

Fig. 3.13. Difference of q between the analytical and reference solutions.

exhibits an improved average dispersion distribution compared to the other two schemes. However, the low-dispersion performance of the NSFD methods is still relatively narrow band.

3.4.3. Dispersion Analysis for INS24

The optimal q values for the INS24 scheme can be derived following a very similar procedure summarized in the previous section. In this section, the 3D INS24 scheme will be considered as an example. The derivation starts with the dispersion relation of the 3D

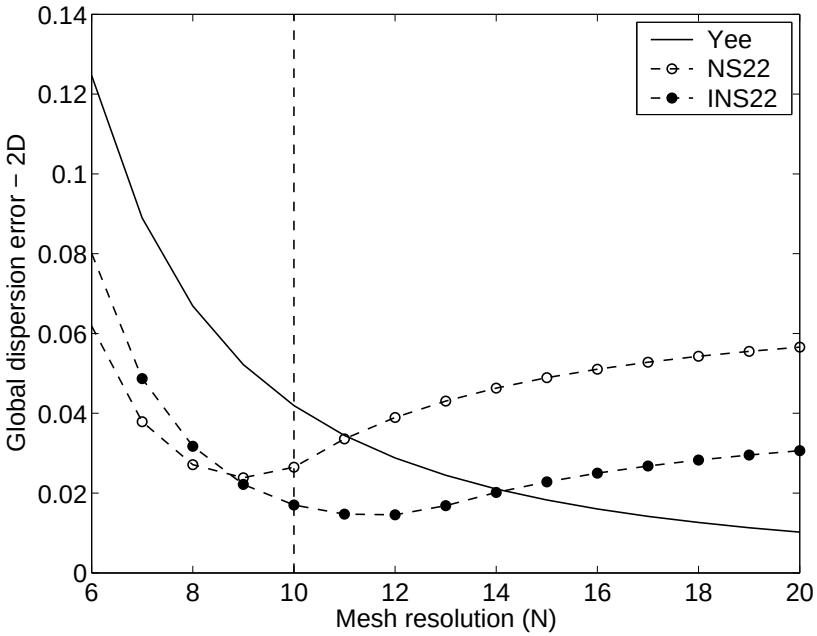

Fig. 3.14. Two-dimensional global dispersion errors of the (2,2) schemes ($S = 0.6, N_0 = 10, q = 1.00414816$).

INS24 scheme which can be written as

$$
\begin{aligned}
& \frac{[\frac{27}{24}\sin(\pi/N_0) - \frac{1}{24}\sin(3\pi/N_0)]^2}{\sin^2(\pi S/N_0)} \sin^2\left(\frac{\pi S}{N}\right) \\
= \quad & \frac{1}{q^2}\left\{\left[\frac{9}{8}\sin\left(\frac{\pi\cos\phi\sin\theta}{N}\frac{\tilde{k}}{k}\right) - \frac{1}{24}\sin\left(\frac{3\pi\cos\phi\sin\theta}{N}\frac{\tilde{k}}{k}\right)\right]^2\right. \\
+ \quad & \left[\frac{9}{8}\sin\left(\frac{\pi\sin\phi\sin\theta}{N}\frac{\tilde{k}}{k}\right) - \frac{1}{24}\sin\left(\frac{3\pi\sin\phi\sin\theta}{N}\frac{\tilde{k}}{k}\right)\right]^2 \\
+ \quad & \left.\left[\frac{9}{8}\sin\left(\frac{\pi\cos\theta}{N}\frac{\tilde{k}}{k}\right) - \frac{1}{24}\sin\left(\frac{3\pi\cos\theta}{N}\frac{\tilde{k}}{k}\right)\right]^2\right\} \qquad (3.33)
\end{aligned}
$$

Similar to the 2D case, forcing $\tilde{k} = k$ at $N = N_0$ at I angles along $\phi(0^\circ \sim 90^\circ)$ and J angles along $\theta(0^\circ \sim 90^\circ)$ (note that the dispersion error for the INS24 scheme is 90° periodic with respect to ϕ and θ) leads to an overdetermined linear system

$$F_p(q) = q^2 - \frac{a_p}{b} = 0, p = 1, 2, \cdots I \times J \qquad (3.34)$$

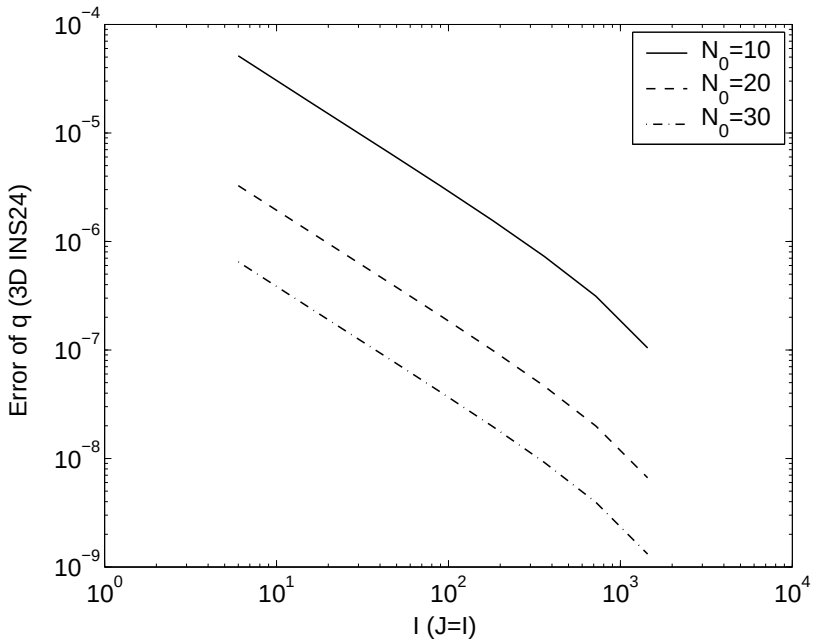

Fig. 3.15. Errors of q for the 3D INS24 scheme.

where

$$\begin{aligned} a_p &= \left[\frac{9}{8}\sin\left(\frac{\pi\cos\phi_i\sin\theta_j}{N_0}\right) - \frac{1}{24}\sin\left(\frac{3\pi\cos\phi_i\sin\theta_j}{N_0}\right)\right]^2 \\ &+ \left[\frac{9}{8}\sin\left(\frac{\pi\sin\phi_i\sin\theta_j}{N_0}\right) - \frac{1}{24}\sin\left(\frac{3\pi\sin\phi_i\sin\theta_j}{N_0}\right)\right]^2 \\ &+ \left[\frac{9}{8}\sin\left(\frac{\pi\cos\theta_j}{N_0}\right) - \frac{1}{24}\sin\left(\frac{3\pi\cos\theta_j}{N_0}\right)\right]^2 \\ i &= 1 \sim I, j = 1 \sim J \\ b &= \left[\frac{9}{8}\sin\left(\frac{\pi}{N_0}\right) - \frac{1}{24}\sin\left(\frac{3\pi}{N_0}\right)\right]^2 \end{aligned}$$

Then, the q value for the 3D INS24 can be solved following a similar procedure summarized in (3.24)-(3.26). The reference solution is found by using $I = J = 2,881$. The errors of q versus different I are plotted in Fig. 3.15. As shown, the error of q decreases when I or N_0 increases. Using $I = J > 400$, the error of q is smaller than 10^{-6} for $N_0 = 10$.

The correction parameter q can also be found by forcing $\tilde{k} = k$ at $N = N_0$ along zero

dispersion direction (ϕ_0, θ_0) of the INS24 scheme. This leads to

$$\begin{aligned} q &= \left\{ \left[\frac{9}{8} \sin\left(\frac{\pi \cos\phi_0 \sin\theta_0}{N_0} \right) - \frac{1}{24} \sin\left(\frac{3\pi \cos\phi_0 \sin\theta_0}{N_0} \right) \right]^2 \right. \\ &+ \left[\frac{9}{8} \sin\left(\frac{\pi \sin\phi_0 \sin\theta_0}{N_0} \right) - \frac{1}{24} \sin\left(\frac{3\pi \sin\phi_0 \sin\theta_0}{N_0} \right) \right]^2 \\ &+ \left. \left[\frac{9}{8} \sin\left(\frac{\pi \cos\theta_0}{N_0} \right) - \frac{1}{24} \sin\left(\frac{3\pi \cos\theta_0}{N_0} \right) \right]^2 \right\}^{1/2} \\ &\times \left[\frac{9}{8} \sin\left(\frac{\pi}{N_0} \right) - \frac{1}{24} \sin\left(\frac{3\pi}{N_0} \right) \right]^{-1} \end{aligned} \tag{3.35}$$

However, the exact values of ϕ_0 and θ_0 are not obvious. In fact, there are multiple solutions for the zero dispersion direction. For convenience, we only need to find ϕ_0 and θ_0 along the principal axes, for example, forcing $\theta_0 = 0^\circ$ in (3.35) and solving for ϕ_0, or *vice versa*. Assuming $\theta_0 = 0^\circ$ and substituting the reference q value with $I = J = 2,881$ into (3.35), ϕ_0 is solved and plotted in Fig. 3.16. As shown, ϕ_0 converges to 27.07° as I increases.

Using the definition in (3.9), the local dispersion errors of Fang's algorithm and the NS24, INS24 schemes for $N_0 = 10$ and $S = 0.49$ are plotted in Figs. 3.17 and 3.18; q is calculated using $I = J = 401$. Only the dispersion in the first octant is plotted due to the rotational symmetry of the curves. As shown, both NSFD schemes exhibit lower dispersion error than Fang's algorithm. The average error of the INS24 scheme is shifted down to zero compared to the NS24 scheme. The maximum phase differences (peak-to-peak) are the same for all three methods.

The three-dimensional global dispersion error can be defined as

$$E_{glb}^{3D} = \int_0^{2\pi} \int_0^{\pi} \left| 1 - \frac{\tilde{k}}{k} \right| \sin\theta d\theta d\phi \tag{3.36}$$

The global dispersion errors of Fang's, NS24, and INS24 are plotted in Fig. 3.19. Notice that the INS24 scheme exhibits the lowest average dispersion error near the design mesh

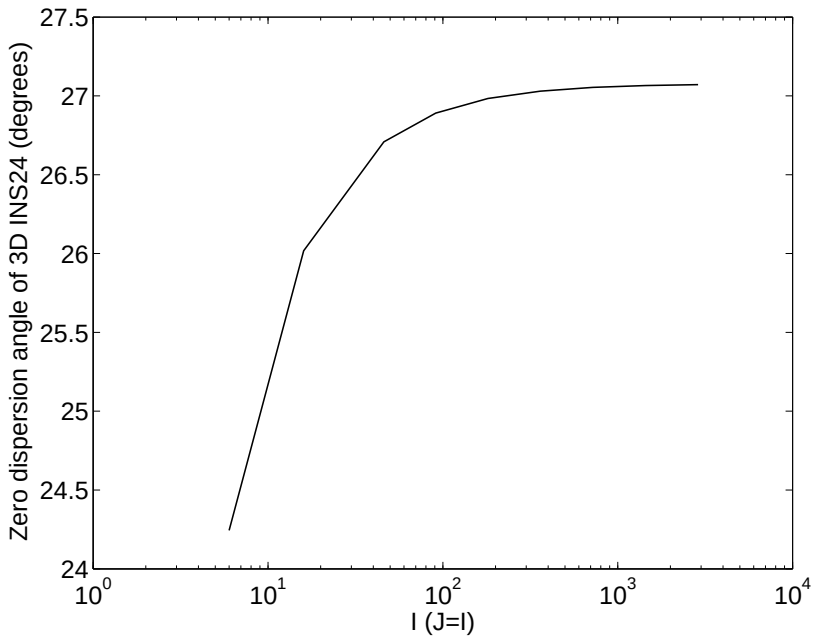

Fig. 3.16. Zero-dispersion angle for the 3D INS24 scheme ($\theta_0 = 0°, S = 0.49, N = N_0 = 10, q(I = J = 2,881) = 1.00034998$).

resolution. Moreover, both NSFD methods are relative narrow band.

3.4.4. Numerical Simulations

In this section, a variety of numerical simulations will be performed to justify the formulations of the improved nonstandard finite-difference. All the q values are computed using the least squares solution. All the open problems (radiation and scattering) are truncated with an 8-layer PML.

In the first simulation, a single-frequency TM^z polarized plane wave is normally incident upon a two-dimensional dielectric square cylinder. The cylinder has a side width of $d = 2\lambda_0$ (where λ_0 is the free-space wavelength) and a relative permittivity $\epsilon_r = 4$. An arithmetic average permittivity ($\epsilon_r = 2.5$) is assigned along the free-space-material interface. The sk and q values are different for different materials. For example, for $N_0 = 20$,

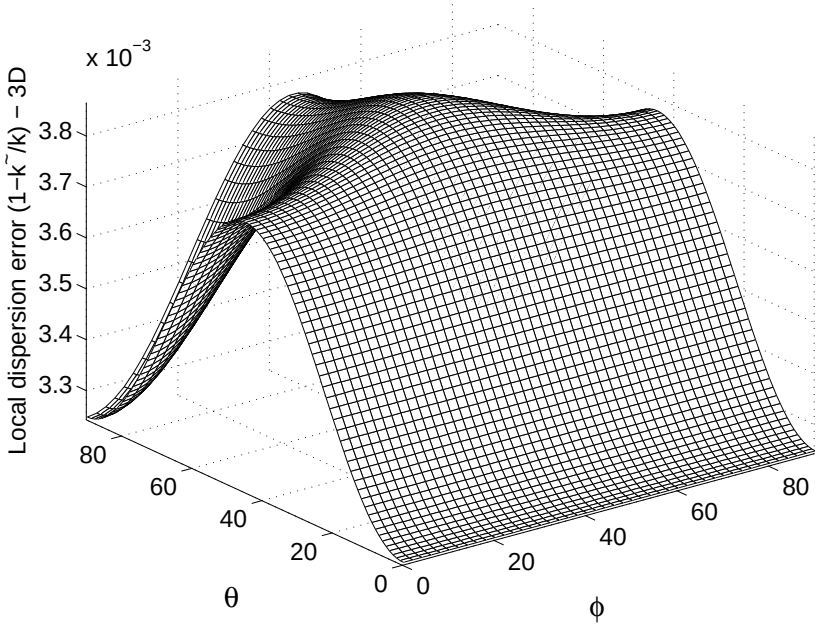

Fig. 3.17. Three-dimensional local dispersion error of Fang's algorithm ($S = 0.49, N = N_0 = 10$).

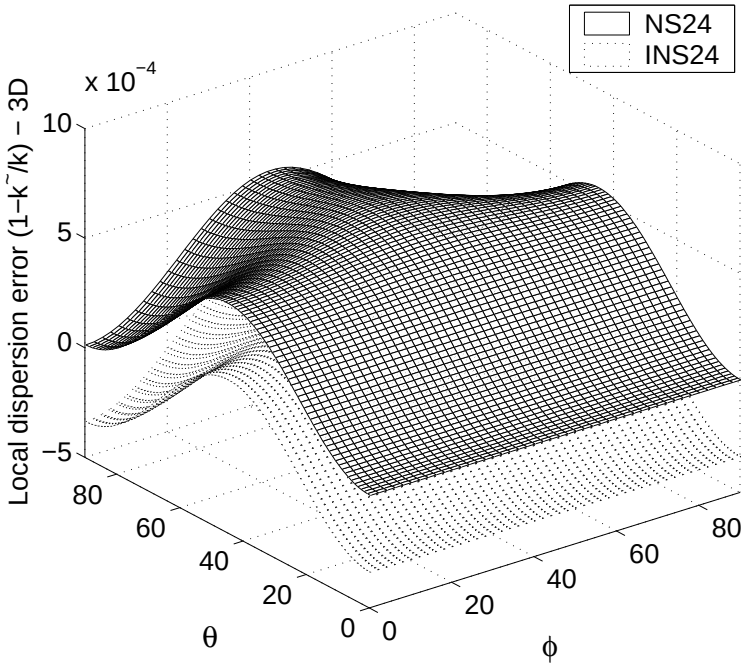

Fig. 3.18. Three-dimensional local dispersion error of the NS24 and INS24 schemes ($S = 0.49, N = N_0 = 10, q = 1.00034933$).

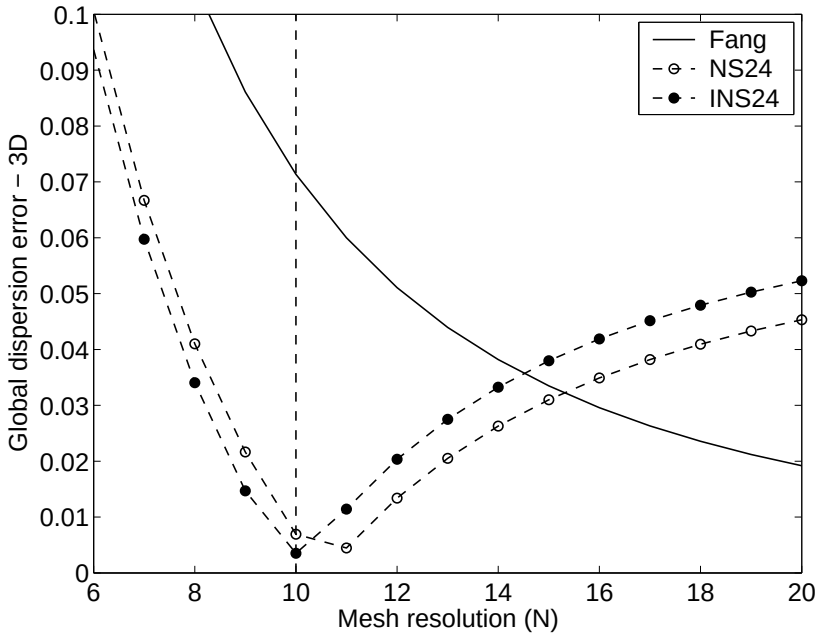

Fig. 3.19. Three-dimensional global dispersion error of the (2,4) schemes ($S = 0.49, N_0 = 10, N = 6 \sim 20, q = 1.00034933$).

it can be solved $q_1 = 1.00102838$, $q_2 = 1.00414816$, and $q_3 = 1.00258172$ for the mesh resolution in the free space, the dielectric material and the interface, respectively. The bistatic RCS using $N_0 = 20$ (in free space) is computed by Yee's, NS22, and INS22 schemes and is plotted in Fig. 3.21. The reference solution is provided by Yee's algorithm with $N_0 = 160$ (in free space).

A good agreement between all four solutions is visually indicated except for the angles close to 180°. To compare the performance of the three algorithms, the following L_2 error is defined and used.

$$L_2 = \sqrt{\frac{\sum_{i=1}^{M}(A_i^{sim} - A_i^{ref})^2}{M}} \tag{3.37}$$

where A^{sim} and A^{ref} are the simulated and the reference amplitudes of the linearized RCS, respectively; M represents the number of the observation angles. The L_2 errors of the three

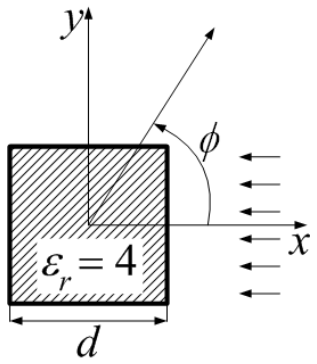

Fig. 3.20. Geometry of the dielectric square cylinder ($d = 2\lambda_0$).

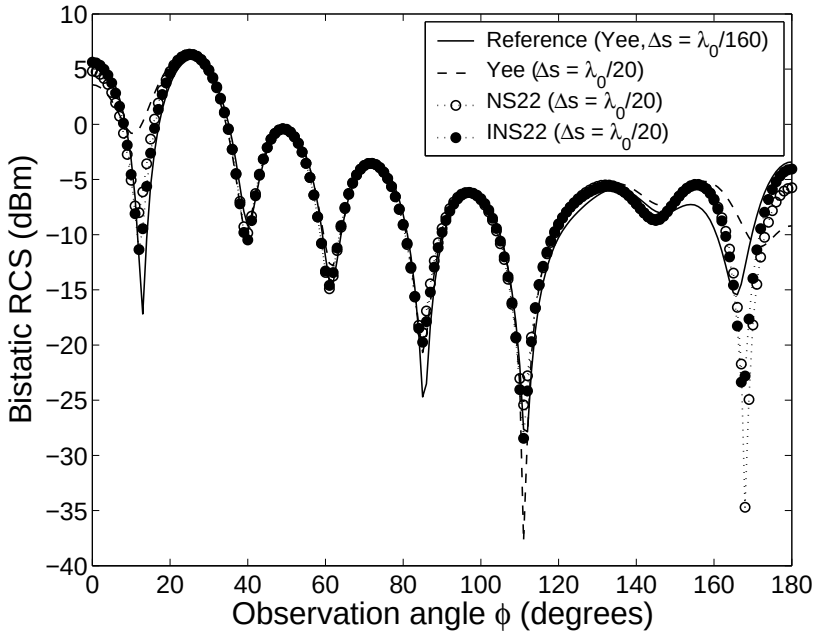

Fig. 3.21. Bistatic RCS of a two-dimensional dielectric square cylinder ($S = 0.6, N_0 = 20$ in free space, $M = 361$).

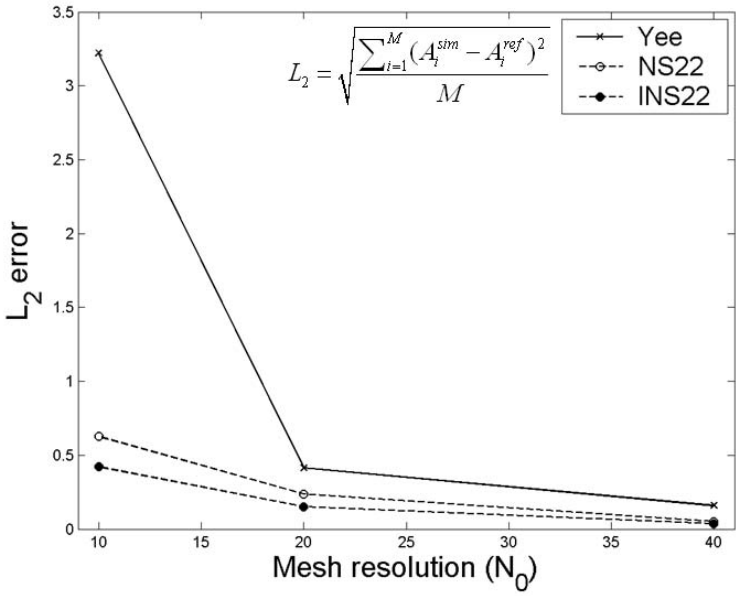

Fig. 3.22. The L_2 error of the linearized RCS of the dielectric square cylinder versus the free-space mesh resolution ($M = 361$).

algorithms using different design mesh resolutions ($N_0 = 10, 20$, and 40 in free space) are plotted in Fig. 3.22. As shown, the INS22 scheme has the lowest L_2 error. However, as the design mesh resolution increases, the performance of the INS22 approaches that of the NS22.

For the second simulation, a TE^x polarized plane-wave is incident and scattered by a three-dimensional PEC square plate [2]. The plate has a side width $d = 5\lambda_0$. The design mesh resolution is selected to be $N_0 = 6$. The reference solution is predicted by Yee's algorithm with $N_0 = 40$; q is calculated to be 1.01556617. The yz-plane bistatic RCS of the plate for incident angles $\theta_i = 0^\circ$ and $\theta_i = 30^\circ$ is computed by Yee's, NS22, and INS22 schemes and plotted in Figs. 3.24 and 3.25.

A good agreement between all four solutions is indicated visually. The L_2 errors

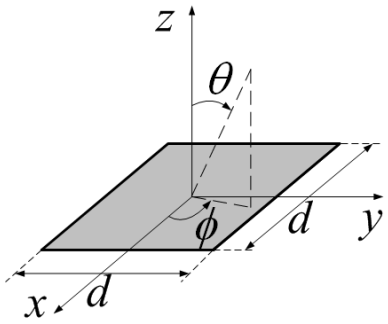

Fig. 3.23. Geometry of the PEC square plate ($d = 5\lambda_0$).

Table 3.2. L^2 Error ($S = 0.55, \Delta s = \lambda_0/6, M = 361$)

Scheme	L_2 Error ($\theta_i = 0°$)	L_2 Error ($\theta_i = 30°$)
Yee	24.6727	14.6364
NS22	23.3063	10.5742
INS22	24.1345	6.0993

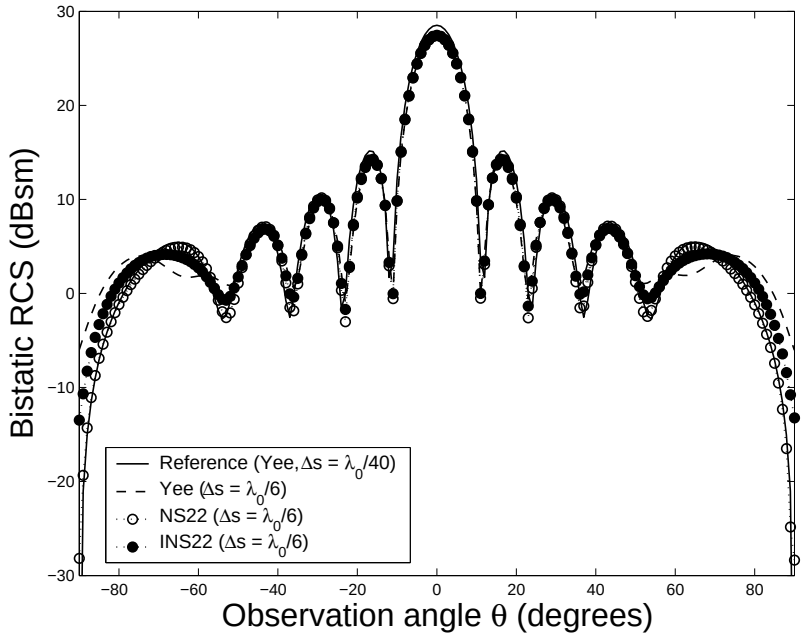

Fig. 3.24. Bistatic RCS of the three-dimensional PEC square plate (yz-plane, $\theta_i = 0°, N_0 = 6, S = 0.55, M = 361$).

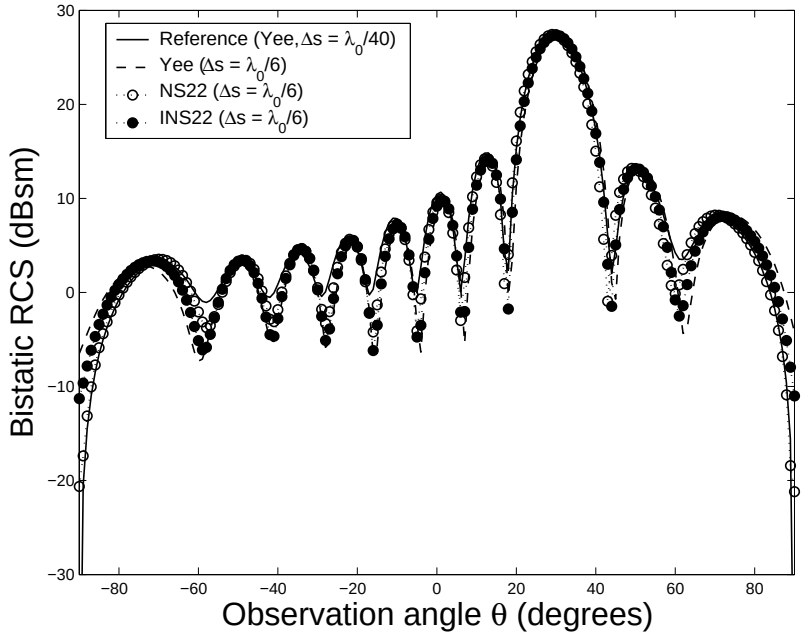

Fig. 3.25. Bistatic RCS of the three-dimensional PEC square plate (yz-plane, $\theta_i = 30°, N_0 = 6, S = 0.55, M = 361$).

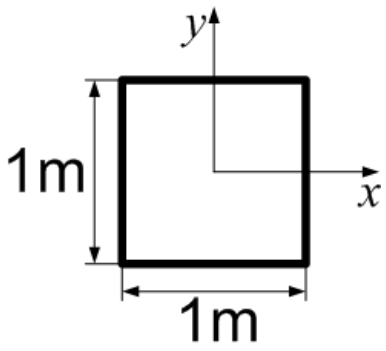

Fig. 3.26. Geometry of the PEC square cavity.

calculated using 3.37 are summarized in Table 3.2. For $\theta_i = 0°$ case, the NS22 scheme has the lowest error because the major energy in the scattering pattern is along $\theta = 0°$ where NS22, according to Fig. 3.12, has the lowest dispersion. However, for the $\theta_i = 30°$ case, the INS22 scheme has the lowest error since the major energy of the pattern is directed along the specular angle of $\theta = 30°$ where the INS22, according to Fig. 3.12, has the lowest dispersion error.

The first example using the higher-order (2,4) schemes simulates the mode field structures and resonant frequencies of a two-dimensional PEC square cavity (TE^z). The cavity has a side width $d = 1$ m. Fang's, NS24 and INS24 schemes with $\Delta s = 1$ m are used for comparison. For the extended stencil, image theory is used to model the PEC boundaries of the cavity [61]. The cavity is excited by a Gaussian pulse with significant energy within 0-0.5GHz. After updating 96,000 time steps, the time history of the H_z field at an observation point is Fourier transformed to the frequency domain. The absolute errors of the resonant frequencies are plotted in Figs. 3.27 and 3.28.

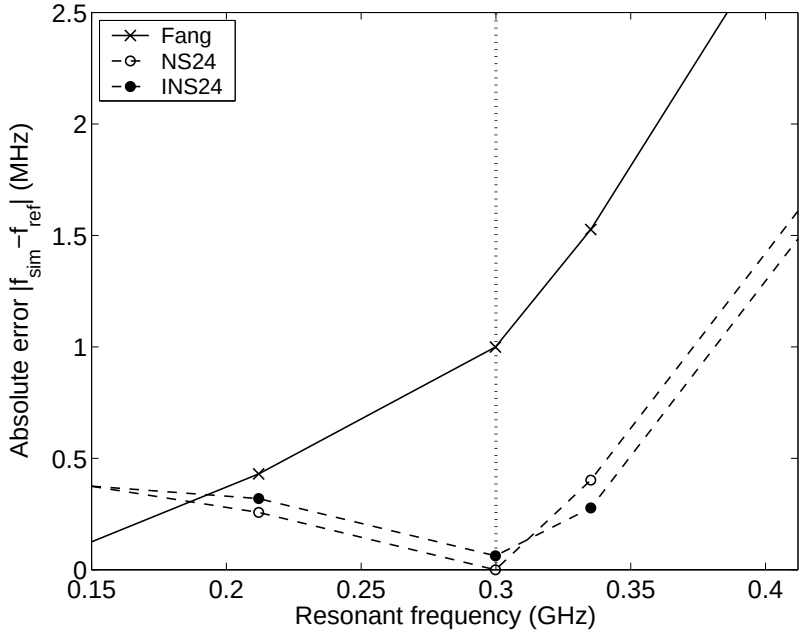

Fig. 3.27. Absolute error of the resonant frequencies of the two-dimensional PEC square cavity ($\Delta s = 0.1$ m, $S = 0.5$, $f_0 = 0.3$ GHz).

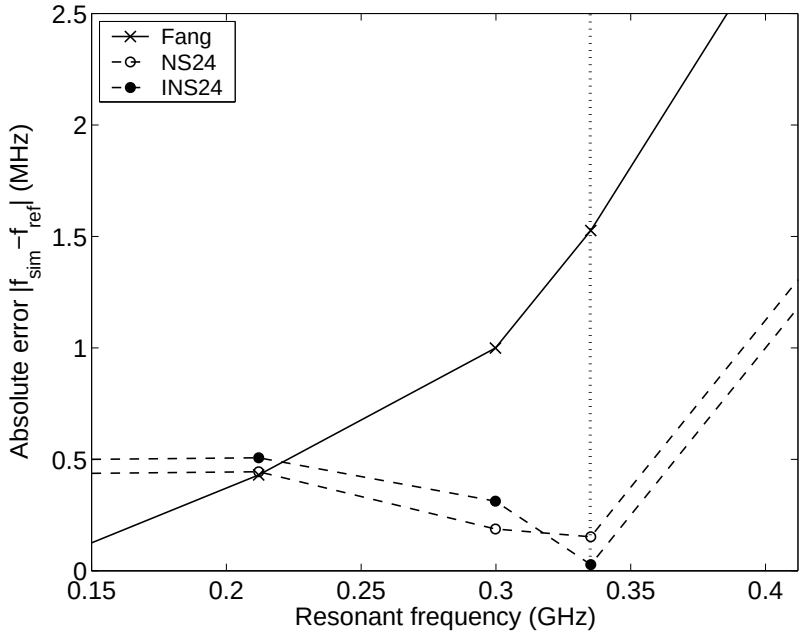

Fig. 3.28. Absolute error of the resonant frequencies of the two-dimensional PEC square cavity ($\Delta s = 0.1$ m, $S = 0.5$, $f_0 = 0.335$ GHz).

In Fig. 3.27, the design frequency is set to be 0.3GHz which is the resonant frequency of the TE_{20} mode; q for this case is solved to be 1.00026584. As shown, the NS24 scheme predicts nearly the exact solution. The error of the INS24 scheme is higher than that of the NS24 scheme, but still much lower than that of Fang's algorithm. The explanation is that, for the TE_{20} mode, the wave vector is directed along the x axis where, according to Fig. 3.18, the NS24 scheme has no dispersion and the INS24 scheme has medium dispersion error compared to Fang's and NS24 algorithms. In Fig. 3.28, the design frequency is set to be 0.335GHz which is the resonant frequency of the TE_{21} mode; q is determined to be 1.00041064. In this case the INS24 scheme has the lowest error because the wave vector is directed along 26.6° where, according to Fig. Fig. 3.18, the INS24 scheme has the lowest dispersion error.

The last simulation is a two-dimensional four-element array. The geometry of the array is shown in Fig. 3.29. The array is excited by four single-frequency soft sources (E_z) which are uniform in amplitude and in phase. Fang's, NS24 and INS24 algorithms with $N_0 = 6$ are used to compute the array factor. Using (3.26), q is found to be 1.00196039. In Fig. 3.30, the array factor power patterns versus observation angles are plotted (note the 90° pattern is periodic). The errors calculated using (3.37) are summarized in Table 3.3. It is evident that, the INS24 produces the most accurate result based on the observation of the pattern or the comparison of the L_2 error.

Table 3.3. L^2 Error ($S = 0.5, \Delta s = \lambda_0/6, M = 361$)

Scheme	L^2 Error
Fang	0.07786753
NS24	0.03835138
INS24	0.02539144

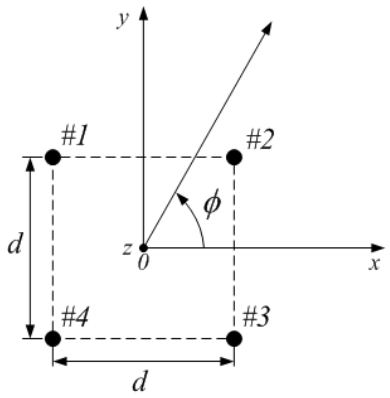

Fig. 3.29. Geometry of the four-element array ($d = 5.5\lambda_0$).

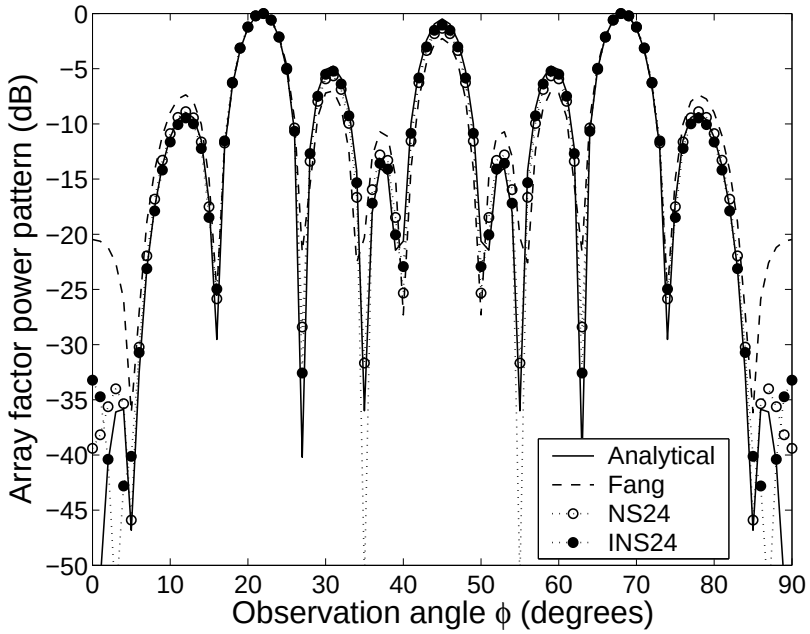

Fig. 3.30. The xy-plane array factor power pattern of the four-element array ($\Delta s = \lambda_0/6$,$S = 0.5, M = 361$).

In this section, we present an improved NSFD algorithm by introducing an extra degree of freedom into the frequency-optimized space step of the regular NSFD. The INS22 algorithm exhibits lower dispersion error than the regular NS22 and Yee's algorithms near the design mesh resolution. However, this low-dispersion performance is narrow band. The correction parameter q of INS22 is independent of the time-step which avoids the recalculation when the time step changes. The computation of the parameters for the regular NSFD, $sk_{\xi 0}$ and $s\omega_0$, is simple. To apply the INS22 algorithm, only slight modifications are needed to Yee's algorithm. The increases of the CPU time and memory consumption are very minimal. The INS24 scheme shares the above properties of the INS22 scheme.

Clearly, the INS schemes mitigate the average dispersion error for the multi-dimensional simulations. However, the INS schemes may not be suitable to simulate broad-band signals since the low-dispersion areas are limited in the vicinity of the the design frequency.

3.5. The Generalized NSFD Schemes

To resolve some of the previously stated issues, the concept of the INS schemes can be generalized by introducing more degrees of freedom into the space stencils. In the rest of the report, these schemes are referred to as *Generalized NSFD (GNS) schemes* [93]. The GNS24 scheme will be used as an example to demonstrate the analytical procedure.

3.5.1. The GNS24 Scheme

It has been reported that the dispersion error of Fang's FDTD(2,4) algorithm can be drastically reduced by properly adjusting the coefficients of the space stencil [58] - [65].

However, in the aforementioned literature, the procedure to determine the optimal coefficients becomes cumbersome for complex stencils. A more straightforward approach is to use the least squares method introduced in the previous sections. Now the GNS24 scheme will be presented by considering a 2D domain with the square mesh ($\Delta x = \Delta y = \Delta s$). The extension to three dimension is straightforward.

As stated in Chapter 2, the fourth-order of accuracy will not be achieved for the entire FDTD(2,4) algorithm due to the second-order error in the time domain. Thus, for this case, a space stencil with fourth-order accuracy may not be necessary. In other words, a space stencil with second-order accuracy is sufficient. This allows additional degrees of freedom in choosing the coefficients of the space stencil.

In the 2D Cartesian coordinate, the space stencils for the GNS24 scheme can be expressed as [60]

$$d_\xi(f_\xi) = \frac{C_1(f_{\xi+1/2} - f_{\xi-1/2}) + C_2(f_{\xi+3/2} - f_{\xi-3/2})}{\Delta s}, \xi = x, y \tag{3.38}$$

where C_1 and C_2 are free parameters whose values will be determined based upon the dispersion analysis. If $C_1 = 9/8$ and $C_2 = -1/24$, (3.38) reduces to the regular fourth-order stencil.

From Taylor series expansion, it can be shown that the constraint for C_1 and C_2 to guarantee second-order accuracy is [60], [93]

$$C_1 + 3C_2 = 1 \quad \text{or} \quad C_1 = 1 - 3C_2 \tag{3.39}$$

This condition allows one independent free parameter which can be utilized to reduce the numerical dispersion. A more relaxed constraint would be [93]

$$C_1 + 3C_2 = p \quad \text{or} \quad C_1 = p - 3C_2 \tag{3.40}$$

where p is an extra free parameter. This condition makes the stencil in (3.38) nearly second-order accurate (it can be verified that p is very close to unity) but provides two independent free parameters to further reduce the dispersion. For convenience, the schemes governed by (3.39) and (3.40) are referred to as the GNS24-1 and GNS24-2 schemes, respectively. The values of the free parameters C_1 and C_2 can be determined following a similar procedure demonstrated in Section 3.4.3.

First, the dispersion relation of the GNS24 schemes can be derived and written as

$$\begin{aligned} \frac{1}{S^2}\sin^2\left(\frac{\pi S}{N}\right) &= \left[C_1 \sin\left(\frac{\pi\cos\phi}{N}\frac{\tilde{k}}{k}\right) + C_2 \sin\left(\frac{3\pi\cos\phi}{N}\frac{\tilde{k}}{k}\right)\right]^2 \\ &+ \left[C_1 \sin\left(\frac{\pi\sin\phi}{N}\frac{\tilde{k}}{k}\right) + C_2 \sin\left(\frac{3\pi\sin\phi}{N}\frac{\tilde{k}}{k}\right)\right]^2 \end{aligned} \tag{3.41}$$

where S is the Courant number, N is the number of cells per wavelength, and $\tilde{k}/k$ is the ratio of the numerical wave number to the exact wave number. Since (3.39) is a special case of (3.40), we only present (3.40) as an example.

Second, forcing $\tilde{k}/k = 1$ at $N = N_0$ along $\phi_i = 0^\circ \sim 90^\circ, i = 1 \sim I$ in (3.41) leads to an overdetermined nonlinear system which can be expressed as

$$F_i(C_1, C_2) = (a_i C_1 + b_i C_2)^2 + (c_i C_1 + d_i C_2)^2 - e = 0, i = 1, 2, \cdots, I \tag{3.42}$$

where

$$\begin{aligned} a_i &= \sin\left(\frac{\pi\cos\phi_i}{N_0}\right),\ b_i = \sin\left(\frac{3\pi\cos\phi_i}{N_0}\right) \\ c_i &= \sin\left(\frac{\pi\sin\phi_i}{N_0}\right),\ d_i = \sin\left(\frac{3\pi\sin\phi_i}{N_0}\right) \\ e &= \frac{1}{S^2}\sin^2\left(\frac{\pi S}{N_0}\right) \end{aligned}$$

Equation (3.42) can be rewritten as

$$F_i(C_1, C_2) = f_i C_1^2 + g_i C^2 + h_i C_1 C_2 - e = 0, i = 1, 2, \cdots, I \tag{3.43}$$

where

$$\begin{aligned} f_i &= a_i^2 + c_i^2 \\ g_i &= b_i^2 + d_i^2 \\ h_i &= 2(a_i b_i + c_i d_i) \end{aligned}$$

The least squares solution can be found by minimizing the square error defined as follows [92]

$$\|F(q)\|^2 = \sum_{i=1}^{I} [F_i(q)]^2 = \sum_{i=1}^{I} \left(f_i C_1^2 + g_i C_2^2 + h_i C_1 C_2 - e \right)^2 \tag{3.44}$$

This can be achieved by solving the following equations

$$\mathbf{G}(C_1, C_2) = \begin{bmatrix} G_1(C_1, C_2) \\ \\ G_2(C_1, C_2) \end{bmatrix} = \begin{bmatrix} \frac{\partial \|F(q)\|^2}{\partial C_1} \\ \\ \frac{\partial \|F(q)\|^2}{\partial C_2} \end{bmatrix} = 0 \tag{3.45}$$

Since (3.45) is still a nonlinear equation, Newton's method will be used to solve for C_1 and C_2. Assuming $\mathbf{C} = [C_1, C_2]'$ and $\mathbf{J}$ is the Jacobian of $\mathbf{G}$, the procedure is summarized as follows

$$\mathbf{C}^{n+1} = \mathbf{C}^n + \mathbf{\Delta C}^n \tag{3.46}$$

where

$$\mathbf{\Delta C}^n = -\mathbf{J}^{-1}\mathbf{G}^n \tag{3.47}$$

In (3.47), $\mathbf{J}$ can be expressed in explicit form as

$$\mathbf{J} = \begin{bmatrix} \frac{\partial G_1}{\partial C_1} & \frac{\partial G_1}{\partial C_2} \\ \\ \frac{\partial G_2}{\partial C_1} & \frac{\partial G_2}{\partial C_2} \end{bmatrix} = \begin{bmatrix} \frac{\partial^2 \|F(q)\|^2}{\partial {C_1}^2} & \frac{\partial^2 \|F(q)\|^2}{\partial C_1 C_2} \\ \\ \frac{\partial^2 \|F(q)\|^2}{\partial C_1 C_2} & \frac{\partial^2 \|F(q)\|^2}{\partial {C_2}^2} \end{bmatrix}$$

where

$$\begin{aligned}
\frac{\partial^2 \|F(q)\|^2}{\partial {C_1}^2} &= 2\sum_{i=1}^{I}\left[\left(\frac{\partial F_i}{\partial C_1}\right)^2 + F_i\frac{\partial^2 F_i}{\partial {C_1}^2}\right] \\
\frac{\partial^2 \|F(q)\|^2}{\partial C_1 \partial C_2} &= 2\sum_{i=1}^{I}\left[\frac{\partial F_i}{\partial C_1}\frac{\partial F_i}{\partial C_2} + F_i\frac{\partial^2 F_i}{\partial C_1 C_2}\right] \\
\frac{\partial^2 \|F(q)\|^2}{\partial {C_2}^2} &= 2\sum_{i=1}^{I}\left[\left(\frac{\partial F_i}{\partial C_2}\right)^2 + F_i\frac{\partial^2 F_i}{\partial {C_2}^2}\right]
\end{aligned}$$

Notice that a good set of initial values for the iteration is $\mathbf{C}_0 = [9/8, -1/24]'$, i.e., the coefficients of the regular fourth-order stencil. The coefficients for the GNS24-1 scheme can be solved similarly.

Using the coefficients with large I ($I = 90,001$) as reference, the error of the coefficients for the GNS24-1 and GNS24-2 schemes are plotted in Figs. 3.31 and 3.32, respectively. To guarantee the errors to be smaller than 10^{-5}, $I = 401$ will be used to calculate the coefficients.

As an example, the coefficients for $N_0 = 10$ and $N_0 = 20$ are computed and summarized in Table 3.4.

Table 3.4. Computed coefficients for the GNS24 schemes ($S = 0.5$)

	$N_0 = 10$	$N_0 = 20$
GNS24-1	$C_1 = \ 1.08867882$ $C_2 = -0.02955961$	$C_1 = 1.08630375$ $C_2 = -0.02876792$
GNS24-2	$C_1 = \ 1.12864752$ $C_2 = -0.04437762$	$C_1 = \ 1.12592203$ $C_2 = -0.04232427$

Using these coefficients, the local dispersion error defined in (3.9) for each of the GNS24-1 and GNS24-2 schemes is plotted in Fig. 3.33. As shown, the GNS24-1 scheme exhibits lower

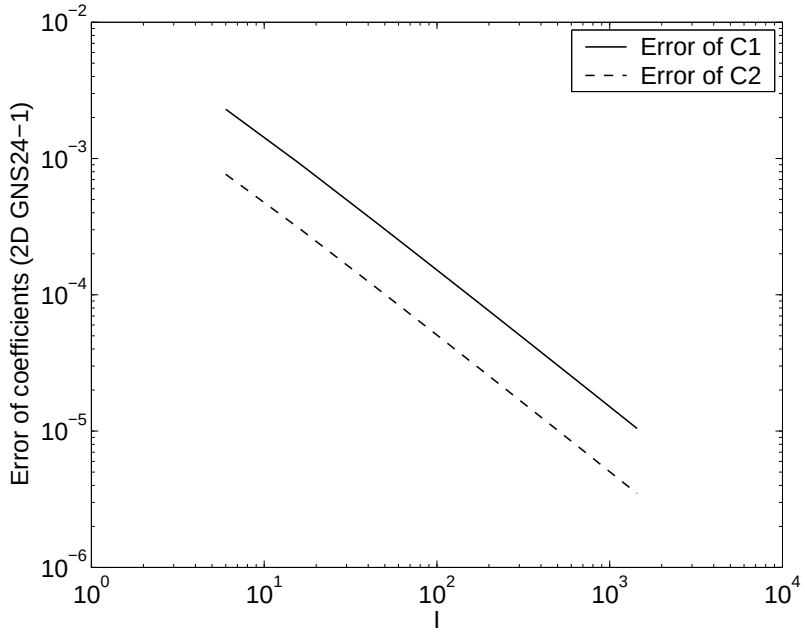

Fig. 3.31. Errors of the coefficients for the 2D GNS24-1 scheme $[S = 0.5, N_0 = 10, C_1(I = 90,001) = 1.08867882, C_2(I = 90,001) = -0.02955961]$.

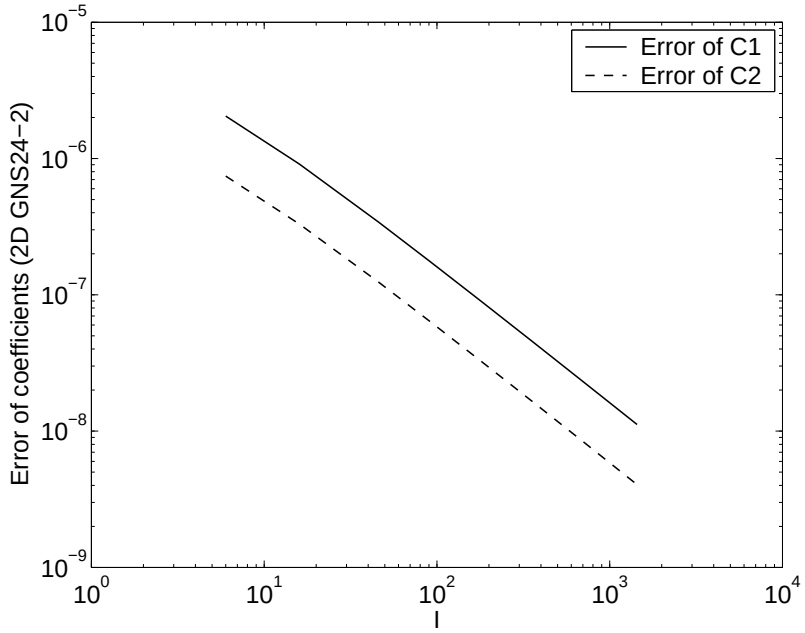

Fig. 3.32. Errors of the coefficients for the 2D GNS24-2 scheme $[S = 0.5, N_0 = 10, C_1(I = 90,001) = 1.12864752, C_2(I = 90,001) = -0.04437762]$.

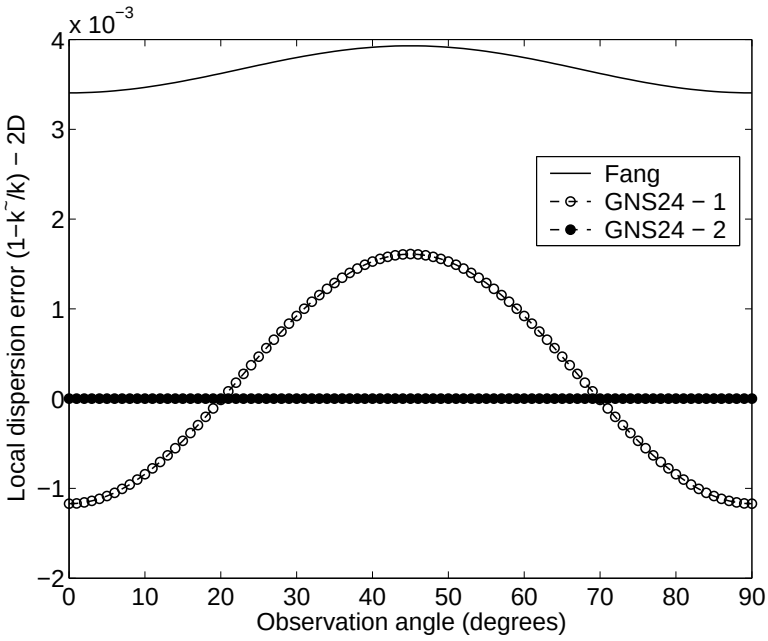

Fig. 3.33. Local dispersion error of the GNS24 schemes ($N = N_0 = 10, S = 0.5$).

average dispersion error than the FDTD(2,4) scheme, while the maximum phase error (peak-to-peak) is greater. However, the GNS24-2 scheme presents no visible dispersion errors.

The global dispersion errors defined in (3.32), for $N_0 = 10$ and $N_0 = 20$, are plotted in Figs. 3.34 and 3.35, respectively. It is evident that the GNS24-1 scheme generates smaller global errors for all the mesh resolutions. In other words, the GNS24-2 is a *broad-band* scheme in terms of dispersion error. However, compared to the INS24 scheme, the GNS24-2 scheme is a *narrow-band* scheme whose dispersion error is negligible at $N = N_0$. The dispersion-error null of the GNS24-2 scheme is precisely controlled by the design mesh resolution N_0.

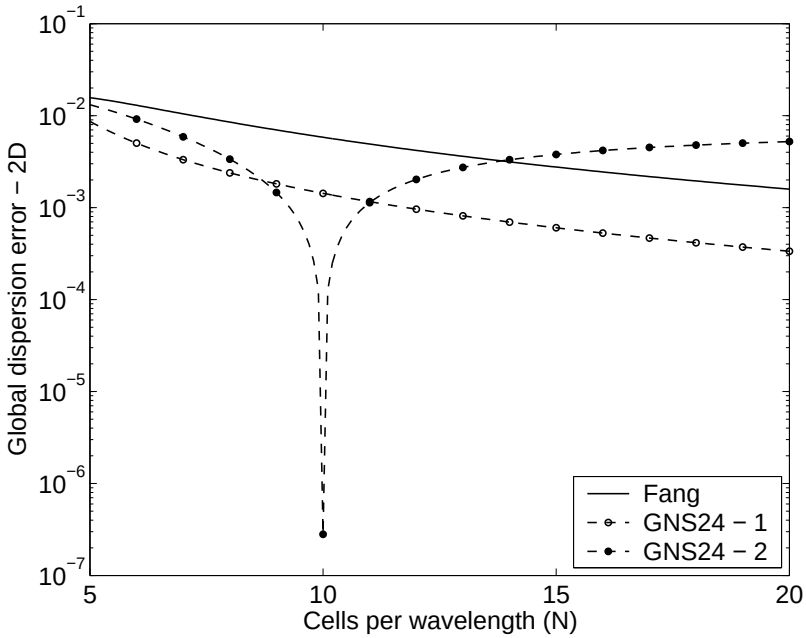

Fig. 3.34. Local dispersion error of the GNS24 schemes ($N_0 = 10, S = 0.5$).

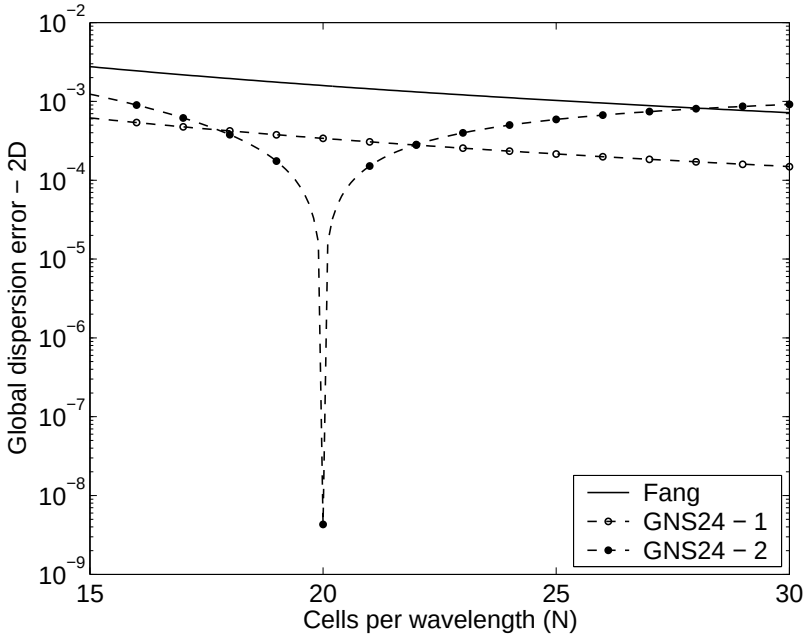

Fig. 3.35. Local dispersion error of the GNS24 schemes ($N_0 = 20, S = 0.5$).

3.5.2. Absorbing Boundary Condition

To perform the simulations in an open region, appropriate absorbing boundary conditions (ABCs) must be applied to truncate the FDTD domain. One of the most popular ABCs is the Perfectly Matched Layer (PML) proposed by Berenger [8] - [9]. In this section, the effectiveness of Berenger's PML for the GNS24 scheme will be verified following a procedure presented in [94], [95].

A two-dimensional TE^z FDTD test domain Ω_T is truncated by Berenger's PML with various number of layers. A uniform square mesh with $\Delta x = \Delta y = 0.015m$ is used. There are 100 cells in the x direction, and 50 cells in the y direction. The Courant number is set to $S = 0.5$. A benchmark domain Ω_B, with the same constitutive parameters, is used to simulate the wave propagating in an unbounded space. The benchmark domain is large enough so that there is no significant reflection from the boundary during the time of interest. The test and benchmark domains are shown in Fig. 3.36.

To excite the test and the benchmark domains, a hard-line source on H_z component is placed at the center of the test and benchmark domains. The source should have a very smooth transition to zero in the time domain. A waveform that satisfies this characteristic was suggested by [94] and repeated here as follows

$$H_z(\text{at center of domain}) = \begin{cases} \alpha[10 - 15cos(\omega_1\xi) + 6cos(\omega_2\xi) - cos(\omega_3\xi)] & \xi \leq \tau \\ \\ 0 & \xi > \tau \end{cases} \tag{3.48}$$

where

$$\alpha = \frac{1}{320}, \quad \tau = 10^{-9}, \quad \xi = n\Delta t, \quad \omega_m = \frac{2\pi m}{\tau}, \quad m = 1, 2, 3$$

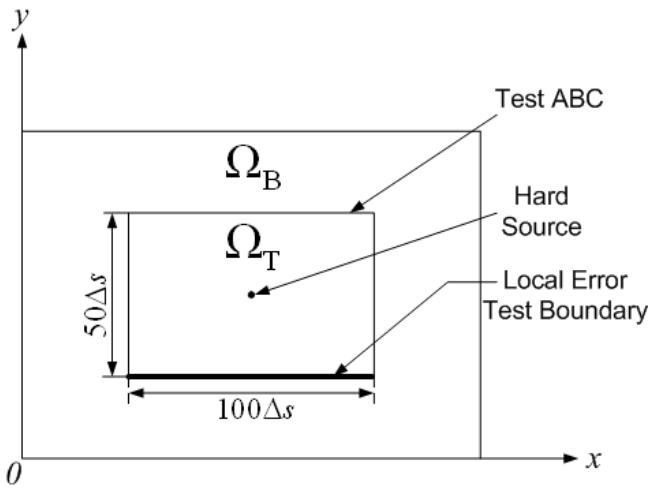

Fig. 3.36. The two-dimensional test and benchmark domains.

The time history and the frequency spectrum of the source in (3.48) are plotted in Figs. 3.37 and 3.38, respectively.

The errors caused by the tested ABCs are obtained by subtracting the field at the observation point within Ω_T from the field at the corresponding point in Ω_B. The local error is defined as

$$E_{loc} = \frac{|H_z^T(i,j) - H_z^B(i,j)|}{H_{zmax}} \tag{3.49}$$

where H_{zmax} is the maximum magnitude of the H_z components at the center of the lower air-PML interface and $H_z^T(i,j)$,$H_z^B(i,j)$ are magnetic fields in the test and benchmark domains, respectively. The observation points are selected along the lower air-PML interface, as

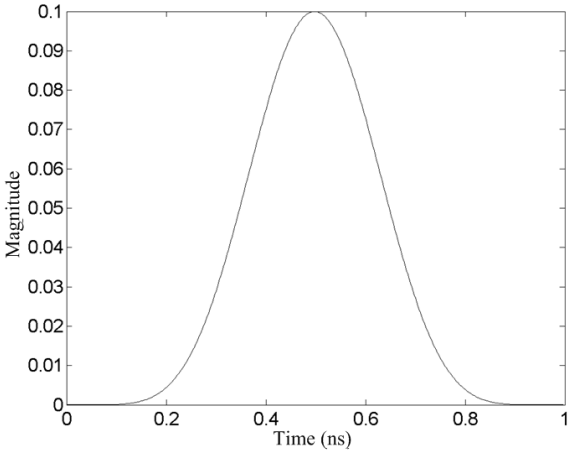

Fig. 3.37. The time history of the smooth pulse.

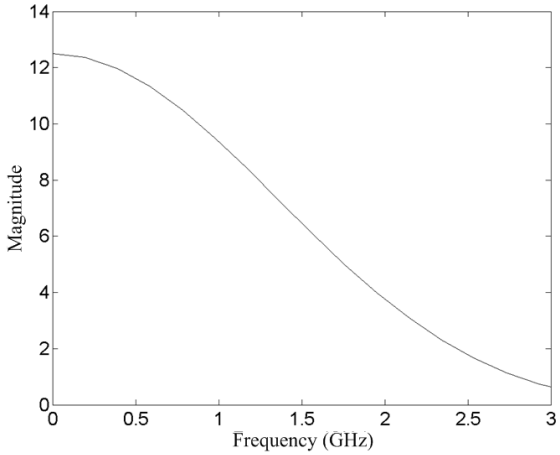

Fig. 3.38. The frequency spectrum of the smooth pulse.

shown in Fig. 3.36. The global error is defined by

$$E_{glb} = \sum_i \sum_j [H_z^T(i,j) - H_z^B(i,j)]^2 \tag{3.50}$$

As a reference, the local errors of Yee's algorithm with 4, 8, and 16 PML layers at $t = 100\Delta t$ are plotted in Fig. 3.39. For $N_0 = 20$ (at 1 GHz), the coefficients of the GNS24-2 scheme are computed to be $C_1 = 1.12592203$ and $C_2 = -0.04232427$. The local errors for Fang's and the GNS24-2 schemes are plotted in Fig. 3.40. As shown, the local errors generated by Fang's and the GNS24-2 scheme are about the same level as that of Yee's algorithm. The local error of the GNS24-2 scheme is slightly greater than that of Fang's algorithm.

The global errors versus time for Yee's algorithm are plotted in Fig. 3.41. The global errors for Fang's and the GNS24-2 schemes are plotted in Fig. 3.42. As shown, the global errors for all three methods with 4 or 8 PML layers are about the same level. However, for 16 PML layers, the global error of Yee's algorithm at a later time is much smaller than that generated by Fang's algorithm and the GNS24-2 scheme. This probably can be attributed to the larger error at the air-PML interface, which forms a higher noise floor for the two schemes using the extended stencils.

From the above numerical experiments, the Berenger's PML is able to effectively absorb the outgoing waves simulated by Fang's and the GNS24 schemes. For all the simulations presented in this report, no instability was observed.

3.5.3. Numerical Simulations

Two numerical simulations, the 2D PEC square and the four-element array, will be repeated for the GNS24 schemes. The geometry and the parameters used in the simulation

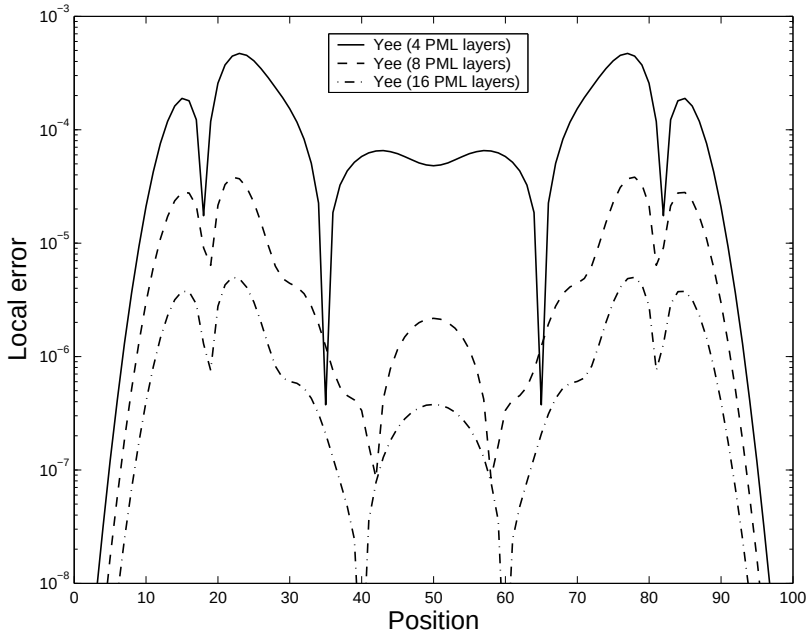

Fig. 3.39. The local error of Yee's algorithm ($\Delta s = 0.015m, S = 0.5$).

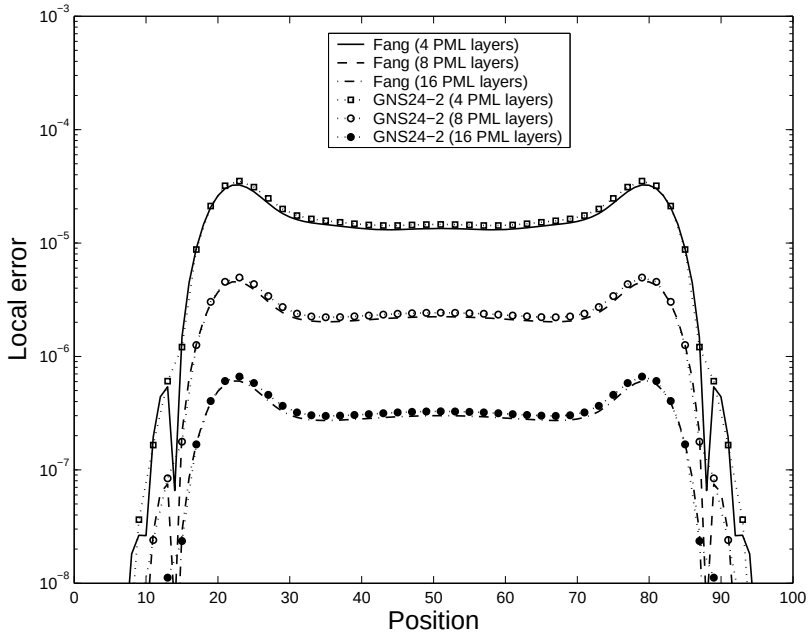

Fig. 3.40. The local errors of Fang's algorithm and the GNS24-2 scheme ($\Delta s = 0.015m, S = 0.5$).

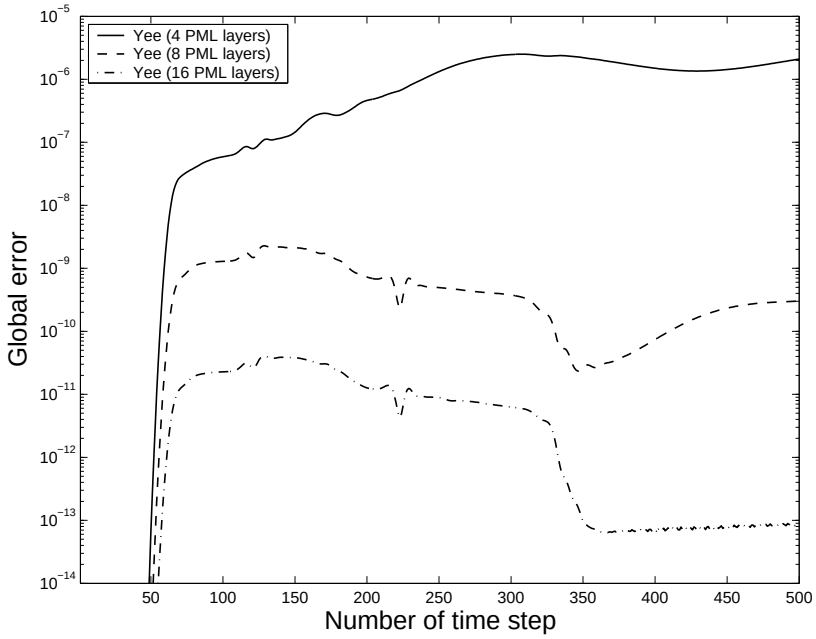

Fig. 3.41. The global error of Yee's algorithm ($\Delta s = 0.015m, S = 0.5$).

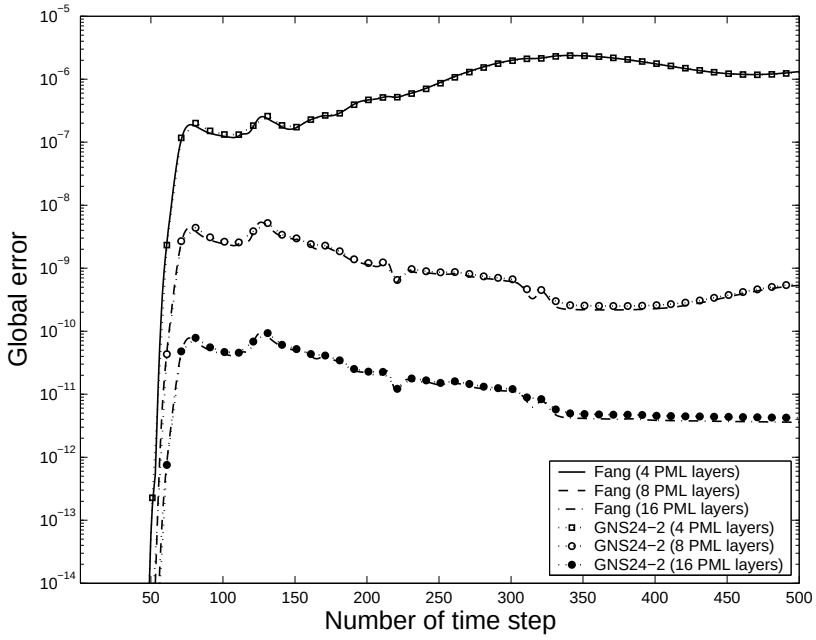

Fig. 3.42. The global errors of Fang's algorithm and the GNS24-2 scheme ($\Delta s = 0.015m, S = 0.5$).

can be found in Section 3.4.4. In the first example, the absolute errors of the resonant frequencies for the same 2D cavity are plotted in Figs. 3.43 and 3.44. The design frequencies of Figs. 3.43 and 3.44 are set to $f_0 = 0.3$ GHz and $f_0 = 0.335$ GHz, respectively. The computed coefficients for the GNS24-1 and the GNS24-2 schemes are summarized in Table 3.5. As shown, for all of the resonant frequencies, the errors generated by the GNS24-1 scheme are always smaller than those of Fang's scheme. The GNS24-2 scheme predicts precisely the resonant frequency for each case when the design frequency is set to the corresponding resonant frequency. However, the errors increase rapidly when the resonant frequency deviates from the design frequency.

Table 3.5. Computed coefficients for the GNS24 schemes ($S = 0.5, \Delta s = 0.1m$)

	$f_0 = 0.3GHz$	$f_0 = 0.335GHz$
GNS24-1	$C_1 = 1.08871679$ $C_2 = -0.02957226$	$C_1 = 1.08951410$ $C_2 = -0.02983803$
GNS24-2	$C_1 = 1.12864748$ $C_2 = -0.04437761$	$C_1 = 1.12953082$ $C_2 = -0.04508125$

In the second example, the array factor of the four-element array is also simulated using the GNS24-1 and the GNS24-2 schemes. The computed power patterns are plotted in Fig. 3.45. The computed coefficients and the L_2 errors are summarized in Table 3.6. Compared to the L_2 errors in Table 3.6, the error of the GNS24-1 is larger than those of the NS24 and INS24 schemes but smaller than that of Fang's scheme. However, the GNS24-2 scheme predicts the most accurate results.

The numerical simulations in this section clearly justifies the conclusions based on the dispersion analysis. The extension to the 3D GNS24 scheme is straightforward. In addition,

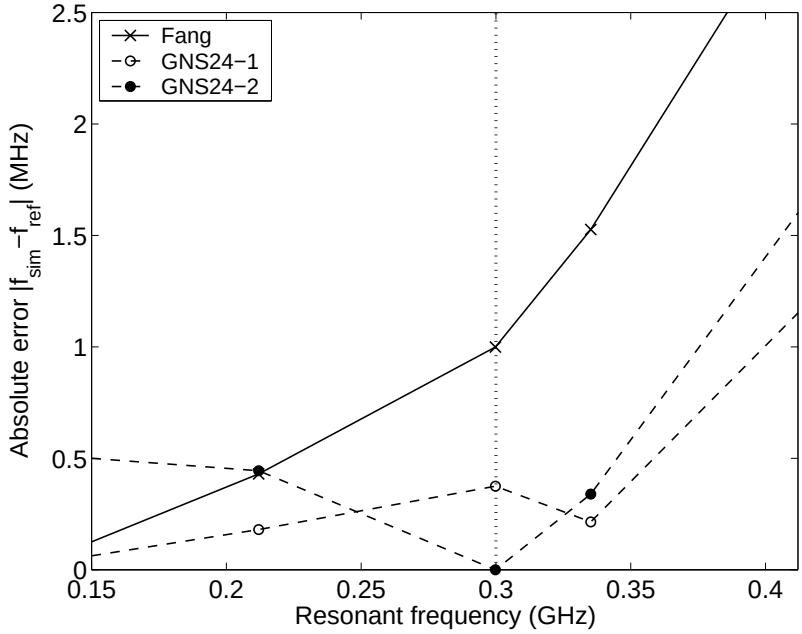

Fig. 3.43. Absolute error of the resonant frequencies of the two-dimensional PEC square cavity ($\Delta s = 0.1$ m, $S = 0.5$, $f_0 = 0.3$ GHz).

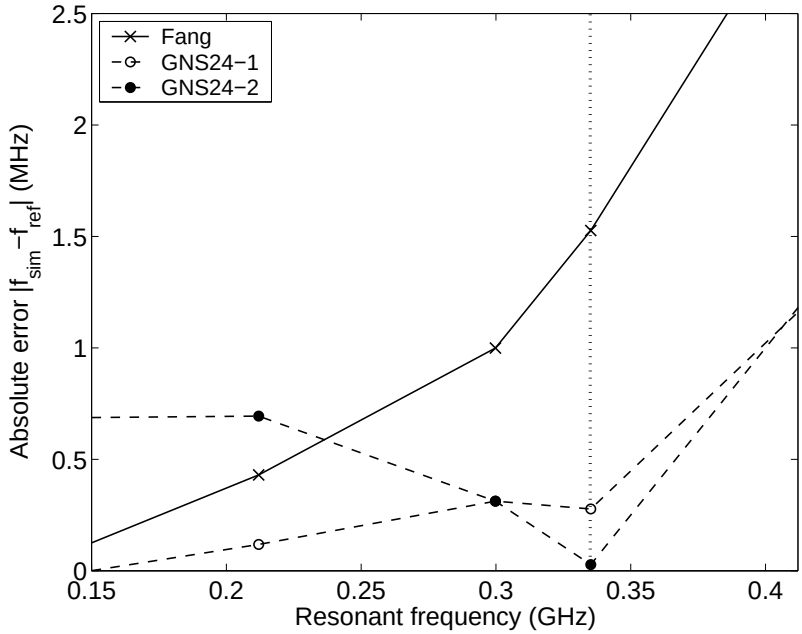

Fig. 3.44. Absolute error of the resonant frequencies of the two-dimensional PEC square cavity ($\Delta s = 0.1$ m, $S = 0.5$, $f_0 = 0.335$ GHz).

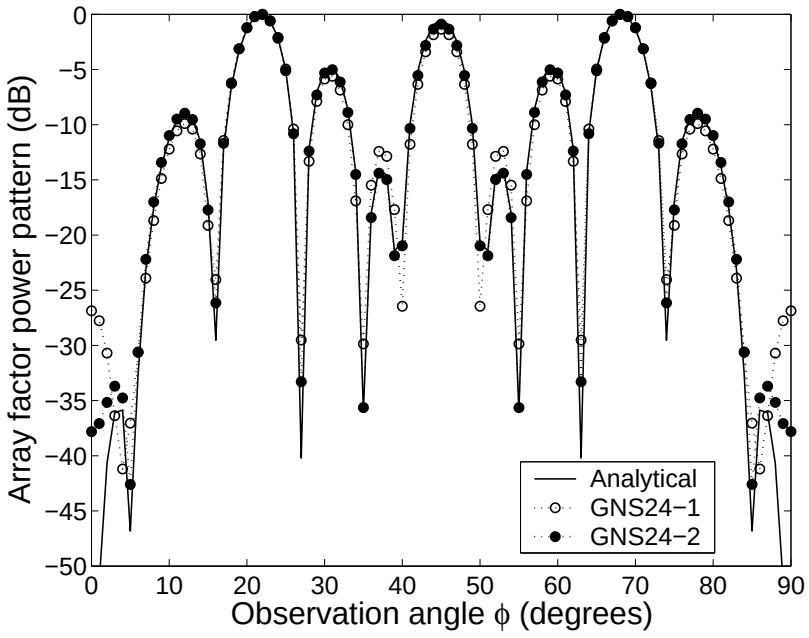

Fig. 3.45. The xy-plane array factor power pattern of the four-element array ($\Delta s = \lambda_0/6$,$S = 0.5, M = 361$).

Table 3.6. Computed coefficients and the L^2 error ($S = 0.5, \Delta s = \lambda_0/6, M = 361$)

	Coefficients	L_2 Error
GNS24-1	$C_1 = \ 1.09461960$ $C_2 = -0.03153987$	0.03989388
GNS24-2	$C_1 = \ 1.13483392$ $C_2 = -0.04977567$	0.01759012

the capability of the GNS24 scheme will be explored in the following two section.

3.5.4. The Angle-Optimized GNS24 Scheme

In practice, there are some problems in which the dispersion errors in certain propagation angles are dominant. For example, the simulation of an highly enlongated cavity or the scattering from an electrically large PEC strip. An Angle-Optimized FDTD was proposed in [57] using a filtering technique. However, to achieve the same goal of reducing the dispersion in certain angle ranges, a more straightforward approach is to use the GNS24-2 scheme.

Recall that, to obtain the stencil coefficients of the GNS24 scheme, $\tilde{k}/k$ is forced to unity in (3.41) for all angles $\phi = 1^\circ \sim 90^\circ$. If we force $\tilde{k}/k = 1$ only along the dominant directions, a scheme with low dispersion within the desired angle range can be expected. The GNS24 scheme presented in the pervious section is a special case where all directions are equally important.

Two examples are presented to verify the above argument. In Fig. 3.46, the local dispersion errors within the desired angles $\phi_i = 0^\circ \sim 15^\circ$ are plotted. In Fig. 3.47, the dominant angles are set to $\phi_i = 30^\circ \sim 60^\circ$. The computed coefficients are summarized in Table 3.7. As shown, the regular GNS24-2 scheme ($\phi_i = 0^\circ \sim 90^\circ$) exhibits an more

Table 3.7. Computed coefficients of the angle-optimized GNS24 scheme ($S = 0.5, N_0 = 10$)

	C_1	C_2
$\phi_i = 0^\circ \sim 15^\circ$	1.12862263	-0.04436822
$\phi_i = 30^\circ \sim 60^\circ$	1.12867282	-0.04438673
$\phi_i = 0^\circ \sim 90^\circ$	1.12864733	-0.04437755

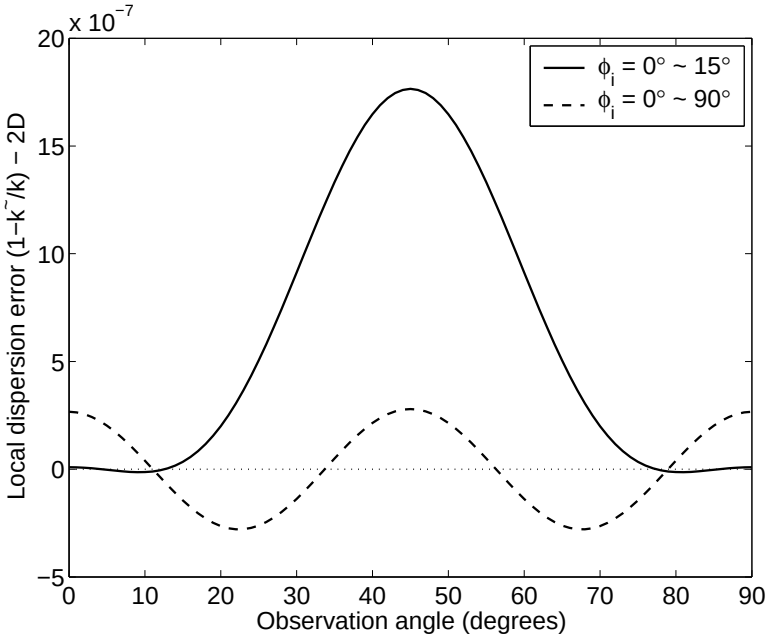

Fig. 3.46. Local dispersion error of the GNS24-2 scheme ($N_0 = 10, S = 0.5, \phi_i = 0^\circ \sim 15^\circ$).

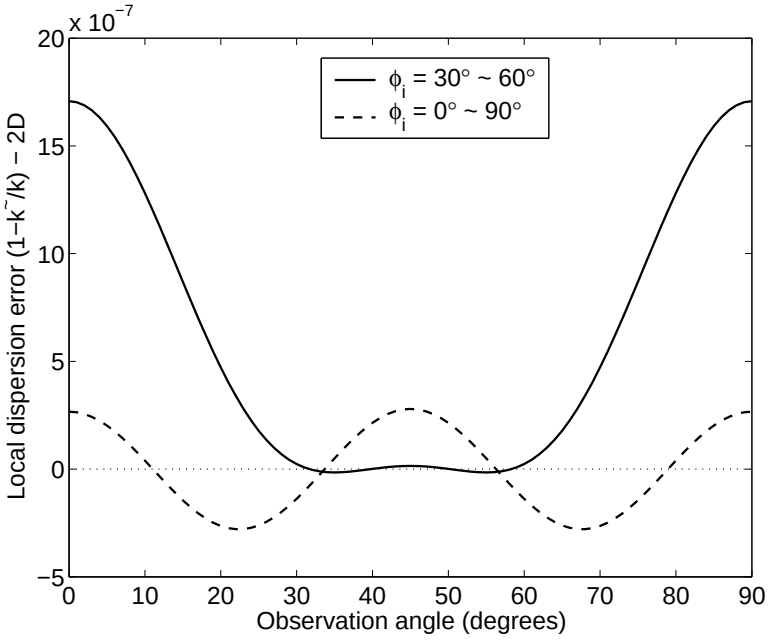

Fig. 3.47. Local dispersion error of the GNS24-2 schemes ($N_0 = 10, S = 0.5, \phi_i = 30^\circ \sim 60^\circ$).

evenly distributed dispersion. For the Angle-Optimized GNS24 (AOGNS24), the dispersion errors along the desired directions are much lower than those of the regular GNS24-2 scheme. However, for the angles of less interests, the AOGNS24 suffers from much greater dispersion errors than the regular GNS24-2 scheme. It is evident that, by properly adjusting the coefficient values of the stencil, the low dispersion directions of the AOGNS24 scheme can be flexibly controlled. Notice that the variations of the coefficient values for different angle ranges are subtle.

3.5.5. The GNS24 Scheme for the Rectangular Mesh

The dispersion analysis conducted so far are all using a square mesh ($\Delta x = \Delta y = \Delta s$). Now, we will examine the performance of the GNS24 scheme for the rectangular mesh ($\Delta x \neq \Delta y$). For the 2D case, let us assume the ratio of the space increments with respect to x and y is defined as $R = \Delta x/\Delta y > 1$. Therefore, the mesh resolutions in the x and y directions can be expressed as $N_x = \lambda/\Delta x$ and $N_y = \lambda/\Delta y = R \times N_x$, respectively. The Courant number is defined based upon the larger space step (Δx) as $S = c\Delta t/\Delta x$.

For the rectangular mesh, it can be expected that the coefficients for the stencils with respect to x and y will no longer be identical. Let C_{x1} and C_{x2} represent the coefficients for the stencil with respect to x and C_{y1} and C_{y2} represent the coefficients for the stencil with respect to y. The 2D GNS24 dispersion relation for the rectangular mesh can then be written as

$$\begin{aligned}\left(\frac{1}{c\Delta t}\right)^2 \sin^2\left(\frac{\omega\Delta t}{2}\right) &= \frac{1}{\Delta x^2}\left[C_{x1}\sin\left(\frac{\tilde{k}_x\Delta x}{2}\right) + C_{x2}\sin\left(\frac{3\tilde{k}_x\Delta x}{2}\right)\right]^2 \\ &+ \frac{1}{\Delta y^2}\left[C_{y1}\sin\left(\frac{\tilde{k}_y\Delta y}{2}\right) + C_{y2}\sin\left(\frac{3\tilde{k}_y\Delta y}{2}\right)\right]^2 \end{aligned} \quad (3.51)$$

where

$$\tilde{k}_x = \tilde{k}\cos(\phi),\ \tilde{k}_y = \tilde{k}\sin(\phi)$$

Equation (3.51) can be rewritten as

$$\frac{1}{S^2}\sin^2\left(\frac{\pi S}{N_x}\right) = \left[C_{x1}\sin\left(\frac{\pi\cos\phi}{N_x}\frac{\tilde{k}}{k}\right) + C_{x2}\sin\left(\frac{3\pi\cos\phi}{N_x}\frac{\tilde{k}}{k}\right)\right]^2 + R^2\cdot\left[C_{y1}\sin\left(\frac{\pi\sin\phi}{RN_x}\frac{\tilde{k}}{k}\right) + C_{y2}\sin\left(\frac{3\pi\sin\phi}{RN_x}\frac{\tilde{k}}{k}\right)\right]^2 \tag{3.52}$$

The procedure to solve $\tilde{k}/k$ in (3.52) is very similar to the square mesh case, while now there are totally four unknowns C_{x1}, C_{x2}, C_{y1}, and C_{y2}. For $R = 2$, $N_{x0} = 10$, and $S = 0.25$, the coefficients for the GNS24-2 scheme are computed and summarized in Table 3.8.

Table 3.8. Computed GNS24-2 coefficients for the rectangular mesh ($R = 2, N_{x0} = 10, S = 0.25$).

C_{x1}	1.05281421
C_{x2}	-0.01421612
C_{y1}	1.46453965
C_{y2}	-0.15900394

The local dispersion errors of the Fang's algorithm and the GNS24-2 scheme are plotted in Figs. 3.48 and 3.49, respectively. It is evident that the dispersion curve for Fang's algorithm is no longer 90° periodic. Compared to the curves for the square mesh in Fig. 2.19, a high dispersion error is observed in the vicinity of $\phi = 90°$ due to the different mesh resolutions in the x and y directions. However, the effects of the rectangular mesh is automatically compensated by the GNS24-2 scheme. A very low and more isotropic dispersion distribution can be observed.

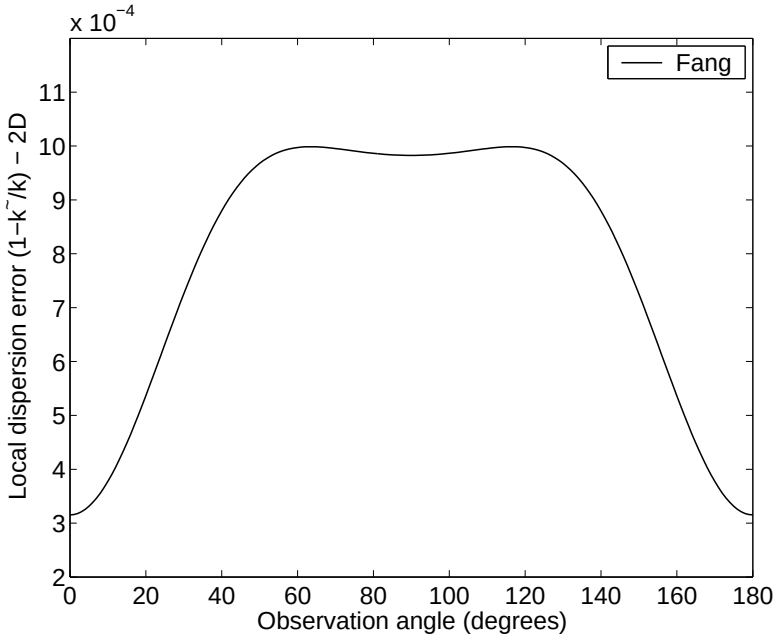

Fig. 3.48. Local dispersion error of Fang's scheme ($R = 2, N_{x0} = 10, S = 0.25$).

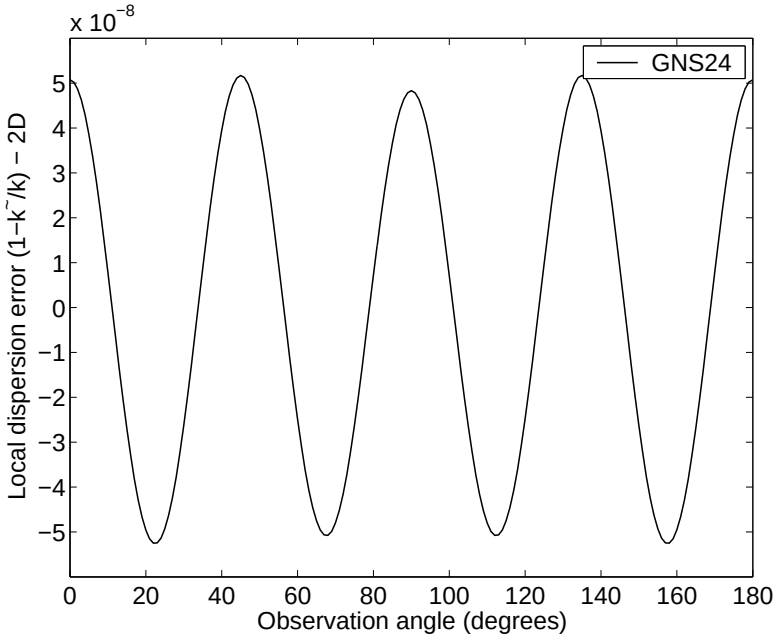

Fig. 3.49. Local dispersion error of the GNS24-2 schemes ($R = 2, N_{x0} = 10, S = 0.25$).

3.5.6. More Complex Stencils

The procedure summarized in the previous sections can be applied, but not limited to, the GNS24 scheme. More complex stencils can be derived following a similar procedure. In this section, an "Isotropic" Finite Difference (IFD) presented in [28] will be considered as an example. In two dimensions, the space stencil of the generalized IFD scheme (GIFD) uses six-point stencils which can be expressed as

$$\begin{aligned} D_x(f_{i,j}) &= \frac{D_1(f_{i+1/2,j} - f_{i-1/2,j})}{\Delta s} \\ &+ \frac{D_2(f_{i+1/2,j+1} + f_{i+1/2,j-1} - f_{i-1/2,j+1} - f_{i-1/2,j-1})}{\Delta s} \end{aligned} \tag{3.53}$$

$$\begin{aligned} D_y(f_{i,j}) &= \frac{D_1(f_{i,j+1/2} - f_{i,j-1/2})}{\Delta s} \\ &+ \frac{D_2(f_{i+1,j+1/2} + f_{i-1,j+1/2} - f_{i+1,j-1/2} - f_{i-1,j-1/2})}{\Delta s} \end{aligned} \tag{3.54}$$

where D_1 and D_2 are undetermined coefficients. If $D_1 = 11/12$ and $D_2 = 1/24$, (3.53) and (3.54) reduce to the regular IFD scheme in [28]. The 2D stencils for the GIFD stencils are illustrated in Fig. 3.50.

From Taylor series expansion, it can be derived that the constraint for (3.53) and (3.54) to maintain the second-order accuracy is

$$D_1 + 2D_2 = 1 \text{ or } D_1 = 1 - 2D_2 \tag{3.55}$$

Similarly, a more relaxed constraint is

$$D_1 + 2D_2 = q \text{ or } D_1 = q - 2D_2 \tag{3.56}$$

where q is an extra free parameter. We refer the scheme using (3.55) as GIFD26-1 and the scheme using (3.56) as GIFD26-2.

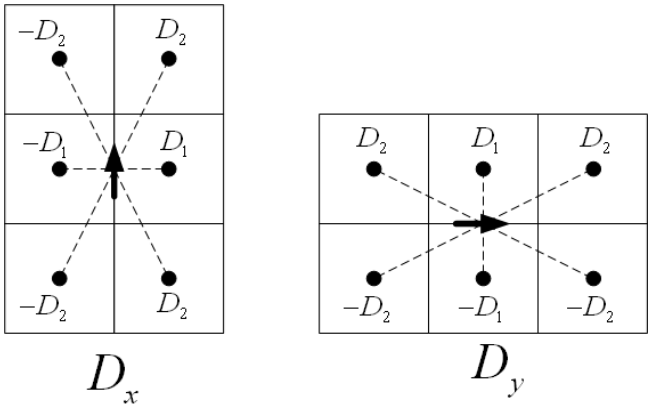

Fig. 3.50. The 2D general six-point stencils.

The dispersion relation of the general (2,6) scheme can be derived and written as

$$\begin{aligned}\frac{1}{S^2}\sin^2\left(\frac{\pi S}{N}\right) &= \left[D_1+2D_2\cos\left(\frac{2\pi\sin\phi}{N}\frac{\tilde{k}}{k}\right)\right]^2\sin^2\left(\frac{\pi\cos\phi}{N}\frac{\tilde{k}}{k}\right)\\ &+ \left[D_1+2D_2\cos\left(\frac{2\pi\cos\phi}{N}\frac{\tilde{k}}{k}\right)\right]^2\sin^2\left(\frac{\pi\sin\phi}{N}\frac{\tilde{k}}{k}\right)\end{aligned} \tag{3.57}$$

Following a similar procedure, I equations are obtained by forcing $\tilde{k}/k = 1$ at $N = N_0$ along $\phi_i = 0^\circ \sim \cdots, 90^\circ, i = 1, 2, \cdots, I$. This leads to a nonlinear overdetermined system which can be expressed as

$$F_i(D_1, D_2) = b_i^2[D_1 + 2a_iD_2]^2 + d_i^2[D_1 + 2c_iD_2]^2 - e = 0, i = 1, 2, \cdots, I \tag{3.58}$$

where

$$\begin{aligned}a_i &= \cos\left(\frac{2\pi\sin\phi_i}{N_0}\right),\ b_i = \sin\left(\frac{\pi\cos\phi_i}{N_0}\right)\\ c_i &= \cos\left(\frac{2\pi\cos\phi_i}{N_0}\right),\ d_i = \sin\left(\frac{\pi\sin\phi_i}{N_0}\right)\\ e &= \frac{1}{S^2}\sin^2\left(\frac{\pi S}{N_0}\right)\end{aligned}$$

Equation (3.58) can be rewritten as

$$F_i(D_1, D_2) = f_i D_1^2 + g_i D_2^2 + h_i D_1 D_2 - e = 0, i = 1, 2, \cdots, I \tag{3.59}$$

where

$$\begin{aligned} f_i &= b_i^2 + d_i^2 \\ g_i &= 4(a_i^2 b_i^2 + c_i^2 d_i^2) \\ h_i &= 4(a_i b_i^2 + c_i d_i^2) \end{aligned}$$

The resultant overdetermined system in (3.59) can be solved following a similar procedure summarized in (3.44)-(3.48). The initial values are chosen to be the coefficients for the regular six-point stencil, i.e.,$\mathbf{D}_0 = [11/12, 1/24]$. The computed coefficients using $I = 401$ for different N_0 are summarized in Table 3.9.

Table 3.9. Computed coefficients for the GIFD26 schemes ($S = 0.5$)

	$N_0 = 10$	$N_0 = 20$
GIFD26-1	$D_1 = 1.08464967$ $D_2 = -0.04232484$	$D_1 = 1.08365977$ $D_2 = -0.04182988$
GIFD26-2	$D_1 = 0.92662022$ $D_2 = 0.04292245$	$D_1 = 0.91913928$ $D_2 = 0.04197646$

Using the computed coefficients, the local dispersion errors for the IFD26, GIFD26-1, and GIFD26-2 schemes are plotted in Fig. 3.51. As shown, the IFD26 scheme does exhibit an "isotropic" dispersion distribution; the dispersion variation with angles is negligible. However, the average level of its dispersion is still very high. The average dispersion error of the GIFD26-1 scheme is smaller than that of the IFD26 scheme, while it suffers from

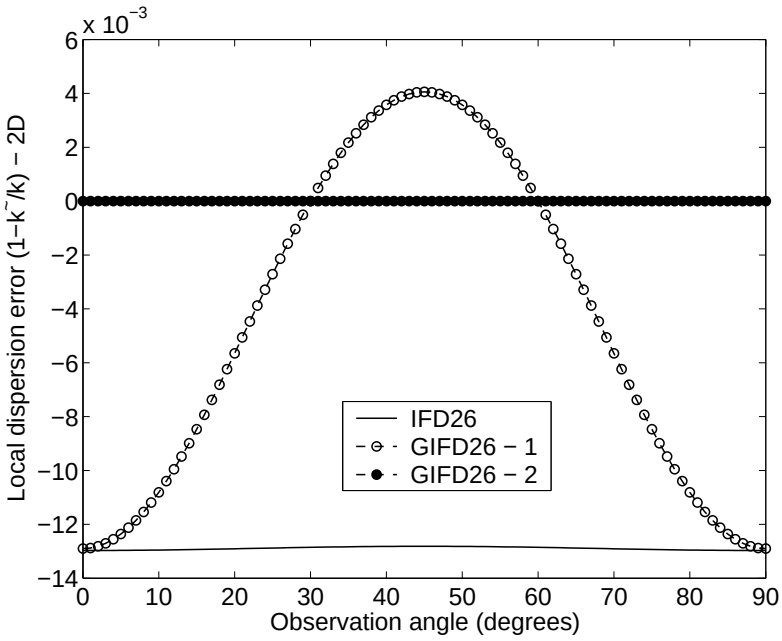

Fig. 3.51. Local dispersion error of the GIFD26 schemes ($N = N_0 = 10, S = 0.5$).

more anisotropy. As a comparison, the GIFD26-2 scheme exhibits no visible dispersion error at $N = N_0$.

The global dispersion errors for $N_0 = 10$ and $N_0 = 20$ are plotted in Figs. 3.52-3.53, respectively. It is evident that the GIFD26-1 algorithm is a broad-band scheme in terms of the average dispersion error. However, the GIFD26-2 scheme is a narrow-band scheme. At the corresponding mesh resolution, the minimum dispersion errors are even smaller than those of the GNS24-2 scheme in Figs. 3.34 and 3.35.

3.5.7. Stability Condition

Another important issue for the NSFD methods is the stability condition which guarantees the convergence of the algorithm. Conventionally, the stability condition can be obtained by performing a Von Neuman analysis [88] or following a more concise approach

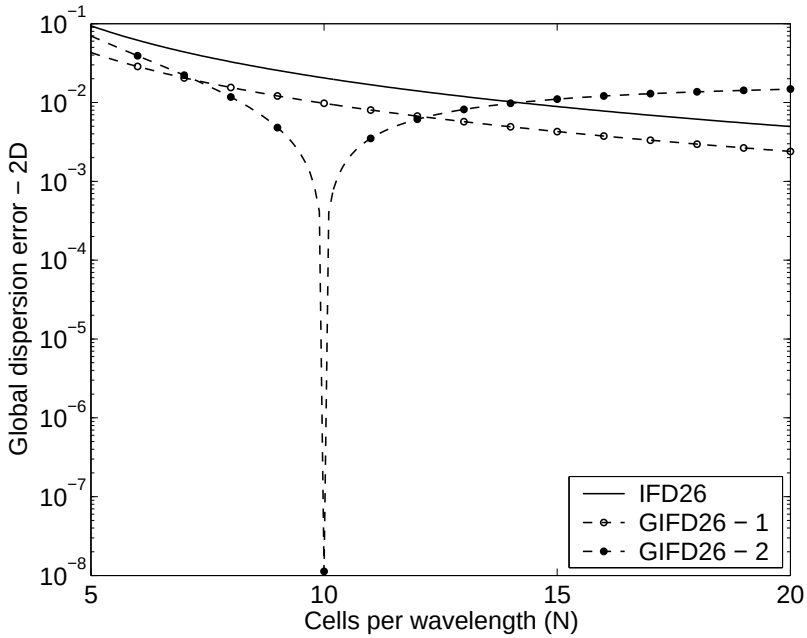

Fig. 3.52. Global dispersion error of the GIFD26 schemes ($N_0 = 10, S = 0.5$).

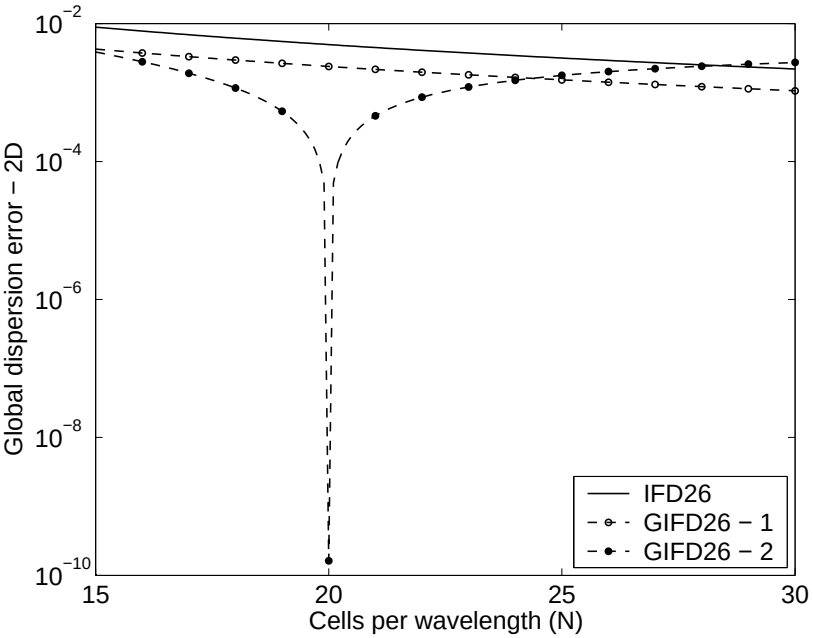

Fig. 3.53. Global dispersion error of the GIFD26 schemes ($N_0 = 20, S = 0.5$).

based on the complex frequency analysis. In this section, the procedure of [1] will be used to solve the stability condition for the NSFD algorithms.

Let us consider the 2D GNS24-2 scheme as an example. In (3.51), solving for ω leads to

$$\omega = \frac{2}{\Delta t}\sin^{-1}(\xi) \tag{3.60}$$

where

$$\xi = c\Delta t\sqrt{\begin{array}{c}\frac{1}{\Delta x^2}\left[C_{x1}\sin\left(\frac{\tilde{k}_x\Delta x}{2}\right)+C_{x2}\sin\left(\frac{3\tilde{k}_x\Delta x}{2}\right)\right]^2\\ +\frac{1}{\Delta y^2}\left[C_{y1}\sin\left(\frac{\tilde{k}_y\Delta y}{2}\right)+C_{y2}\sin\left(\frac{3\tilde{k}_y\Delta y}{2}\right)\right]^2\end{array}} \tag{3.61}$$

To guarantee that ω in (3.60) has a real value, ξ in (3.61) must satisfy $\xi \leq 1$. Since $C_{x1} > 0, C_{x2} < 0$ and $C_{y1} > 0, C_{y2} < 0$, the maximum value of ξ is achieved when $(\tilde{k}_x\Delta x)/2 = (\tilde{k}_y\Delta y)/2 = \pi/2$. Consequently,

$$\xi_{max} \quad = \quad c\Delta t\sqrt{\frac{(C_{x1}-C_{x2})^2}{\Delta x^2}+\frac{(C_{y1}-C_{y2})^2}{\Delta y^2}} \leq 1 \tag{3.62}$$

Rearranging (3.62), we obtain

$$\Delta t \leq \frac{1}{c\sqrt{\frac{(C_{x1}-C_{x2})^2}{\Delta x^2}+\frac{(C_{y1}-C_{y2})^2}{\Delta y^2}}} \quad \text{(2D)} \tag{3.63}$$

which is the stability condition for the 2D GNS24-2 algorithm. Following a similar procedure, the 1D and 3D stability conditions can be derived and expressed as

$$\Delta t \leq \frac{\Delta x}{c(C_1 - C_2)} \quad \text{(1D)} \tag{3.64}$$

$$\Delta t \leq \frac{1}{c\sqrt{\frac{(C_{x1}-C_{x2})^2}{\Delta x^2}+\frac{(C_{y1}-C_{y2})^2}{\Delta y^2}+\frac{(C_{z1}-C_{z2})^2}{\Delta z^2}}} \quad \text{(3D)} \tag{3.65}$$

For the cubic mesh case ($\Delta x = \Delta y = \Delta z = \Delta s$), the stability conditions reduce to

$$S = \frac{c\Delta t}{\Delta s} \leq \frac{1}{(C_1 - C_2)} \quad \text{(1D)} \tag{3.66}$$

$$S = \frac{c\Delta t}{\Delta s} \leq \frac{1}{\sqrt{2}(C_1 - C_2)} \quad \text{(2D)} \tag{3.67}$$

$$S = \frac{c\Delta t}{\Delta s} \leq \frac{1}{\sqrt{3}(C_1 - C_2)} \quad \text{(3D)} \tag{3.68}$$

3.6. Gauss's Laws

Maxwell's equations contain Faraday's Law in (2.5), Ampere's Law in (2.6) and Gauss's Laws for electric and magnetic fields in (2.7) and (2.8). However, most FDTD methods only differentiate the former two equations without considering the two Gauss's Laws. Therefore, it is important to justify that any FDTD scheme also satisfies Gauss's Laws. In source-free regions, this requires that no artificial electric and magnetic charges are generated inside the domain. In Cartesian coordinates, it has been verified that Yee's algorithm satisfies Gauss's Law for rectangular meshes [1]. However, it remains unclear if the NSFD methods meet this fundamental requirement. In this section, Gauss's Law for the electric fields will be examined for the NSFD algorithms. Gauss's Law for the magnetic fields can be derived following a very similar procedure. For conciseness, only the 2D (TE^z) case is considered. The derivations for the 2D (TM^z) and the 3D cases are similar.

In a 2D free-space region, Gauss's Law for electric fields can be written in both the differential and integral forms as

$$\text{Differential form:} \qquad \nabla \cdot \vec{D} = 0 \tag{3.69}$$

$$\text{Integral form:} \qquad \oint_C \vec{D} \cdot \vec{dl} = 0 \tag{3.70}$$

where C is an arbitrary closed contour. The time derivatives of Gauss's Laws in (3.69) and (3.70) are also zero since all the fields at the initial time are zero. Two semi-discretized NSFD update equations for the E_x and E_y fields

$$\epsilon_0 \frac{\partial}{\partial t} E_x|_{i+1/2,j} = D_y^{ns}(H_z|_{i+1/2,j}) \tag{3.71}$$

$$\epsilon_0 \frac{\partial}{\partial t} E_y|_{i,j+1/2} = -D_x^{ns}(H_z|_{i,j+1/2})) \tag{3.72}$$

will be used in the derivation. In (3.71) and (3.72), D_x^{ns} and D_y^{ns} represent the NSFD space stencils with respect to x and y, which could be the NS, INS, or GNS operators introduced in the previous sections.

In the 2D Cartesian coordinates, the rectangular FDTD grids ($\Delta x \neq \Delta y$) are shown in Fig. 3.54. For clarity, the position index of each field component is suppressed. All the involved fields are numbered in sequence according to the superscripts. Two closed contours, designated as L_1 and L_2, are also illustrated in Fig. 3.54. Gauss's Law in differential form is defined at the center point which is represented by the empty circle in Fig. 3.54 while Gauss's Law in integral form describes the total charge encompassed by the L_1 contour.

3.6.1. The NS22 Scheme

As a first example, let us consider the NS22 scheme where D_x^{ns} and D_y^{ns} are given as

$$D_x^{ns22} f_i = \frac{(f_{i+1/2} - f_{i-1/2})}{sk_x} \tag{3.73}$$

$$D_y^{ns22} f_j = \frac{(f_{j+1/2} - f_{j-1/2})}{sk_y} \tag{3.74}$$

where sk_x and sk_y are correction parameters which possess different values for the rectangular mesh. Using the standard second-order central difference, the time derivative of

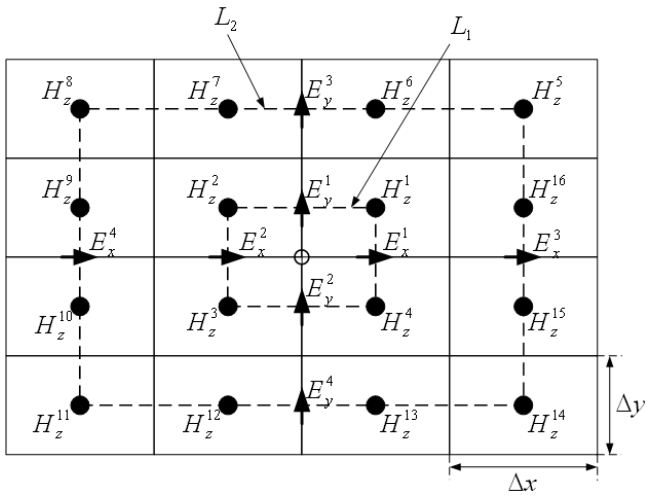

Fig. 3.54. Illustration of the 2D rectangular FDTD grids (TE^z).

(3.69) can be differentiated and written as

$$\begin{aligned} \frac{\partial}{\partial t}\nabla\cdot\vec{D} &= \varepsilon_0\frac{\partial}{\partial t}\left(\frac{\partial E_x}{\partial x}+\frac{\partial E_y}{\partial y}\right) \\ &\approx \varepsilon_0\frac{\partial}{\partial t}\left(\frac{E_x^1-E_x^2}{\Delta x}+\frac{E_y^1-E_y^2}{\Delta y}\right) \end{aligned} \tag{3.75}$$

where E_x^1, E_x^2 and E_y^1, E_y^2 are used to evaluate the derivatives in the x and y directions, respectively. Substituting (3.71) and (3.72) for NS22 into (3.75) yields

$$\frac{\partial}{\partial t}\nabla\cdot\vec{D}\approx(H_z^1-H_z^4-H_z^2+H_z^3)\left(\frac{1}{sk_y\Delta x}-\frac{1}{sk_x\Delta y}\right) \tag{3.76}$$

Notice that, for arbitrary H_z-fields, Gauss's Law will not be satisfied unless the following constraint

$$\frac{sk_x}{\Delta x}=\frac{sk_y}{\Delta y} \tag{3.77}$$

is met. It is evident that the optimal sk_x and sk_y values for the regular NS22 scheme, defined in (3.4), do not satisfy this constraint. In other words, the regular NS22 scheme does not satisfy Gauss's Law using the standard differentiation. If we were to enforce the constraint in (3.77), the optimal values of sk_x and sk_y, defined in (3.4), will not be obtained. Consequently, the dispersion performance of the NS22 scheme will be compromised.

Naturally, an alternative way of differentiating (3.75) is to use the NS22 operators in (3.73) and (3.74), which are self-consistent to the scheme. Following a similar procedure, this leads to

$$\begin{aligned} \frac{\partial}{\partial t}\nabla\cdot\vec{D} &\approx \varepsilon_0\frac{\partial}{\partial t}\left(\frac{E_x^1-E_x^2}{sk_x}+\frac{E_y^1-E_y^2}{sk_y}\right) \\ &= (H_z^1-H_z^4-H_z^2+H_z^3)\left(\frac{1}{sk_ysk_x}-\frac{1}{sk_xsk_y}\right)=0 \end{aligned} \tag{3.78}$$

That is, Gauss's Law in differential form is satisfied.

In Cartesian coordinate, Gauss's Law in integral form can be evaluated along the L_1 contour. This leads to

$$\frac{\partial}{\partial t}\oint_C \vec{D}\cdot\vec{dl} \approx \epsilon_0\frac{\partial}{\partial t}[(E_x^1-E_x^2)\Delta y+(E_y^1-E_y^2)\Delta x] \tag{3.79}$$

Substituting (3.71) and (3.72) into (3.79) and collecting terms yields

$$\frac{\partial}{\partial t}\oint_C \vec{D}\cdot\vec{dl} \approx (H_z^1-H_z^4-H_z^2+H_z^3)\left(\frac{\Delta y}{sk_y}-\frac{\Delta x}{sk_x}\right) \tag{3.80}$$

Clearly, forcing (3.80) equal to zero leads to the same constraint as in (3.77). Again, if Δx and Δy in (3.79) are replaced by sk_x and sk_y, respectively, Gauss's Law in integral form is satisfied.

3.6.2. The GNS24 Scheme

Next, let us consider the 2D GNS24 scheme. The NS and INS schemes are special cases of the GNS24 scheme. The space stencils of the 2D GNS24 scheme are repeated as

$$D_x^{gns24} f_i = \frac{C_{x1}(f_{i+1/2} - f_{i-1/2}) + C_{x2}(f_{i+3/2} - f_{i-3/2})}{\Delta x} \tag{3.81}$$

$$D_y^{gns24} f_j = \frac{C_{y1}(f_{j+1/2} - f_{j-1/2}) + C_{y2}(f_{j+3/2} - f_{j-3/2})}{\Delta y} \tag{3.82}$$

Following a similar procedure, (3.69) can be differentiated using the standard fourth-order stencil and written as

$$\begin{aligned} \frac{\partial}{\partial t}\nabla \cdot \vec{D} &\approx \varepsilon_0 \frac{\partial}{\partial t}\left[\frac{\frac{27}{24}(E_x^1 - E_x^2) - \frac{1}{24}(E_x^3 - E_x^4)}{\Delta x}\right] \\ &+ \varepsilon_0 \frac{\partial}{\partial t}\left[\frac{\frac{27}{24}(E_y^1 - E_y^2) - \frac{1}{24}(E_y^3 - E_y^4)}{\Delta y}\right] \end{aligned} \tag{3.83}$$

where E_x^1, E_x^2, E_x^3, E_x^4 and E_y^1, E_y^2, E_y^3, E_y^4 are used to evaluate the derivatives in the x and y directions, respectively. Substituting (3.71) and (3.72) for GNS24-2 into (3.83) yields

$$\begin{aligned} \frac{\partial}{\partial t}\nabla \cdot \vec{D} &\approx [(27(C_{y1} - C_{x1})(H_z^1 - H_z^4 - H_z^2 + H_z^3) \\ &+ (27C_{y2} + C_{x1})(H_z^6 - H_z^{13} - H_z^7 + H_z^{12}) \\ &- (27C_{x2} + C_{y1})(H_z^{16} - H_z^{15} - H_z^9 + H_z^{10}) \\ &- (C_{y2} - C_{x2})(H_z^5 - H_z^{14} - H_z^8 + H_z^{11})] \cdot \frac{1}{24\Delta x \Delta y} \end{aligned}$$

Similar to the NS22 case, Gauss's Law will not be satisfied unless the following constraints

$$C_{x1} = C_{y1} = C_1 \tag{3.84}$$

$$C_{x2} = C_{y2} = C_2 \tag{3.85}$$

$$C_1 + 27C_2 = 0 \tag{3.86}$$

are met. It can be verified that the optimal GNS24 coefficients in Table 3.5.5 do not satisfy these constraints. Enforcing these extra constraints on the stencil coefficients compromises the dispersion performance.

An alternative way of differentiating (3.69) is to use the GNS24 operators defined in (3.81) and (3.82). This leads to zero divergence and can be expressed as

$$\begin{aligned} \frac{\partial}{\partial t}\nabla\cdot\vec{D} &\approx \varepsilon_0\frac{\partial}{\partial t}\left[\frac{C_{x1}(E_x^1-E_x^2)+C_{x2}(E_x^3-E_x^4)}{\Delta x}\right] \\ &+ \varepsilon_0\frac{\partial}{\partial t}\left[\frac{C_{y1}(E_y^1-E_y^2)+C_{y2}(E_y^3-E_y^4)}{\Delta y}\right]=0 \end{aligned} \tag{3.87}$$

For Gauss's Law in integral form, a direct integration along L_1 leads to

$$\begin{aligned} \frac{\partial}{\partial t}\oint_C \vec{D}\cdot\vec{dl} &\approx (C_{y1}-C_{x1})(H_z^1-H_z^4-H_z^2+H_z^3) \\ &+ C_{y2}(H_z^6-H_z^{13}-H_z^7+H_z^{12}) \\ &+ C_{x2}(H_z^{16}-H_z^9-H_z^{15}+H_z^{10}) \end{aligned} \tag{3.88}$$

For arbitrary H_z fields, the second and third terms in (3.88) will never vanish unless $C_{x2} = C_{y2} = 0$.

However, multiplying both sides of (3.88) with $\Delta x\Delta y$ and reorganizing, we obtain

$$\begin{aligned} (\Delta x\Delta y)\frac{\partial}{\partial t}\nabla\cdot\vec{D} &\approx \varepsilon_0\frac{\partial}{\partial t}\left[C_{x1}(E_x^1-E_x^2)\Delta y+C_{y1}(E_y^1-E_y^2)\Delta x\right] \\ &+ \varepsilon_0\frac{\partial}{\partial t}\left[\frac{C_{x2}}{3}(E_x^3-E_x^4)3\Delta y+\frac{C_{y2}}{3}(E_y^3-E_y^3)3\Delta x\right] \\ &\approx \oint_{L_1}\vec{D}\cdot\vec{dl}+\oint_{L_2}\vec{D}\cdot\vec{dl} \end{aligned} \tag{3.89}$$

Thus, the integral-form of Gauss's Law can be approximated using the weighted sum of the closed integrals along two contours: L_1 and L_2. Since (3.89) is derived from Gauss's Law in differential form, the same statements can be made for Gauss's Law in integral form.

That is, the standard formulation does not satisfy Gauss's Law unless extra constraints are enforced. However, using the nonstandard formulation, Gauss's Law is automatically satisfied.

To further evaluate Gauss's Laws, a simple numerical simulation is performed, as shown in Fig. 3.55. A free-space region (TE^z), excited with a soft Gaussian pulse ($n_{decay} = 10$, $n_0 = 3n_{decay}$ [1]) at the domain center (i_s, j_s), is simulated using both the NS22 and the GNS24-2 schemes. The design frequency for each of the scheme is set to $f_0 = 300$ MHz. The simulation domain is large enough so that there is no reflection from the edges within the simulation duration of interest. Rectangular cells with $\Delta x = 0.1$m and $\Delta y = 0.05$m are used. The Courant number is set to $S = 0.25$. Electric charge densities at a point away from the source $(i_s + 3, j_s + 3)$ are computed and normalized with $D_x(i_s, j_s)$. The normalized electric charge densities are plotted in Fig. 3.56 using the standard differentiation of (3.75) and (3.83) in Fig. 3.57 using the nonstandard differentiation of (3.78) and (3.87). It is evident that artificial charges are observed in the source-free region if the standard formulations are used. However, the nonstandard formulations reduce the artificial charges by a factor of nearly 10^4.

Based on the above discussions, the following conclusions can be made concerning Gauss's Laws for the NSFD algorithms. In the source-free region, the standard formulations do not satisfy Gauss's Law unless extra constraints on the stencil coefficients are enforced. These constraints are not desirable since they sacrifice the dispersion performance of the NSFD schemes. Using the nonstandard formulations, Gauss's Law (both in differential and integral forms) is automatically satisfied.

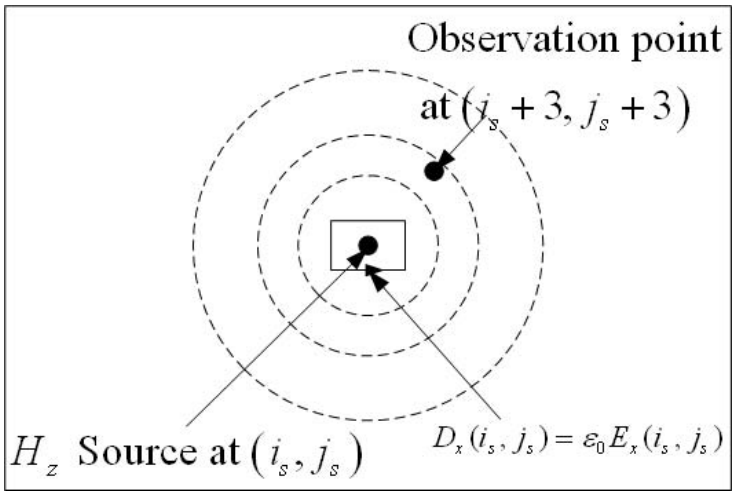

Fig. 3.55. Geometry of the simulated free-space region.

3.7. The Material Interface Conditions

One of the greatest barriers for the schemes using the extended stencils is the proper material interface treatments. Even if there is no staircase error, the extended stencils fail to accurately predict the interaction near the material interfaces [85]. Many efforts have been made to minimize the errors due to material interfaces. Among them, there are the hybrid FDTD(2,2)/FDTD(2,4) scheme [72]– [76], the one-sided stencils [77], [78], and the derivative-matching technique [81]. Recently, a very different approach was presented for Yee's algorithm to reduce the artifacts due to the material discontinuities [82]– [84]. The approach used in [82]– [84] is similar to that used to derive the NSFD algorithms. That is, the coefficients in the space stencils are allowed to be adjusted. By forcing the numerical results to be equal to the exact solutions at a certain design frequency, the values of those free coefficients can be determined. In this report, the basic concept of [82]– [84] is extended to the four-point finite difference stencils.

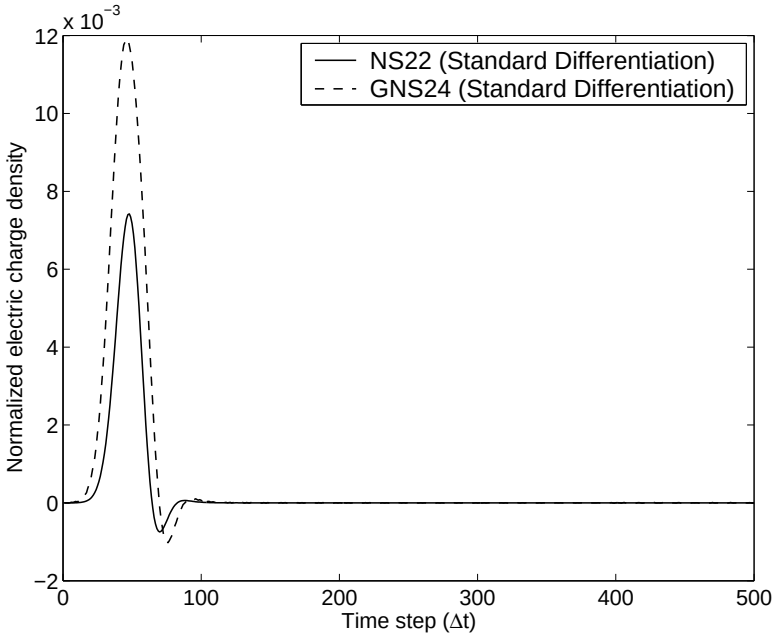

Fig. 3.56. Normalized electric charge densities using the standard differentiation of (3.75) and (3.83).

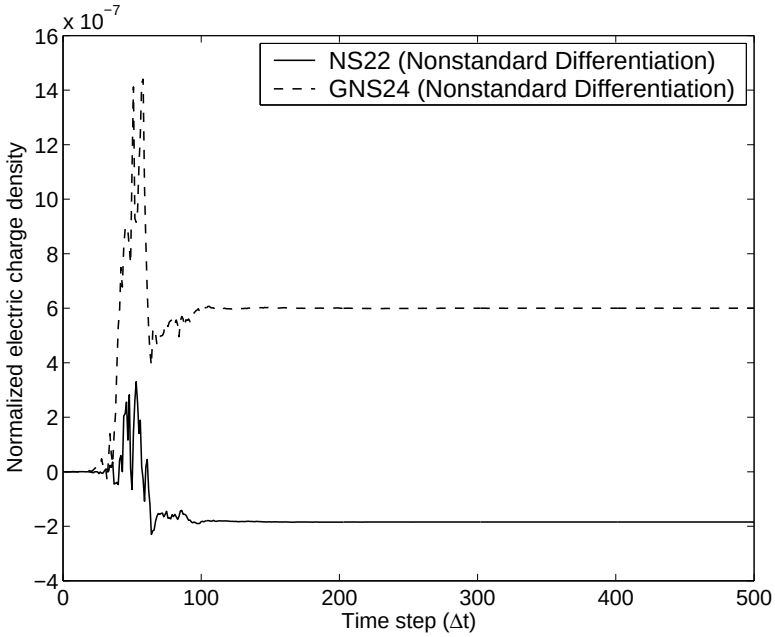

Fig. 3.57. Normalized electric charge densities using the nonstandard differentiation of (3.78) and (3.87).

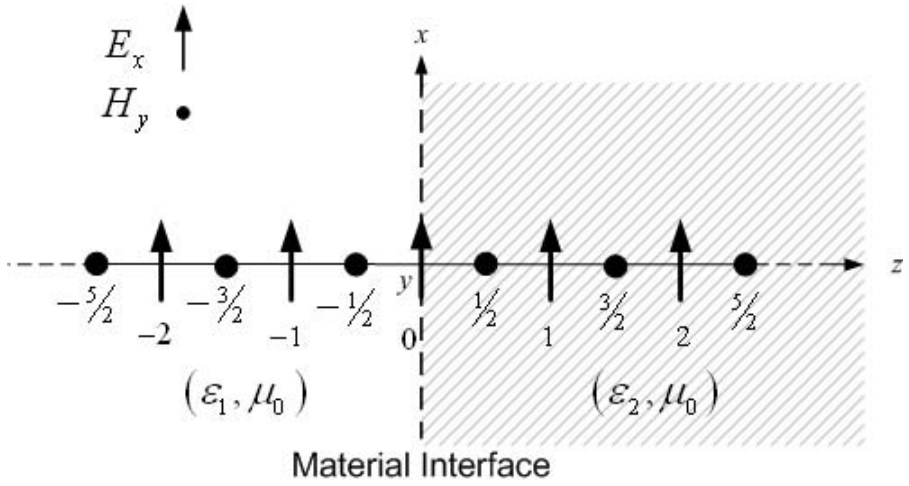

Fig. 3.58. One-dimensional material discontinuity.

3.7.1. Formulation

In a one-dimensional homogeneous medium, x-polarized plane waves traveling in $\pm z$ directions can be modeled by Maxwell's equations in the form of

$$-\frac{\partial E_x}{\partial t} = \frac{1}{\epsilon}\frac{\partial H_y}{\partial z} \tag{3.90}$$

$$-\frac{\partial H_y}{\partial t} = \frac{1}{\mu}\frac{\partial E_x}{\partial z} \tag{3.91}$$

Let us consider that a dielectric discontinuity, formed by two different dielectric media (ϵ_1 and ϵ_2) exists at $z = 0$, as shown in Fig. 3.58. A uniform mesh, with the space step Δz is used everywhere. Without loss of generality, an E_x field is located at the interface ($z = 0$).

The exact solutions, for the normalized E- and H-fields in the two different media, are given as [2]

Medium 1:

$$E^1 = \left(e^{-jk_1 z} + \Gamma e^{jk_1 z}\right) \tag{3.92}$$

$$H^1 = \frac{1}{\eta_1}\left(e^{-jk_1 z} - \Gamma e^{jk_1 z}\right) \tag{3.93}$$

Medium 2:

$$E^2 = (1+\Gamma)e^{-jk_2 z} \tag{3.94}$$

$$H^2 = \frac{(1+\Gamma)}{\eta_2} e^{-jk_2 z} \tag{3.95}$$

where η_1 and η_2 are the wave impedances in medium 1 and 2, respectively; k_1 and k_2 are the wave numbers in different media at a design frequency f_0; and Γ is the reflection coefficient from medium 1 toward medium 2 at the interface, which can be written as

$$\Gamma = \frac{\eta_2 - \eta_1}{\eta_2 + \eta_1} \tag{3.96}$$

In a homogeneous medium, the regular fourth-order finite difference stencil [15]

$$D(f_i) = \frac{f_{i-3/2} - 27 f_{i-1/2} + 27 f_{i+1/2} - f_{i+3/2}}{\Delta z} \tag{3.97}$$

can be used to discretize the space derivatives in (3.90) and (3.91). However, the direct application of (3.97) near the dielectric interface will cause significant errors [85]. In [81], it was reported that these errors can be greatly reduced by using a modified stencil near the interface, which can be expressed as

$$\tilde{D}(f_i) = \frac{C_1 f_{i-3/2} + C_2 f_{i-1/2} + C_3 f_{i+1/2} + C_4 f_{i+3/2}}{\Delta z} \tag{3.98}$$

where C_1, C_2, C_3, and C_4 are unknown coefficients which need to be optimized. The regular fourth-order stencil in (3.97) can be viewed as a special case of (3.98). In Fig. 3.58, three

E-fields (at $z = -\Delta z, 0, \Delta z$) and two H-fields (at $z = -\Delta z/2, \Delta z/2$) will be influenced by the material discontinuities due to the width of the four-point stencil. Therefore, the update equations for the $E-$ and $H-$ fields near the interface can be modified as

$$\frac{\left(E|_i^{n+1} - E|_i^n\right)}{\Delta t} = -\frac{1}{\epsilon_i}\tilde{D}\left(H|_i^{n+1/2}\right), i = -1, 0, 1 \tag{3.99}$$

$$\frac{\left(H|_i^{n+1/2} - H|_i^{n-1/2}\right)}{\Delta t} = -\frac{1}{\mu_i}\tilde{D}\left(E|_i^n\right), i = -1/2, 1/2 \tag{3.100}$$

There are four unknown coefficients for each of the five update equations in (3.99) and (3.100). In [81], the method to find the unknown coefficients involves the use of fictitious points and solving the resultant algebraic equations. Alternatively, a more straightforward approach, which is originally proposed for Yee's algorithm in [82] - [84], can be generalized to optimize the general four-point stencil. Unlike the treatment for Yee's algorithm, two types of interface conditions can be derived for the fourth-order stencil.

3.7.1.1. *Condition 1*

As an example, let us consider the update equation for the E-field at $i = 0$. Replacing the E- and H-fields in (3.99) by the exact solutions in (3.92) and (3.93) at a design frequency f_0 and equating the real and imaginary parts, we obtain two equations with four unknowns (C_1, C_2, C_3, C_4). By forcing $C_1 = 1/24$ and $C_2 = -27/24$ (i.e., the coefficients for the regular fourth-order stencil), the unknowns reduce to two (C_3, C_4). The resultant equations can be rewritten in the matrix form as

$$\begin{bmatrix} a_{11} & a_{12} \\ a_{21} & a_{22} \end{bmatrix} \cdot \begin{bmatrix} C_3 \\ C_4 \end{bmatrix} = \begin{bmatrix} b_1 \\ b_2 \end{bmatrix} \tag{3.101}$$

where

$$\begin{aligned}
a_{11} &= \frac{24(1+\Gamma)\cos(k_2\Delta z/2)}{\eta_2}, a_{12} = \frac{24(1+\Gamma)\cos(3k_2\Delta z/2)}{\eta_2}, \\
a_{21} &= -\frac{24(1+\Gamma)\sin(k_2\Delta z/2)}{\eta_2}, a_{22} = -\frac{24(1+\Gamma)\sin(3k_2\Delta z/2)}{\eta_2}, \\
b_1 &= \frac{(1-\Gamma)[27\cos(k_1\Delta z/2) - \cos(3k_1\Delta z/2)]}{\eta_1}, \\
b_2 &= -\frac{48(1+\Gamma)\epsilon\Delta z\sin(\omega\Delta t/2)}{\Delta t} \\
&+ \frac{(1-\Gamma)[27\cos(k_1\Delta z/2) - \cos(3k_1\Delta z/2)]}{\eta_1}
\end{aligned} \tag{3.102}$$

are constants. The values of C_3, C_4 can be determined by solving (3.101). The other four sets of unknown coefficients for $i = \pm 1, \pm 1/2$ can be found using a similar approach. In the rest of the report, the scheme using these coefficients is referred to as *Condition 1*.

3.7.1.2. *Condition 2*

Note that the general stencil of (3.98) allows a total of four free coefficients. However, in Condition 1, only two of them were used. To take advantage of the extra two degrees of freedom, we can introduce a second design frequency f_0'. By doing this, we can also expect to obtain a more broad-band scheme. Again, let us consider the update equation for the E-field at $i = 0$. Substituting the exact solution into (3.92) and (3.93) for two design frequencies f_0, f_0' into (3.99), and equating the real and imaginary parts, yields the matrix equation

$$\begin{bmatrix} a_{11} & a_{12} & a_{13} & a_{14} \\ a_{21} & a_{22} & a_{23} & a_{24} \\ a'_{11} & a'_{12} & a'_{13} & a'_{14} \\ a'_{21} & a'_{22} & a_{23} & a'_{24} \end{bmatrix} \cdot \begin{bmatrix} C_1 \\ C_2 \\ C_3 \\ C_4 \end{bmatrix} = \begin{bmatrix} b_1 \\ b_2 \\ b'_1 \\ b'_2 \end{bmatrix} \tag{3.103}$$

where

$$\begin{aligned}
a_{11} &= \frac{(1-\Gamma)\cos(3k_1\Delta z/2)}{\eta_1}, a_{12} = \frac{(1-\Gamma)\cos(k_1\Delta z/2)}{\eta_1} \\
a_{13} &= \frac{(1+\Gamma)\cos(k_2\Delta z/2)}{\eta_2}, a_{14} = \frac{(1+\Gamma)\cos(3k_2\Delta z/2)}{\eta_2} \\
a_{21} &= \frac{(1-\Gamma)\sin(3k_1\Delta z/2)}{\eta_1}, a_{22} = \frac{(1-\Gamma)\sin(k_1\Delta z/2)}{\eta_1} \\
a_{23} &= -\frac{(1+\Gamma)\sin(k_2\Delta z/2)}{\eta_2}, a_{24} = -\frac{(1+\Gamma)\sin(3k_2\Delta z/2)}{\eta_2} \\
b_1 &= 0, b_2 = -\frac{2\Delta z\epsilon(1+\Gamma)\sin(\omega\Delta t/2)}{\Delta t}
\end{aligned}$$

are constants corresponding to the first design frequency f_0. The matrix elements $a'_{i,j}$ and $b'_{i,j}$ have similar expressions as $a_{i,j}$ and $b_{i,j}$ except that ω, k_1, k_2 are replaced by ω', k'_1, k'_2 corresponding to the second design frequency f'_0. The values of C_1, C_2, C_3, C_4 can be determined by solving (3.103). The other four sets of unknown coefficients can be determined similarly. The scheme using these coefficients is referred to as *Condition 2*.

3.7.2. Numerical Simulations

A classical problem [77], [81], a one-dimensional partially-filled dielectric cavity as shown in Fig. 3.59, is used to evaluate the aforementioned interface conditions. In Fig. 3.59, N (even number) is the total number of cells used to mesh the cavity. By enforcing the corresponding boundary conditions at the PEC and dielectric interfaces, the closed form solutions for the E- and H-fields can be readily derived [2] and written as

$$E(z) = \begin{cases} \sin(k_1 z), & 0 \le z \le 1 \\ C\cos(k_2 z) + D\sin(k_2 z), & 1 < z \le 2 \end{cases} \tag{3.104}$$

$$H(z) = \begin{cases} \frac{k_1}{j\omega\mu_0}\cos(k_1 z), & 0 \le z \le 1 \\ -\frac{k_2 C}{j\omega\mu_0}\sin(k_2 z) + \frac{k_2 D}{j\omega\mu_0}\sin(k_2 z), & 1 < z \le 2 \end{cases} \tag{3.105}$$

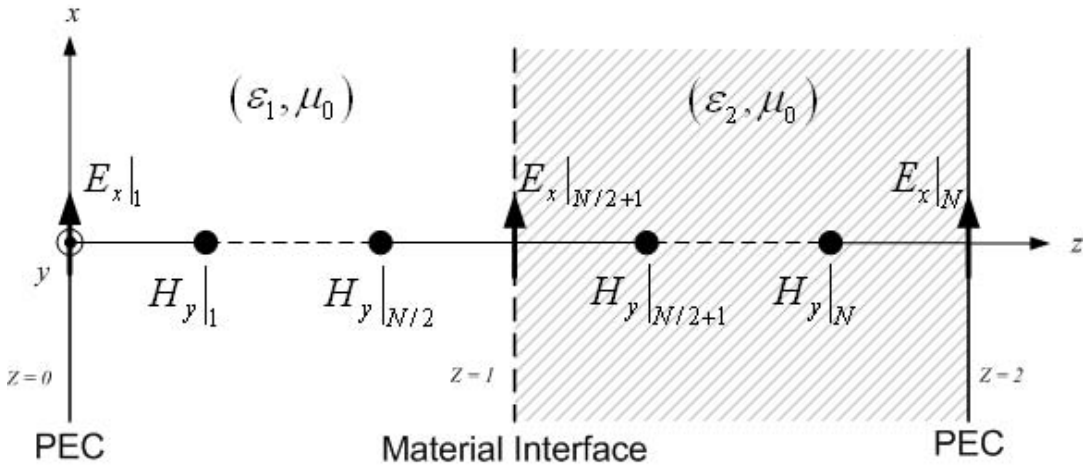

Fig. 3.59. One-dimensional partially-filled cavity.

where

$$C = 2\sin(k_1)\cos(k_2), D = -\frac{\sin(k_1)\cos(2k_2)}{\sin(k_2)}$$

Assuming that $\epsilon_{r1} = 1$ and $\epsilon_{r2} = 2.25$, one of the resonant frequencies is 242.0138 MHz. This frequency will be used in all of the simulations.

The regular FDTD(2,4) [15] or the NS24 [91] schemes will be applied to the update equations in the homogeneous regions. Near the material interface, Condition 1 or 2 will be enforced. The PEC boundaries are modeled using image theory. The only differences between the regular stencils and the interface conditions are the coefficients. Consequently, similar fourth-order stencils, with different coefficients, can be consistently applied throughout the domain. The coefficients for the interface conditions will be calculated once, using (3.101) or (3.103), before the time loop starts. To measure the accuracy, the L^2 error is defined as [85]

$$\|E\|_2 = \sqrt{\Delta z \sum_{i=0}^{N} (\tilde{U}_i - U_i)^2} \tag{3.106}$$

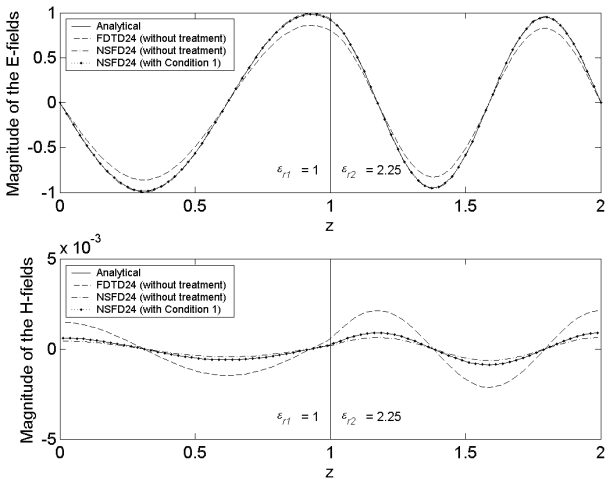

Fig. 3.60. The snapshot of the E- and H-fields for $N_0 = 80$.

where $\tilde{U}_i$ represents the numerical E- and H-fields predicted by FDTD; U_i designates the exact solution given by (3.104) and (3.105).

In the first example, we initially consider *Condition 1*. Since Condition 1 is derived for a single frequency, NS24 will be applied in the homogeneous region to minimize dispersion. In the simulation, the design number of cells and the Courant number are set to be $N_0 = 80$ and $S = 0.85$, respectively. The total number of time steps for different N is $2048(N/24)$. Snapshots of the E- and H-fields for $N_0 = 80$ are plotted in Fig. 3.60. It is evident that the NS24 scheme with Condition 1 predicts almost the exact solution. The L^2 error of the E-field versus N, with and without Condition 1 near the material interface, are plotted in Fig. 3.61. As shown, at $N = N_0$ the error generated by NS24 scheme with Condition 1 is extremely small. However, the error increases rapidly as N deviates from N_0.

As a second example, *Condition 2* is considered. To evaluate the broad-band performance, the standard FDTD(2,4) is used throughout the homogeneous region. Indeed, the update coefficients for Condition 2 are weak functions of the design number of cells N_0,N_0'. In other words, varying N_0 and N_0' will not alter the coefficients significantly. In the following, N_0 and N_0' will be set to 320 and 1×10^6, respectively. To demonstrate the order of accuracy in the entire space domain, a very small Courant number $S = 0.01$ is used. The L^2 error of the E-field versus N, with and without Condition 2, are plotted in Fig. 3.62. As shown, due to the error generated near the material interface, FDTD(2,4) without the interface treatment exhibits only second-order accuracy. However, fourth-order accuracy is fully restored if Condition 2 is applied near the interface.

In summary, two dielectric interface conditions are designed for the four-point space stencils. *Condition 1* is almost exact at the design frequency. However, this ideal performance is very narrow band. *Condition 2* generates a real fourth-order scheme in the space domain. However, a very small Courant number has to be used to achieve the fourth-order. An alternative approach is to use a fourth-order discretization, for example RK4 [85], in the time domain.

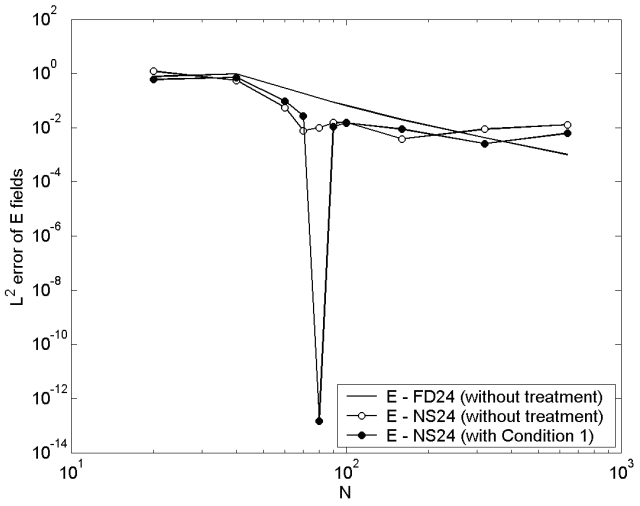

Fig. 3.61. L^2 error of the E-fields (Condition 1).

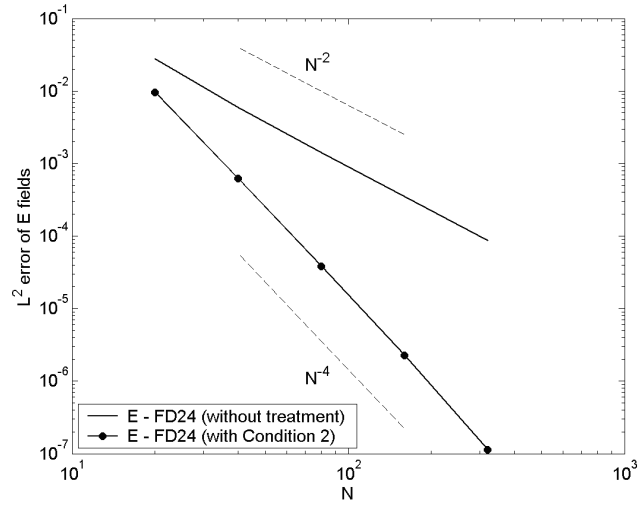

Fig. 3.62. L^2 error of the E-fields (Condition 2).

CHAPTER 4

THE EFFECTS OF PASSENGERS ON PED MUTUAL COUPLING

An important EMI issue for commercial aircraft is the possibility of interference generated by on-board personal electronic devices (PEDs), such as cell phones, CD players, laptop computers, etc. "It is a common policy of all commercial airlines to prohibit the use of PEDs during at least the very sensitive phases of take-off and landing, if not for the entire duration of the flights. The policy has been established because it is believed that radiated emissions from PEDs can interfere with the aircraft electronic equipment, i.e., jamming in the communication systems" [72], [76].

In Georgakopoulos, *et al*, the mutual coupling between a simulated PED, located in the cabin area of a simplified scale model aircraft fuselage, and an antenna mounted on the exterior of the fuselage was predicted using the FDTD and compared with measurements [72], [76]. This work, however, was performed for a completely empty fuselage. An airline fuselage is of course highly populated with various structures: metal frames, foam seat cushions, duct work, wires, various plastics, insulating and decorative materials, etc. An ideal model would include all of these geometrical details and material properties, but the complexity and computational resources involved in such an undertaking renders it impractical. Some of these structures can be neglected. Surprisingly, it has been reported that the seat cushions and even their metal frames have a negligible impact on the coupling of such antennas [96]. Passengers, on the other hand, are a class of structures which have a high probability of modifying the EMI environment found within the perforated metallic cavity of an aircraft fuselage due to their dispersive and lossy constituent materials. Modeling the enormous complexity of the human body, particularly using uniform discretization

across a solution space on the scale of an airliner, is also prohibitive. Instead, the low-order approximate passenger modeled here is represented by a geometrically simple shape composed of a single bulk material.

In this chapter, the *S*-parameters of a simulated PED located within a scaled fuselage-like enclosure and an antenna mounted on the exterior of this enclosure are both measured and computed using the FDTD method [1], [6]. The *S*-parameters are determined for the case in which the enclosure is populated with simplified "passengers," and compared with those for the case of the empty enclosure.

4.1. Geometry

The "Simplified Fuselage" is an aluminum box having a rectangular cross section that would enclose the fuselage of a 1:20 scaled Boeing 757. Although individually larger than their scaled counterparts, the cabin windows have approximately the same aperture area per unit length as those of a scaled 757, and the Simplified Fuselage has a large aperture at one end to represent the cockpit windows. To ease fabrication and handling, the overall length of the Simplified Fuselage is 75% that of a scaled 757. Additional dimensional details can be found in [72], [76]. The image in Fig. 4.1 is of the CAD model for the empty Simplified Fuselage, from which the relative locations of the simulated PED and the external antenna can be discerned.

The structure of the human body is extremely complex, and consists of a variety of dispersive and lossy materials [1], [11], [97]. Modeling all the details of the human body is beyond the scope of this work. However, approximately 70% by weight of the human body is blood which has salinity close to 0.9% (grams/liter). Therefore, circular-cross-section plastic

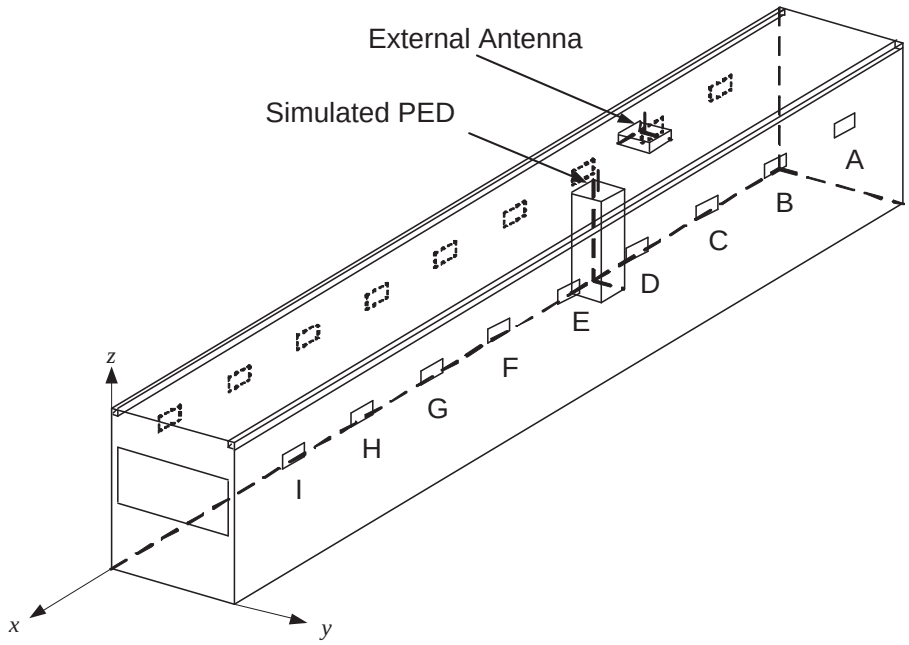

Fig. 4.1. Geometry of the empty Simplified Fuselage (the letters denote the locations of the cabin windows).

tubes containing 0.9% salt water were used to simulate the passengers. As illustrated in Figs. 4.2 and 4.3, there are 6 passengers on every row, and 15 rows (90 passengers in total) inside the fuselage. The distance between the adjacent rows is 75 mm.

4.2. Measurements

To provide experimental data with which to compare to the FDTD simulations, measurements were made of the coupling between the simulated PED and the external antenna. These measurements were made with the Simplified Fuselage empty, and with the passengers in place.

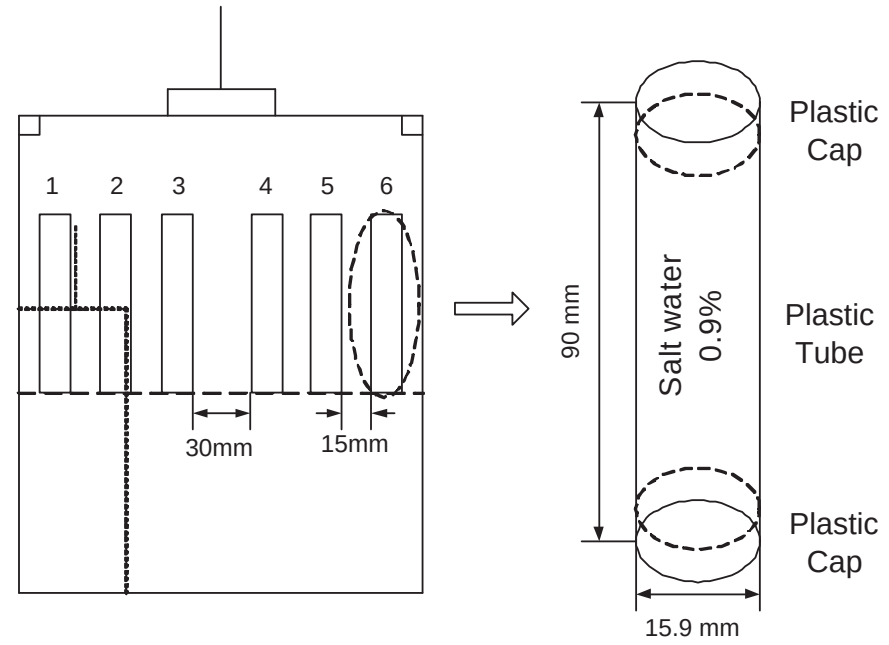

Fig. 4.2. Cross section of the Simplified Fuselage illustrating the geometrical relationships between the simulated PED, the exterior antenna, and the simulated passengers.

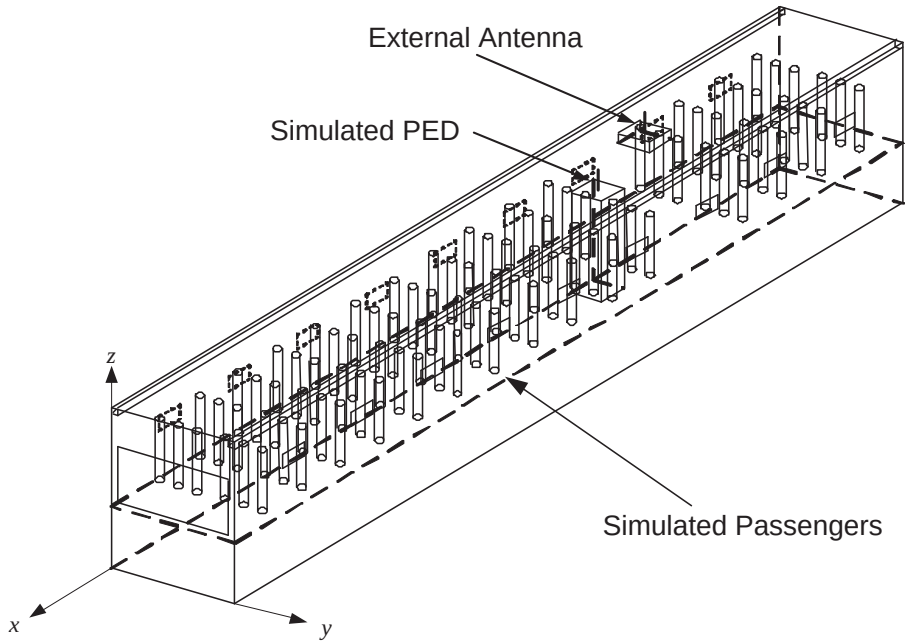

Fig. 4.3. Geometry of the Simplified Fuselage filled with 90 passengers.

4.2.1. Passengers

The low-order approximation to scaled passengers consists of 90 mm long, 15.9 mm diameter thin-walled "propionate" plastic tubing filled with 0.9% salt water. Top and bottom plug caps were used to close the tubes. A small hole was drilled through each of the top caps to allow the air displaced as the cap was installed to escape.

To keep the passengers in their designated locations and upright, an expanded polystyrene support system was made. In a sheet of 1" thick polystyrene, holes were cut according to the FDTD model with the help of a wood template, as shown in Fig. 4.4. A circular brass tube with its edge sharpened was used to cut the holes into which the passengers were placed. To keep the passengers from falling through, a second layer of expanded polystyrene was placed beneath the first. Finally, expanded polystyrene spacers were used beneath the support system to place the passengers at the designed height within the Simplified Fuselage. The complete set of 90 passengers and their support system is shown in Fig. 4.5.

The permittivity and loss tangent of the saline solution was measured using Hewlett-Packard's open-ended coaxial Dielectric Probe [98]. The measurement setup is shown in Fig. 4.6. The measured permittivity and effective conductivity of the 0.9% salt water at $20°C$ are plotted in Figs. 4.7 and 4.8, respectively.

4.2.2. Measurement Setup

The experimental setup is essentially identical to that for the PED measurements previously reported [72], [76]. A detailed description of the setup and measurements follows.

The measurements were made in the anechoic chamber to preclude the possibility

Fig. 4.4. A top view photograph of the expanded polystyrene passenger support, and the wood template and brass tube used to cut the holes.

Fig. 4.5. A photograph of the 90 passengers in their support structures.

Fig. 4.6. The setup for the measurements of the permittivity and conductivity of the 0.9% salty water.

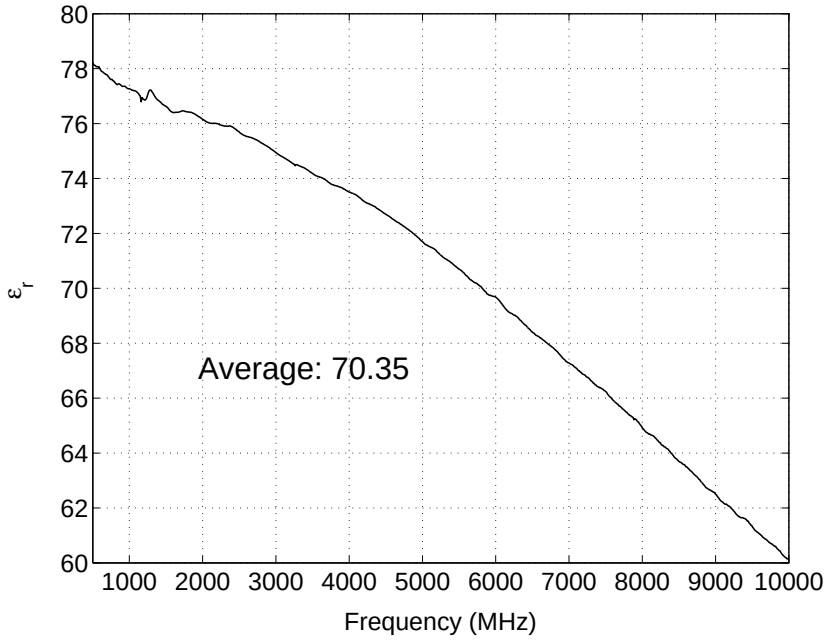

Fig. 4.7. Measured permittivity of the 0.9% salt water at $20°C$.

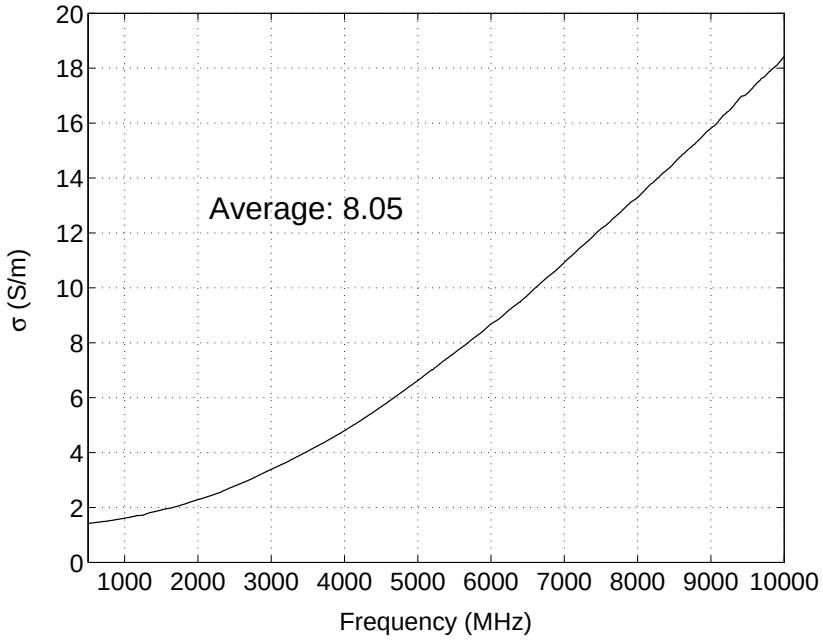

Fig. 4.8. Measured effective conductivity of the 0.9% salt water at $20°C$.

Fig. 4.9. An end-view photograph of the Simplified Fuselage, setup in the anechoic chamber with the instrumentation beneath it. The front panel had not yet been copper taped to the fuselage, revealing the simulated passengers and their expanded polystyrene supports.

of environmental scattering. The Simplified Fuselage was placed near the center of the chamber, and was supported approximately 84 cm (33 inch) above the floor with blocks of expanded polystyrene. The only significance of this height is that it was convenient for placing the synthesizer and S-parameter test set of the network analyzer beneath the model, thus minimizing the lengths of the RF cables. Carbon-loaded foam absorber was placed on the instrumentation to reduce any scattering that might occur. A 15 m (50-foot)-long IEEE-488 cable enabled the HP8510 processor to communicate with the source and test set, and a 12 m (40-foot)-long IF cable plumbed the measured results to the HP8510 detector, located outside of the chamber. A photograph of the setup within the anechoic chamber is shown in Fig. 4.9.

One of the RF cables passed through a hole in the fuselage floor and into the hollow pedestal on which the monopole (which simulates the PED) was mounted. A 51 cm (20 inches) long "Gold Tipped" Addams-Russell precision cable was used here to capitalize on its interchangeable interface. A female APC-3.5 connector was used to measure the "Thru" standards of the full 2-port calibration. The female connector was removed and replaced with a phase-matched male APC-3.5 connector with which the other calibration standards and the S-parameters were measured.

A 1.5 m (5-foot)-long braided cable that had been wrapped with ferrite-loaded elastomeric absorbing material was used to connect the external monopole to the other port of the test set.

4.2.3. Calibration and Measurement Parameters

Extremely rapid amplitude variations occur as a function of frequency in S_{12} between the PED and the external antenna due to the reverberations within the fuselage. However, the maximum number of frequency points that can be measured in one sweep with the network analyzer is 801. This is insufficient to accurately sample these frequency response variations over the desired band of 50 MHz to 6 GHz. To increase the sampling density, six bands of 801 frequency points were measured. The first band ranged from 50 MHz to 1.0 GHz, the remaining bands were each 1.0 GHz wide.

In order to measure the error-corrected S-parameters at multiple frequency bands, a calibration had to be performed for each of the frequency bands. A standard open/short/load "full 2-port" calibration (with the Isolation standard omitted) was performed at each frequency band. Since the HP8510 does not have sufficient memory to store all of the correc-

tion coefficients, the six 801-frequency calibration sets were stored on 3.5" floppy disks and loaded and deleted from the network analyzer memory as needed.

The other instrumentation parameters of note are: the source was operated in "Step Frequency Mode" (the oscillator was phase locked at each frequency), the source power was +10 dBm, 512 IF averages were used for the high-signal calibration standards and 1,024 IF averages were used for the low-signal calibration standards and for the measurements. Over the first frequency band at which the amplitude of S_{12} is lowest, an IF averaging factor of 2,048 was used. Good measurement practices were employed: the connectors of the DUT, calibration standards, instruments, and RF cables were cleaned; RF connections were torqued to 8 in-lb; and more than sufficient time was allowed to elapse with the instrumentation turned on and with the DUT in place to ensure thermal stability

4.2.4. Measurement Results

The measured S-parameters of the fuselage with and without passengers are shown in Figs. 4.10 - 4.12. Because the system is reciprocal ($S_{12} = S_{21}$), only S_{12} is plotted.

From Figs. 4.10 - 4.12, it is evident that the presence of the passengers has a negligible impact on S_{11} (the two curves are indistinguishable), which is the reflection coefficient of the exterior antenna. However, the passengers did have a significant effect on S_{22} and S_{12}. As shown, S_{22} (the interior antenna) and S_{12} without passengers exhibit much more oscillatory behavior due to the large number of resonances present inside the fuselage. However, S_{22} and S_{12} with the passengers exhibit much smoother distributions since many resonant components have been significantly dampened by the "human bodies" which are highly dielectric and lossy. Due to this phenomenon, the presence of the passengers has

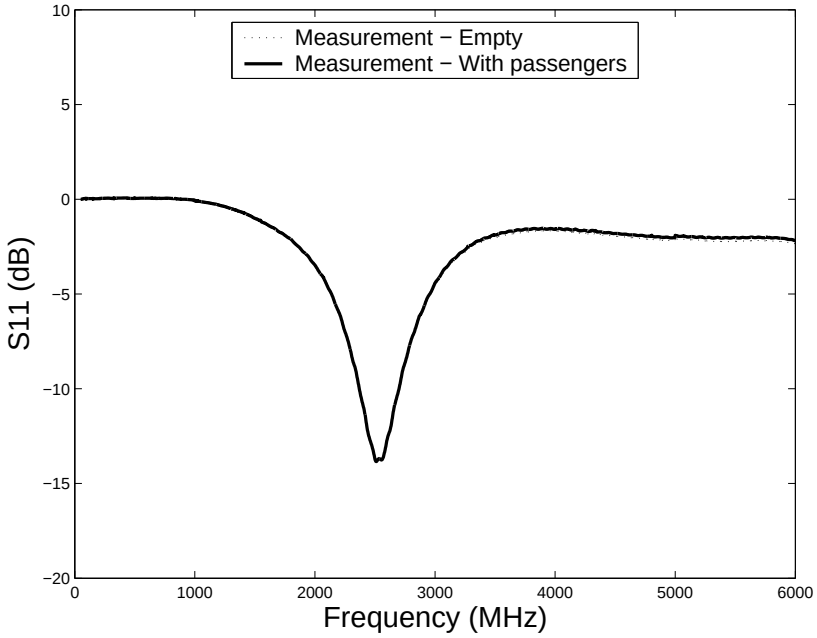

Fig. 4.10. Measured S_{11} (the exterior antenna) of the simplified fuselage with and without passengers.

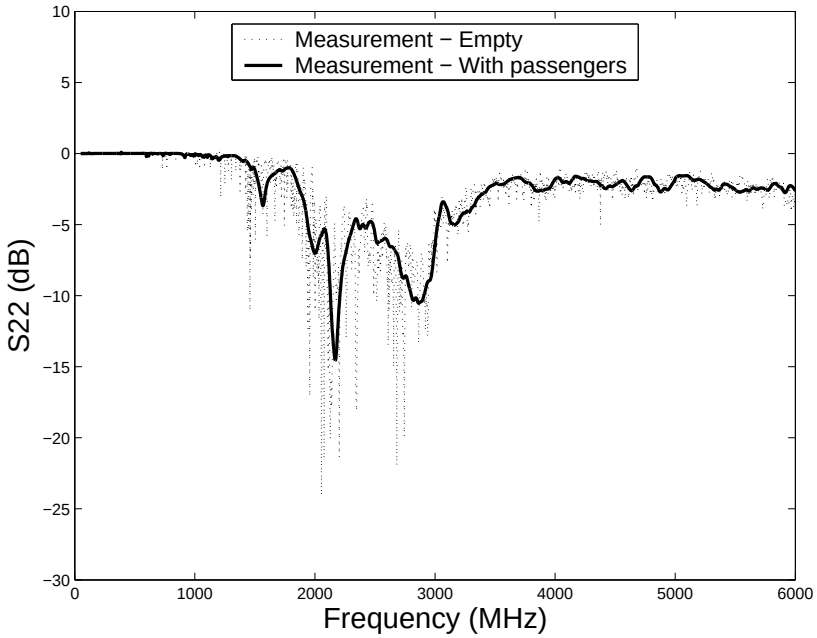

Fig. 4.11. Measured S_{22} (the interior antenna) of the simplified fuselage with and without passengers.

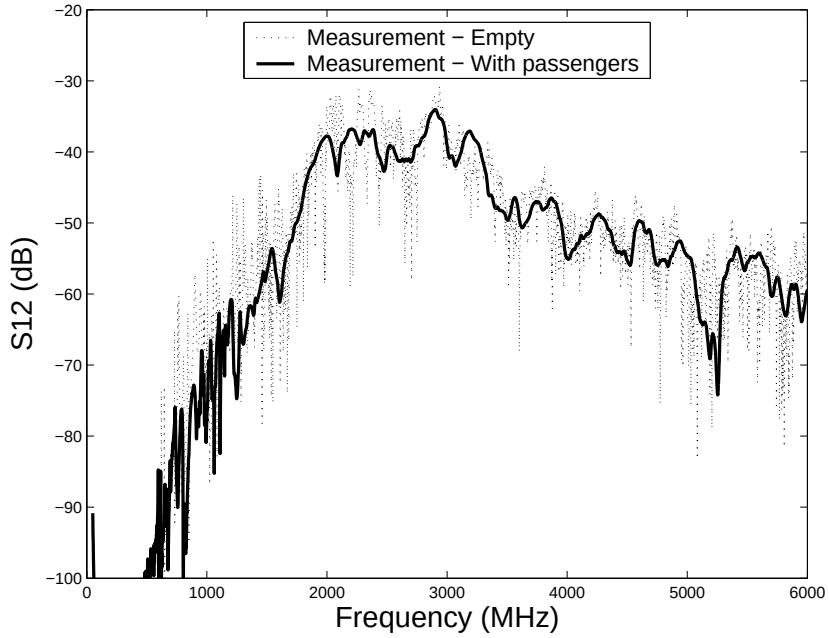

Fig. 4.12. Measured S_{12} of the simplified fuselage with and without passengers.

the effect of slightly reducing the possibility of aircraft system upset by PED emissions as compared to that of the empty fuselage.

4.3. Simulations

The mutual coupling between the internal PED antenna and the antenna mounted on the exterior of the fuselage was simulated using the FDTD algorithm [1], [6]. The S-parameters were computed following the procedure described in [8].

Due to the very large permittivity values of the salt water, a finer mesh size than that used for the case of the empty fuselage was necessary. Therefore, a cell size of $\Delta x = \Delta y = \Delta z = 2.5mm$ ($\lambda/40$ at 3 GHz in free space or about $\lambda/5$ at 3 GHz in the salt water) was used. To allow the excitation pulse to decay to a low level, the simulation was executed for 60,000 time steps.

From the numerical experiments, it has been found that the coupling results are not very sensitive to variations in the passengers' permittivity and conductivity. To demonstrate this, S_{12} values were computed for three different combinations, e.g.: the low-frequency parameters ($\epsilon_r = 78.22, \sigma = 1.42$S/m) at 500 MHz, the high-frequency parameters at ($\epsilon_r = 60.12, \sigma = 18.43$S/m) 10,000 MHz, and the average parameters ($\epsilon_r = 70.35, \sigma = 8.05$S/m).The S_{12}s computed using these three different sets of parameters are plotted for the frequency band of 1,500 MHz to 2,500 MHz in Fig. 4.13 and for the frequency band of 4,500 MHz to 5,500 MHz in Fig. 4.14.

As shown, the simulated results using different parameters agree to each other very well regardless of the dispersive characteristic of the salt water. That the direct path through window C likely accounts for the majority of the coupling of energy from the PED to the exterior antenna probably explains this insensitivity in S_12 to the parameters of the passengers. Based upon this observation, it can be justified that, for this particular configuration, a complete dispersive modeling of the salt water is not necessary. Hence, the average permittivity and conductivity values (70.35 and 8.05 S/m) were used for the rest of this paper.

The time snapshots of the E_z fields in various cross-section planes are plotted in Fig. 4.17 - 4.18. The brightness of the plot increases with the magnitude of the E_z field. Clearly, the E fields subject significant damping inside the "passenger bodies". Also notice the strong E fields radiated through Window C in Fig. 4.18.

Moreover, the time history of an E_z field in the free-space region inside the fuselage is plotted in Fig. 4.19. The E_z field at the same position for the empty case is also plotted in Fig. 4.19 as a comparison. It is evident that magnitude of the E_z field with

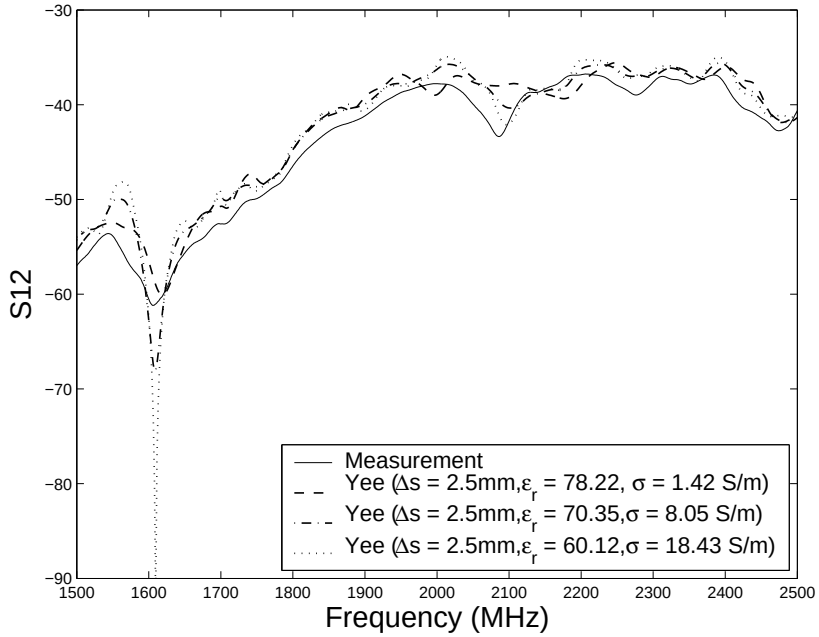

Fig. 4.13. Simulated S_{12} using different electric property combinations (1500 - 2500 MHz).

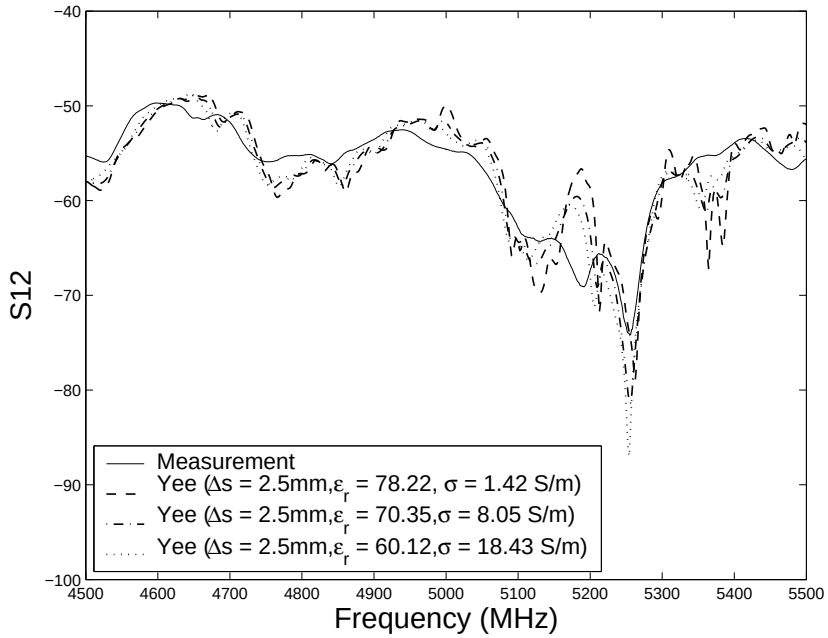

Fig. 4.14. Simulated S_{12} using different electric property combinations (4500 - 5500 MHz).

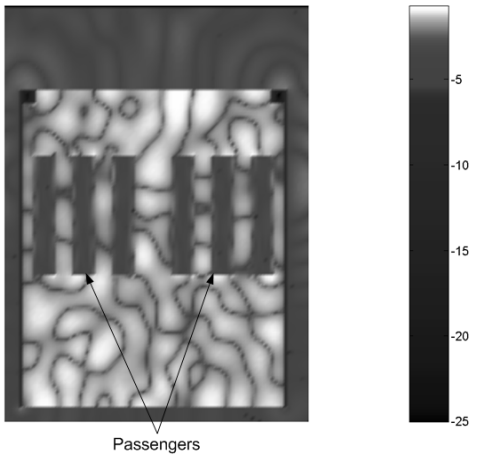

Fig. 4.15. Logarithmic plot of the E_z field on the yz-plane (front view) across one row of passengers.

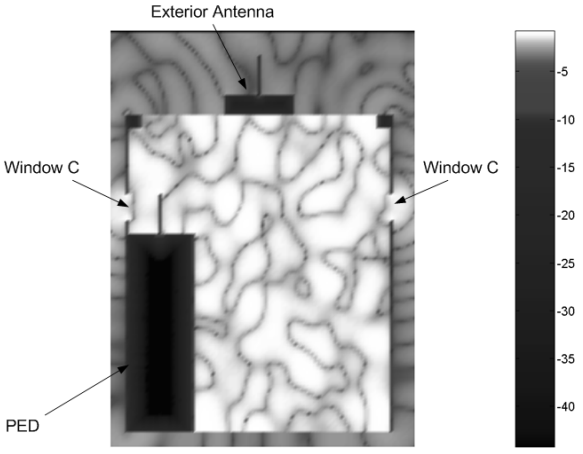

Fig. 4.16. Logarithmic plot of the E_z field on the yz-plane (front view) at the center of Window C.

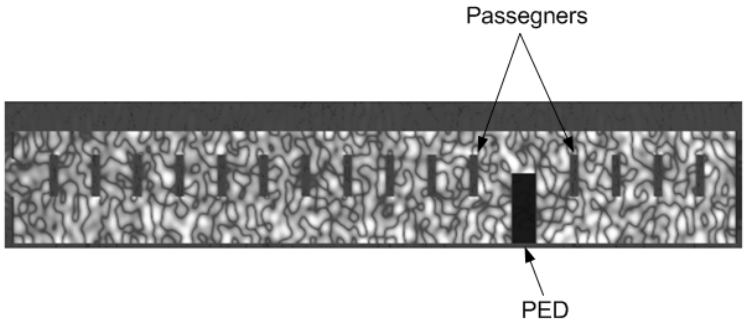

Fig. 4.17. Logarithmic plot of the E_z field on the xz-plane (side view) across one column of passengers.

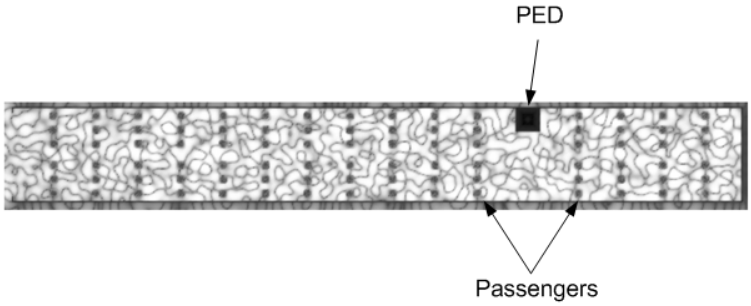

Fig. 4.18. Logarithmic plot of the E_z field on an xy-plane (top view) at the fuselage center in the y direction.

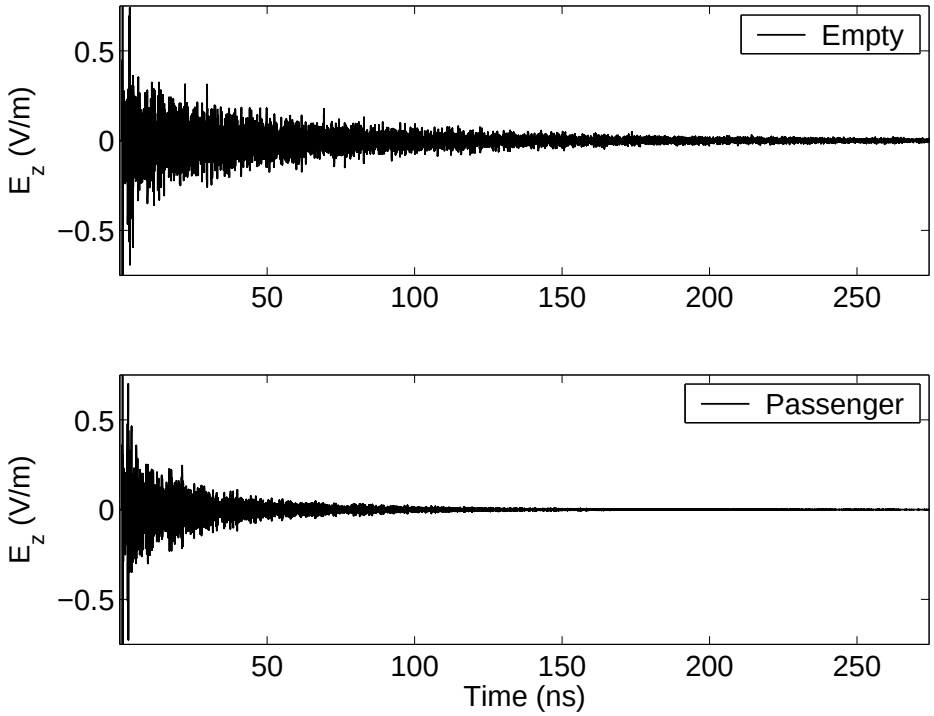

Fig. 4.19. Representative time history of the E_z field inside the fuselage with and without the passengers.

passenger presented decay much faster than that without, due to the heavy damping inside the passenger.

The measured and simulated S-parameters with the passengers are plotted in Figs. 4.20 - 4.22. As shown, S_{11}, which is essentially just the reflection coefficient of a monopole, has a null at 2500 MHz. The null of FDTD simulated result is shifted to a lower frequency by about 100 MHz. However, S_{22}, which is the reflection coefficient of the internal antenna, exhibits a similar trend as that of S_{11} but with more oscillations due to the fuselage's highly resonant characteristic.

Of the S-parameters, S_{12} is the most important since it represents the energy generated by the PED which could interfere with the aircraft's communication system. To better

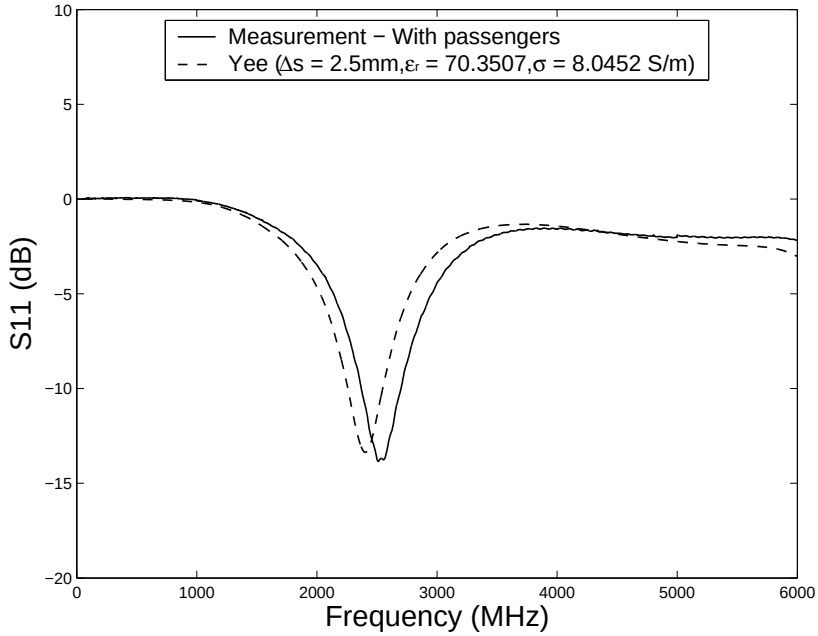

Fig. 4.20. Measured and simulated S_{11} of the simplified fuselage filled with passengers.

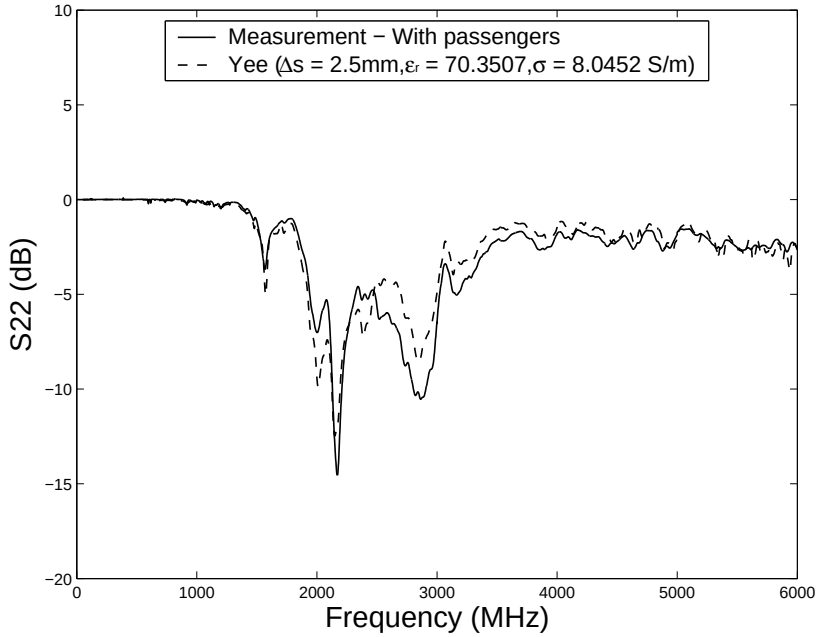

Fig. 4.21. Measured and simulated S_{22} of the simplified fuselage filled with passengers.

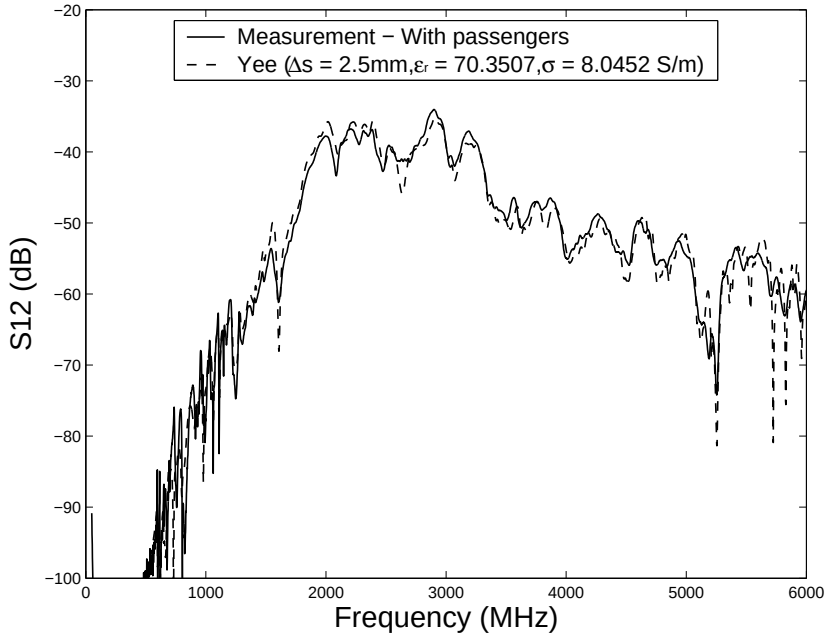

Fig. 4.22. Measured and simulated S_{12} of the simplified fuselage filled with passengers.

illustrate the variation of S_{12}, Fig. 4.22 is expanded in different frequency bands, as shown in Figs. 4.23 - 4.26. Very good agreement is observed from 1,500 MHz to 5,500 MHz. The discrepancy near the lower frequencies is probably due to the extremely low coupling level. However, the discrepancy at the high end of the frequency band can be attributed to the large dispersion error caused by very discretization. Moreover, it is important to note that the maximum coupling level, which is higher than -40 dB, occurs between 2.0 - 3.5 GHz. This level of coupling is sufficiently high to draw the attention of the communication system designers.

4.4. Conclusion

In summary, the effects of passengers on the mutual coupling between a simulated PED and an externally-mounted antenna were investigated. By comparing the S-parameters for

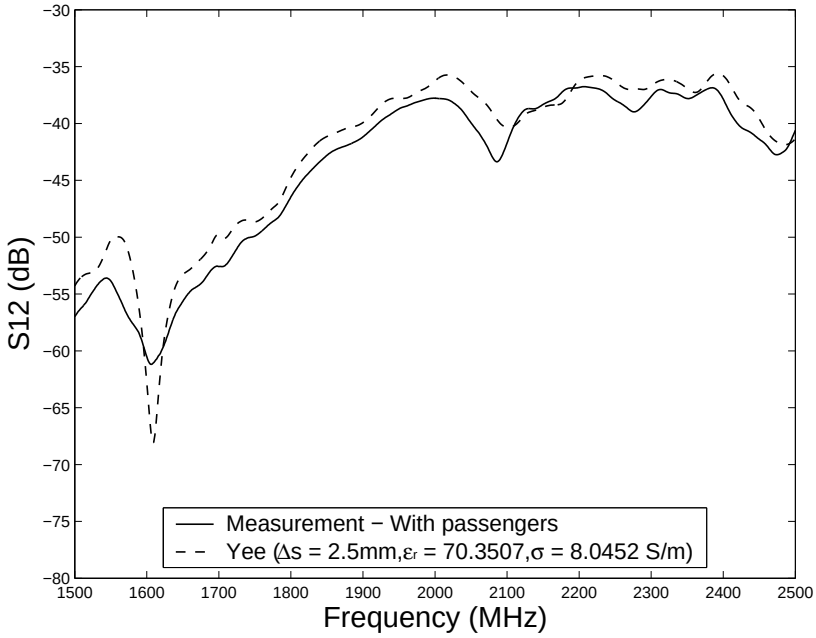

Fig. 4.23. Measured and simulated S_{12} of the Simplified Fuselage filled with passengers (1500 - 2500 MHz).

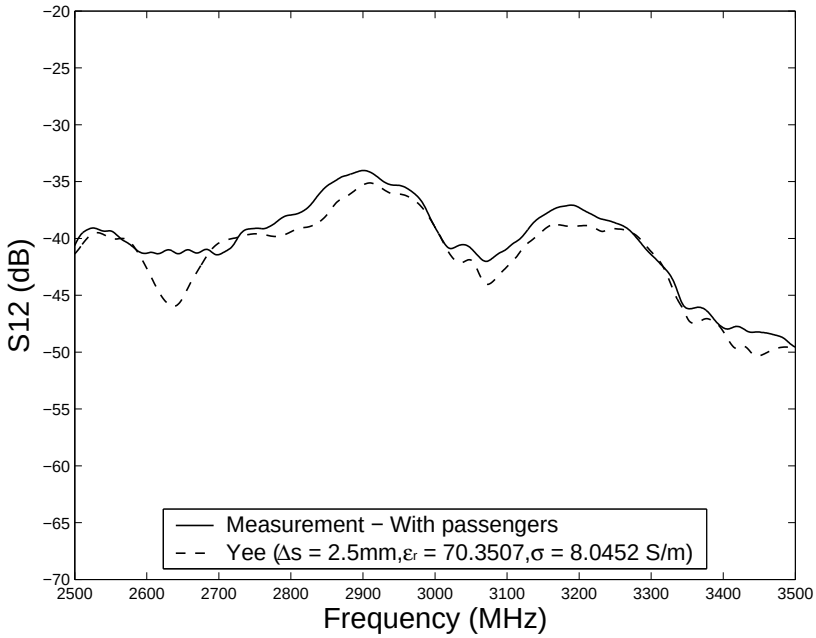

Fig. 4.24. Measured and simulated S_{12} of the Simplified Fuselage filled with passengers (2500 - 3500 MHz).

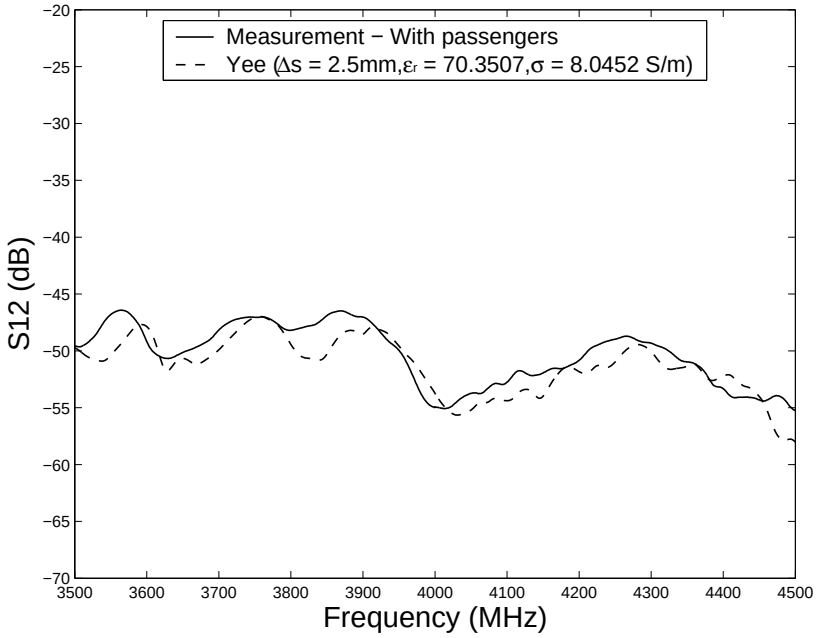

Fig. 4.25. Measured and simulated S_{12} of the Simplified Fuselage filled with passengers (3500 - 4500 MHz).

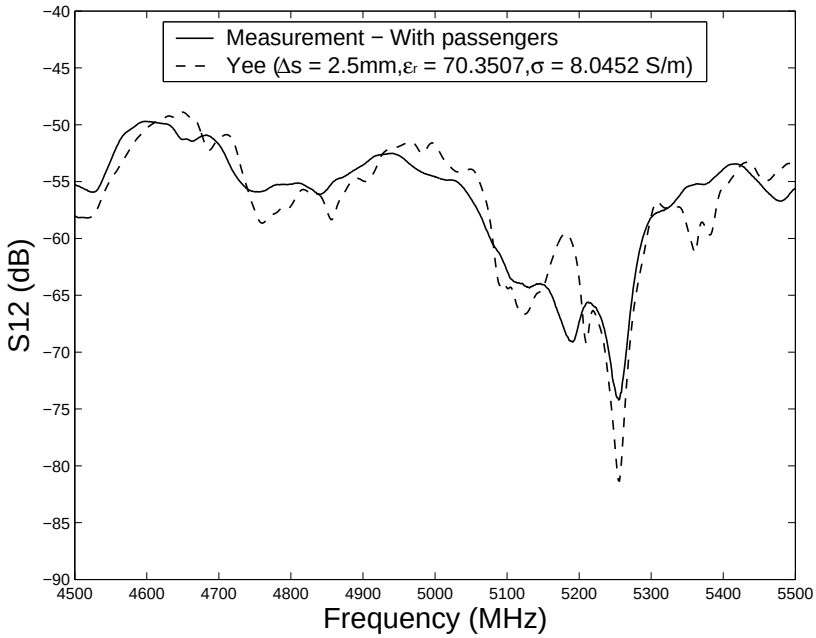

Fig. 4.26. Measured and simulated S_{12} of the Simplified Fuselage filled with passengers (4500 - 5500 MHz).

the empty scale model fuselage with those for the case in which the scale model is populated with 90 bodies which simulated human passengers, it was found that the presence of passengers significantly dampens the reverberations that occur within the fuselage. This dampening effect reduces the magnitude of the coupling over most of the frequencies considered, and by up to approximately 15 dB. The reduced threat indicated with passengers present, potentially represents a relaxation in the EMI shielding required for on-board systems compared to that indicated by predicted and measured S-parameters for the empty fuselage case.

CHAPTER 5

SUMMARY, CONCLUSIONS AND FUTURE WORK

The major objective of the research presented in this project was to develop low-dispersion finite-difference time-domain (FDTD) methods. In particular, such methods are of great interests in many practical applications which contain electrically large objects and/or require very long simulation time. The currently standard FDTD method, Yee's algorithm, is only second-order accurate in both the space- and time- domains which suffers from serious dispersion. However, Yee's algorithm is robust and very easy to implement. Over the years, numerous practical problems have been successfully simulated using Yee's algorithm. Therefore, to take advantage of the available geometry library, the ideal method should be able to minimize the dispersion errors without significant modifications based on Yee's algorithm.

5.1. Summary and Conclusions

In Chapter 1, the issues caused by the electrically large problems and the difficulties for Yee's algorithm were described. It was indicated that the mesh refinement is not a very efficient way of reducing dispersion. Thus, the severe dispersion accumulation of Yee's algorithm greatly restricts the electrical size of the structures that can be handled. Based on a selective survey of the existing literature, the existing dispersion-reduction FDTD methods can be roughly classified into two categories: the standard (SFD) and the nonstandard (NSFD) FDTD methods. The SFD methods use the standard central difference stencils which are derived from the Taylor series expansion by minimizing the leading truncation

error. To further reduce dispersion, the NSFD methods adjust the coefficients of the SFD stencils directly based on the dispersion analysis.

Chapter 2 introduced the fundamental theories of the SFD methods. The governing equations of any electromagnetic phenomena, Maxwell's equations was first reviewed. Then, the procedure to derive Yee's FDTD(2,2) algorithm was demonstrated. That is, the $E-$ and $H-$ fields are staggered in both the time- and space domains. Then, the time- and space- derivatives in Maxwell's equations are directly approximated by the second-order central difference stencil. To improve the accuracy, it is natural to consider the usage of the higher-order finite difference stencils. For simplicity, the higher-order stencils were only used in the space domain which constructs the FDTD(2,N) schemes. The approach to derive the higher-order stencil, the method of undetermined coefficients, was demonstrated for the FDTD(2,4) algorithm. Then, the procedure was generalized for central difference stencils with arbitrary high order. It was indicated that the highest order-of-accuracy that can be achieved increases with the number of points involved in the stencil. Next, the stability conditions of the SFD methods were also briefly discussed. Finally, the dispersion characteristics of the SFD methods were quantitatively studied. Based on the dispersion analysis, it is clear that the dispersion is determined by the space and time increments, the operating frequency, and the propagation angles. Using the higher-order stencils does help to reduce the dispersion errors. It was also observed that the local dispersion curve of a SFD method is centered about its own average value. Moreover, for the FDTD(2,N) scheme, the ideal N-order cannot be achieved due to the larger errors generated in the time domain. These observations can be exploited to further reduce the dispersion.

In Chapter 3, the major topic of this project, the NSFD methods, were presented.

The discussion started with the fundamental theory of the NSFD algorithm. It was shown that the regular NSFD algorithm was constructed by simply replacing the time and space increments in Yee's scheme by their frequency-optimized counterparts. The 1D NS22 scheme was first introduced followed by a detailed dispersion analysis. A few numerical simulations were provided to verify the performance of the 1D NS22 scheme. It was observed that the NS22 scheme is a narrow-band scheme in terms of dispersion, which is very suitable for single-frequency simulations. The dispersion null can be flexibly controlled by a design mesh resolution. For broad-band signals, the 1D NS22 scheme could predict results no worse than Yee's algorithm as long as the design mesh resolution is properly selected. Then, the basic concept of the NSFD was extended to the four-point stencil to create an NS24 scheme. Dispersion analysis revealed that the NS24 scheme possesses two dispersion nulls of which one controlled by the design mesh resolution and the other is controlled by the Courant number. With two nulls, an 1D broad-band scheme can be designed using the NS24 scheme.

However, these dispersion characteristics are only limited to the 1D case. For multi-dimensional cases, the above schemes suffers from significant anisotropy. The reason is that the derivation of the frequency-optimized time and space increments did not consider the wave traveling along directions other than the principle axes. To mitigate the average dispersion error, values of the frequency-optimized increments might me slightly adjusted. Following this idea, an improved NSFD (INS) algorithm was presented by introducing extra free parameters into the frequency-optimized increments. This is equivalent to shifting the average dispersion values of the regular NSFD towards zero. The concept of the INS scheme was applied to both the (2,2) and (2,4) stencils to construct the INS22 and INS24 schemes. The values of these free parameters can be written in closed form. However,

a zero dispersion angle, which can only be found numerically, must be specified. A more straightforward approach was to use the least square method (LSM). A follow-up dispersion analysis indicated that the INS schemes did improve the dispersion in global sense near the design mesh resolution. However, for single-frequency, the local dispersion error still depends on the propagation angles. In other words, for certain directions, the regular NSFD methods could be more accurate than the proposed INS schemes. Numerical simulations, including cavity, radiation, and scattering problems, were presented using both the INS22 and INS24 schemes.

The INS scheme opened a door for further dispersion reduction which could be achieved by introducing more free parameters into the stencil. A generalized NSFD (GNS) was presented in this spirit. With the cost of the order-of-accuracy in the space stencil, the GNS schemes are more powerful in dispersion minimization. Two GNS24 schemes, one broad-band and one narrow-band, were presented. The coefficients of GNS schemes were solved using the LSM. It was found that the average dispersion errors of the broad-band GNS scheme are smaller than that of their standard counterparts. However, this scheme suffers from more anisotropy. The narrow-band scheme exhibits extremely low dispersion at the design mesh resolution regardless of the propagation angles. However, this excellent performance can only be achieved near the design mesh resolution. In order to conduct radiation/scattering simulations, Berenger's perfectly matched layer (PML) was examined for the schemes with extended four-point stencils. From the numerical experiments, it can be observed that Berenger's PML is able to effectively absorb the outgoing waves. Two simulations, a cavity and a four-element array, were performed using the GNS schemes, which verified the dispersion analysis. Moreover, it was found that the GNS schemes can be

used to further reduce the dispersion within certain angle ranges. Also, the extra anisotropy generated in a rectangular-meshing domain can be automatically compensated by the GNS schemes. Then, the successful application to a (2,6) stencil showed that the proposed procedure works equally well for more complex stencils.

After that, the stability conditions of the GNS24 schemes were derived using a complex-frequency analysis. Compared to their standard counterparts, the stability limits of the NSFD schemes are slightly perturbed. Furthermore, Gauss's Laws were examined for the above NSFD methods. It was proven that the Gauss's Law is satisfied if a cubic mesh is used. Using the standard finite difference, Gauss's Laws are conditionally satisfied for the rectangular mesh. The extra constraints will compromise the dispersion performance. However, using the nonstandard differentiation, Gauss's Laws are automatically satisfied. In the last part of this chapter, the error generated by the material discontinuities was investigated. Two conditions, one narrow-band and one broad-band, were proposed for the 1D dielectric interfaces. For the narrow-band condition, the simulation showed that the error generated by the discontinuity is significantly reduced for the design mesh resolution. For the broad-band condition, the fourth-order accuracy of the entire scheme is fully restored if a small time-step is used.

Chapter 4 examined an important EMC problem concerning the effects of passengers on the PED mutual coupling in a simplified Boeing 757 fuselage. The two antennas includes one monopole mounted on the exterior of the fuselage and the other in the interior. The "bodies" of the onboard passengers, which are highly lossy and dispersive, were simplified and modeled using salt water contained in sealed plastic tubes. The S-parameters were simulated using Yee's algorithm and measured in the Electro-Magnetic Anechoic Chamber.

Both the simulated and the measured results agree to each other very well. It was observed that many high-frequency resonances were significantly dampened due to the lossy behavior of the "human bodies". The presence of the passengers reduces the threats from the electromagnetic interference for the onboard system.

5.2. Future Work

The research of this project presented a successful approach to minimize the dispersion without significant modification of Yee's algorithm. Some useful recommendations for future developments are summarized in this section.

First of all, the NSFD methods presented in this report only achieve low dispersion near a design mesh resolution. Some of them, such as the GNS24-1 scheme, exhibit lower dispersion over the entire frequency band. However, the improvement is very limited. One of the most straightforward solutions is to consider even more complex stencils, such as the sixth-order stencils. Since more coefficients (degrees of freedom) are involved, the approach presented in this report can be readily extended to two, three or even more design mesh resolutions. By appropriately choosing these design mesh resolutions, a controllable broadband low-dispersion scheme can be expected.

Second, a more challenging problem is to derive the corresponding material interface conditions for the complex stencil. The dielectric interface conditions proposed in this project are limited to only 1D case. It is still necessary to derive proper interface conditions for multi-dimensional cases, where the reflection and transmission mechanisms are more complicated. Furthermore, there is still no practical PEC interface condition for extended stencils, which can handle complex 3D problems accurately with stability. The material

interface treatments for extended stencils still remain one of the most challenging problems in the FDTD area.

Finally, the NSFD methods discussed so far only considered simple materials. For complex materials, such as lossy, dispersive, and nonlinear materials, the approach introduced in this project cannot be directly applied. In [42], [43], Cole did some pioneering work in applying NSFD to complex material. However, they are still not practical. Moreover, Berenger's PML was not fully justified for the schemes using extended stencils. The larger noise basis generated at the air-PML interfaces could cause serious problems for late time. The development of the appropriate ABCs is still necessary.

REFERENCES

[1] A. Taflove, *Computational Electrodynamics: The Finite-Difference Time-Domain Method*. Boston, MA: Artech House, 1995.

[2] C. A. Balanis, *Advanced Engineering Electromagnetics*. New York: Wiley, 1989.

[3] D. M. Pozar, *Microwave Engineering*, 2nd ed. New York: Wiley, 1998.

[4] R. F. Harrington, *Field Computation by Moment Methods*. IEEE Press, 1993.

[5] J. Jin, *The Finite Element Method in Electromagnetics*. New York: Wiley, 2002.

[6] K. S. Yee, "Numerical solution of initial boundary value problems involving Maxwell's equations in isotropic media," *IEEE Antennas and Propagat. Soc. Int. Symposium*, vol. 14, no. 3, pp. 302–307, 1966.

[7] K. L. Shlager and J. B. Schneider, "A selective survey of the finite-difference time-domain literature," *IEEE Antennas Propagat. Magazine*, vol. 37, no. 4, pp. 39–56, 1995.

[8] J.-P. Berenger, "A perfectly matched layer for the absorption of electromagnetic waves," *J. Comput. Phys.*, vol. 114, no. 1, pp. 185–200, 1994.

[9] ——, "Three-dimensional perfectly matched layer for the absorption of electromagnetic waves," *J. Comput. Phys.*, vol. 127, pp. 363–379, 1996.

[10] M. N. O. Sadiku, *Numerical Techniques in Electromagnetics*. Boca Raton: CRC Press, 1992, pp. 179–204.

[11] K. S. Kunz and R. J. Luebbers, *The Finite Difference Time Domain Method for Electromagnetics*. Boca Raton, FL: CRC Press, 1993.

[12] W. Andrew, "Finite-difference time domain method for high frequency and long slot antennas," Ph.D. dissertation, Arizona State University, 1996.

[13] G. S. Smith, *An Introduction to Classical Electromagnetic Radiation*. Cambridge: Cambridge Univ. Press, 1997.

[14] S. Gedney, *Computational electromagnetics: the finite-difference time-domain*. Univ. of Kentucky: Lecture notes, 2003.

[15] J. Fang, "Time domain finite difference computation for Maxwell's equations," Ph.D. dissertation, University of California at Berkeley, Berkeley, CA, 1989.

[16] T. Deveze, L. Beaulie, and W. Tabbara, "An absorbing boundary conditon for the fourth order FDTD scheme," in *IEEE Antennas and Propagat. Soc. Int. Symposium*, July 1992, pp. 342–345.

[17] ——, "A fourth order scheme for the FDTD algorithm applied to Maxwell equations," in *IEEE Antennas and Propagat. Soc. Int. Symposium*, vol. 1, Chicago, IL, July 1992, pp. 346–349.

[18] T. Deveze, "High order F.D.T.D. algorithm to reduce numerical dispersion and staircasing," in *10th Annual Review of Progress in Applied Computational Electromagnetics*, vol. 2, Monterey, CA, Mar. 1994, pp. 61–68.

[19] C. W. Manry, S. L. Broschat, and J. B. Schneider, "Higher-order FDTD methods for large problems," *Appl. Comput. Electromagn. Soc. J.*, vol. 10, no. 2, pp. 17–29, 1995.

[20] B. Gustafsson and P. Olsson, "Fourth-order difference methods for hyperbolic ibvps," *J. Comput. Phys.*, vol. 117, pp. 300–317, Mar. 1995.

[21] G. Cohen and P. Joly, "Construction and analysis of fourth-order fintie difference schemes for the acoustic vave equations in nonhomogeneous media," *SIAM J. Numer. Anal.*, vol. 33, pp. 1266–1302, 1996.

[22] D. W. Zingg, "Higher-order finite-difference methods in computational electromagnetics," in *IEEE Antennas and Propagat. Soc. Int. Symposium*, vol. 1, Montréal, Canada, July 1997, pp. 110–113.

[23] I. Singer and E. Turkel, "High-order finite-difference methods for the helmholtz equation," *Comp. Methods Appl. Mech. Engrg.*, vol. 163, pp. 342–358, Sept. 1998.

[24] K. Lan, Y. Liu, and W. Lin, "A higher order (2,4) scheme for reducing dispersion in fdtd algorithm," *IEEE Trans. Electromagn. Compat.*, vol. 41, no. 2, pp. 160–165, May 1999.

[25] H. E. Abd El-Raouf, E. A. El-Diwani, A. E.-H. Ammar, and F. El-Hefnawi, "A low-dispersion 3-D second-order in time fourth-order in space FDTD scheme (M3d24)," *IEEE Trans. Antennas Propagat.*, vol. 52, no. 7, pp. 1638–1646, 2004.

[26] M. F. Hadi and M. Piket-May, "A modified FDTD (2,4) scheme for modeling electrically large structures with high-phase accuracy," *IEEE Trans. Antennas Propagat.*, vol. 45, no. 2, pp. 254–264, 1997.

[27] G. Hausmann and M. Piket-May, "FDTD M24 dispersion and stability in three dimensions," in *Proc. 14th Ann. Rev. Prog. Appl. Comput. Electromagn.*, Monterey, CA, Mar. 1998, pp. 82–89.

[28] A. Kumar, "Isotropic finite-differences," *J. Comput. Phys.*, vol. 201, pp. 109–118, Nov. 2004.

[29] J. L. Young, D. Gaitonde, and J. S. Shang, "Toward the construction of a fourth-order difference scheme for transient EM wave simulations: staggered grid approach," *IEEE Trans. Antennas Propagat.*, vol. 45, no. 11, pp. 1573–1580, Nov. 1997.

[30] A. Taflove, *Advances in Computational Eletrodynamics: The Finite-Difference Time-Domain Method*. MA: Artech House, 1998, ch. Higher-order methods, pp. 63–110.

[31] M. Aidam and P. Russer, "New high order time-stepping schemes for finite differences," in *Proc. 15th Ann. Rev. Prog. Appl. Comput. Electromagn.*, Monterey, CA, Mar. 1999, pp. 578–585.

[32] H. Spachmann, R. Schuhmann, and T.Weiland, "Higher order explicit time integration schemes for Maxwell's equations," *Int. J. Numer. Model.*, vol. 15, pp. 419–437, Sept. 2002.

[33] P. G. Petropoulos, "Phase error control for FD-TD methods of second and fourth order accuracy," *IEEE Trans. Antennas Propagat.*, vol. 42, no. 6, pp. 859–862, 1994.

[34] D. W. Zingg, *A review of higher-order and optimized finite-difference methods for simulating linear wave phenomena*. AIAA: Tech. Rep., 1997.

[35] Y. Liu, "Fourier analysis of numerical algorithms for maxwell equations," *J. Comput. Phys.*, vol. 124, pp. 396–406, Mar. 1996.

[36] K. Hwang and A. C. Cangellaris, "Computational efficiency of Fang's fourth-order FDTD schemes," *Electromagn.*, vol. 23, pp. 89–102, 2003.

[37] R. E. Mickens, *Nonstandard Finite Difference Models of Differential Equations*. Singapore: World Scientific, 1994.

[38] ——, *Applications of Nonstandard Finite Difference Schemes.* Singapore: World Scientific, 2000.

[39] ——, *Advances in the Applications of Nonstandard Finite Difference Schemes.* Singapore: World Scientific, 2005.

[40] J. B. Cole, "A high accuracy FDTD algorithm to solve microwave propagation and scattering problems on a coarse grid," *IEEE Trans. Microwave Theory Tech.*, vol. 43, no. 9, pp. 2053–2058, 1995.

[41] ——, "A high-accuracy realization of the Yee algorithm using non-standard finite differences," *IEEE Trans. Microwave Theory Tech.*, vol. 45, no. 6, pp. 991–996, 1997.

[42] ——, "High-accuracy yee algorithm based on nonstandard finite differences: new developments and verifications," *IEEE Trans. Antennas Propagat.*, vol. 50, pp. 1185–1191, Sept. 2002.

[43] ——, "High-accuracy fdtd solution of the absorbing wave equation, and conducting maxwell's equations based on a nonstandard finite-difference model," *IEEE Trans. Antennas Propagat.*, vol. 52, pp. 725–729, Mar. 2004.

[44] T. Kashiwa, H. Kudo, Y. Sendo, T. Ohtani, and Y. Kanai, "The phase velocity error and stability condition of the three-dimensional nonstandard fdtd method," *IEEE Trans. Magn.*, vol. 38, no. 2, pp. 661–664, Mar. 2002.

[45] T. Kashiwa, Y. Sendo, K. Taguchi, T. Ohtani, and Y. Kanai, "Phase velocity errors of the nonstandard fdtd method and comparison with high-accuracy fdtd methods," *IEEE Trans. Magn.*, vol. 39, no. 4, pp. 2125–2128, July 2003.

[46] N. V. Kantartzis and T. D. Tsiboukis, "A higher-order FDTD technique for the implementation of enhanced dispersionless perfectly matched layers combined with efficient absorbing boundary conditions," *IEEE Trans. Magn.*, vol. 34, no. 5, pp. 2736–2739, Sept. 1998.

[47] N. V. Kantartzis, J. S. Juntunen, and T. Tsiboukis, "An enhanced higher-order FDTD technique for the construction of efficient reflectionless PMLs in 3-D generalized curvilinear coordinates," in *IEEE Antennas and Propagat. Soc. Int. Symposium*, vol. 3, July 1999, pp. 1894–1897.

[48] N. V. Kantartzis, T. I. Kosmanis, and T. D. Tsiboukis, "Fully nonorthogonal higher-order accurate FDTD schemes for the systematic development of 3-d reflectionless

PMLs in general curvilinear coordinate systems," *IEEE Trans. Magn.*, vol. 36, pp. 912–916, July 2000.

[49] N. V. Kantartzis, T. I. Kosmanis, T. V. Yioultsis, and T. D. Tsiboukis, "A nonorthogonal higher-order wavelet-oriented FDTD technique for 3-D waveguide structures on generalised curvilinear grids," *IEEE Trans. Magn.*, vol. 37, no. 5, pp. 3264–3268, Sept. 2001.

[50] N. V. Kantartzis, T. T. Zygiridis, and T. D. Tsiboukis, "A nonstandard higher-order FDTD algorithm for 3-D arbitrarily and fractal-shaped antenna structures on general curvilinear lattices," *IEEE Trans. Magn.*, vol. 38, no. 2, pp. 737–7408, Mar. 2002.

[51] N. V. Kantartzis and T. D. Tsiboukis, "A higher-order nonstandard FDTD-PML method for the advanced modeling of complex EMC problems in generalized 3-D curvilinear coordinates," *IEEE Trans. Electromagn. Compat.*, vol. 46, no. 1, pp. 2–11, Feb. 2004.

[52] N. V. Kantartzis, T. D. Tsiboukis, and E. E. Kriezis, "A topologically consistent class of 3-D higher-order curvilinear FDTD schemes for dispersion-optimized EMC and material modeling," *J. Mat. Processing Technol.*, vol. 161, pp. 210–217, 2005.

[53] J. W. Nehrbass, J. O. Jevtic, and R. Lee, "Reducing the phase error for finite-difference methods without increasing the order," *IEEE Trans. Antennas Propagat.*, vol. 46, pp. 1194–1201, Aug. 1998.

[54] J. S. Juntunen and T. D. Tsiboukis, "Reduction of numerical dispersion in FDTD method through artificial anisotropy," vol. 48, pp. 582–588, Apr. 2000.

[55] K. Suzuki and T. Kashiwa, "Reducing the numerical dispersion in the FDTD analysis by modifying the speed of light," *Electron. Commun. Jpn.*, vol. 85, no. 2, pp. 61–69, 2002.

[56] S.Wang and F. L.Teixeira, "A three-dimensional angle-optimized finite-difference time domain algorithm," *IEEE Trans. Microwave Theory Tech.*, vol. 51, pp. 811–817, Mar. 2003.

[57] ——, "A finite-difference time-domain algorithm for arbitrary propagation angles," *IEEE Trans. Antennas Propagat.*, vol. 51, pp. 2456–2463, Sept. 2003.

[58] ——, "Dispersion-relation-preserving FDTD algorithms for largescale three-dimensional problems," *IEEE Trans. Antennas Propagat.*, vol. 51, pp. 1818–1828, Aug. 2003.

[59] ——, "Grid-dispersion error reduction for broadband fdtd electromagnetic simulations," *IEEE Trans. Magnetics.*, vol. 40, no. 2, pp. 1440–1443, Mar. 2003.

[60] T. T. Zygiridis and T. D. Tsiboukis, "A dispersion-reduction scheme for the higher order (2,4) FDTD method," *IEEE Trans. Magnetics.*, vol. 40, pp. 1464–1467, 2004.

[61] ——, "Low-dispersion algorithms based on the higher order (2,4) FDTD method," *IEEE Trans. Microwave Theory Tech.*, vol. 52, pp. 1321–1327, Apr. 2004.

[62] ——, "Higher-order finite-difference schemes with reduced dispersion errors for accurate time-domain electromagnetic simulations," *Int. J. Numer. Model*, vol. 17, pp. 461–486, 2004.

[63] ——, "Development of higher-order FDTD schemes with controllable dispersion error," *IEEE Trans. Antennas Propagat.*, vol. 53, pp. 2952–2960, Sept. 2005.

[64] ——, "Design of optimized FDTD schemes for the accurate solution of electromagnetic problems," *IEEE Trans. Magnetics.*, vol. 42, no. 4, pp. 811–814, Apr. 2006.

[65] G. Sun and C. W. Trueman, "Optimized finite-difference time-domain methods based on the (2,4) stencil," *IEEE Trans. Microwave Theory Tech.*, vol. 53, pp. 832–842, Mar. 2005.

[66] K. L. Shlager and J. B. Schneider, "Comparison of the dispersion properties of several low-dispersion finite-difference time-domain algorithms," *IEEE Trans. Antennas Propagat.*, vol. 51, pp. 642–653, Mar. 2003.

[67] ——, "Comparison of the dispersion properties of higher order FDTD schemes and equivalent-sized mrtd schemes," *IEEE Trans. Antennas Propagat.*, vol. 52, pp. 1095–1104, Apr. 2004.

[68] E. Turkel and A. Yefet, "On the construction of a high order difference scheme for complex domains in a cartesian grid," *Appl. Numer. Math.*, vol. 33, pp. 113–124, May 2000.

[69] H. M. Jurgens and D. W. Zingg, "Numerical solution of the time-domain Maxwell equations using high-accuracy finite-difference methods," *SIAM J. Sci. Comput.*, vol. 22, pp. 1675–1696, 2000.

[70] J. F. Nystrom, "Higher-order time-stable numerical boundary scheme for the temporally dependent Maxwell equations in two dimensions," *J. Comput. Phys.*, vol. 178, pp. 290–306, May 2002.

[71] J. Nordstrom and R. Gustafsson, "High order finite difference approximations of electromagnetic wave propagation close to material discontinuities," *J. Sci. Comput.*, vol. 18, pp. 215–234, Apr. 2003.

[72] S. V. Georgakopoulos, "Higher-order finite difference methods for electromagnetic radiation and penetration," Ph.D. dissertation, Arizona State University, Tempe, AZ, 2001.

[73] S. V. Georgakopoulos, R. A. Renaut, C. A. Balanis, and C. R. Birtcher, "A hybrid fourth-order FDTD utilizing a second-order FDTD subgrid," *IEEE Microwave Wireless Component Lett.*, vol. 11, pp. 462–464, Nov. 2001.

[74] S. V. Georgakopoulos, C. R. Birtcher, C. A. Balanis, and R. A. Renaut, "Higher order finite-difference schemes for electromagnetic radiation, scattering, and penetration, part I: Theory," *IEEE Antennas Propag. Mag.*, vol. 44, pp. 134–142, Apr. 2002.

[75] ——, "Higher order finite-difference schemes for electromagnetic radiation, scattering, and penetration, part II: Applications," *IEEE Antennas Propag. Mag.*, vol. 44, pp. 92–101, Apr. 2002.

[76] ——, "HIRF penetration and PED coupling analysis for scaled fuselage models using a hybrid subgrid FDTD(2,2)/FDTD(2,4) method," *IEEE Trans. Electromagn. Compat.*, vol. 45, pp. 293–305, May 2003.

[77] A. Yefet and P. G. Petropoulos, "A staggered fourth-order accurate explicit finite difference shceme for the time-domain Maxwell's equations," *J. Comput. Phys.*, vol. 168, pp. 286–315, Apr. 2001.

[78] A. Ditkowski, K. Dridi, and J. S. Hesthaven, "Convergent cartesian grid methods for Maxwell's equations in complex geometries," *J. Comput. Phys.*, vol. 170, pp. 39–80, June 2001.

[79] T. A. Driscoll and B. Fornberg, "A block pseudospectral method for Maxwell's equations: I. one dimensional case," *J. Comput. Phys.*, vol. 140, pp. 47–65, 1998.

[80] ——, "Block pseudospectral methods for Maxwell's equations: II. two-dimensional, discontinuous-coefficient case," *SIAM J. Sci. Comput.*, vol. 21, pp. 1146–1167, 1999.

[81] S. Zhao and G. W. Wei, "Higher-order FDTD methods via derivative matching for Maxwell's equations with material interfaces," *J. Comput. Phys.*, vol. 200, pp. 60–103, Oct. 2004.

[82] A. Christ, J. Frohlich, and N. Kuster, "Correction of numerical phase velocity erros in nonuniform FDTD meshes," *IEICE Trans. Commun.*, vol. E85-B, pp. 2904–2915, Dec. 2002.

[83] A. Christ and N. Kuster, "Correction of the numerical reflection coefficient of the finite-difference time-domain method for efficient simulation of vertical-cavity surface-emitting lasers," *Journal of Optical Society of America B*, vol. 20, pp. 1401–1408, July 2003.

[84] A. Christ, S. Benkler, J. Frohilich, and N. Kuster, "Analysis of the accuracy of the numerical reflection coefficient of the finite-difference time-domain method at planar material interfaces," *IEEE Trans. Antennas Propagat.*, vol. 48, pp. 264–272, May 2006.

[85] J. S. Hesthaven, "High-order accurate methods in time-domain computational electromagnetics, a review," *Adv. Imag. Electron. Phys.*, vol. 127, p. 59, 2003.

[86] N. V. Kantartzis and T. D. Tsiboukis, *Higher Order FDTD Schemes for Waveguide and Antenna Structures*. Morgan and Claypool, 2006.

[87] R. J. LeVeque, *Finite Difference Methods for Differential Equations*. http://www.amath.washington.edu/ rjl/booksnotes.html: Unpublished lecture notes, 1998.

[88] G. D. Smith, *Numerical Solution of Partial Differential Equations: Finite Difference Methods*. Oxford, 1985.

[89] W. H. Press, S. A. Teukolsky, and et al., *Numerical Recipes in C: The Art of Scientific Computing*, 2nd ed. Cambridge University Press, 1992.

[90] B. Yang and C. A. Balanis, "Higher-order (2,4) nonstandard finite difference scheme to improve anisotropy," in *IEEE Antennas and Propagat. Soc. Int. Symposium*, vol. 2, Washington, DC, July 2005, pp. 1239–1242.

[91] ——, "An isotropy-improved nonstandard finite-difference time domain method," *IEEE Trans. Antennas Propagat.*, vol. 54, pp. 1935–1942, July 2006.

[92] G. A. F. Seber and C. J. Wild, *Nonlinear Regression*. Wiley, 1989.

[93] B. Yang and C. A. Balanis, "Least square method to optimize the coefficients of complex finite-difference space stencils," *IEEE Antenna Wireless Progagat. Lett.*, vol. 5, pp. 450–453, Dec. 2006.

[94] T. G. Moore, J. G. Blaschak, A. Taflove, and G. A. Kriegsmann, "Theory and application of radiation boundary operators," *IEEE Trans. Antennas Propagat.*, vol. 36, no. 6, pp. 1797–1812, Dec. 1988.

[95] W. V. Andrew, C. A. Balanis, and P. A. Tirkas, "A comparison of the Berenger perfectly matched layer and the Lindman higher-order ABC's for the FDTD method," *IEEE Microwave Guided Wave Lett.*, vol. 5, no. 6, pp. 192–194, 1995.

[96] A. R. Ruddie, "Measured impact of seats and glazing on the coupling of electromagnetic fields into vehicles and their wiring harnessses," in *15th international Zurich EMC Symposium*, 2003.

[97] C. Gabriel, *Compilation of the Dielectric Properties of Body Tissues at RF and Microwave Frequencies.* http://www.brooks.af.mil/AFRL/HED/hedr/reports/dielectric/home.html.

[98] *HP 85070B dielectric probe kit.* User's Manual, Hewlett Packard Inc.

BIOGRAPHICAL SKETCH

Bo Yang was born in Suzhou, Jiangsu, China, P. R. in Feb. 1977. He received his B.S. and M.S. degrees in Radio Engineering from Southeast University, Nanjing, China, P. R., in 1999 and 2002. He is currently pursuing the Ph.D. degree in the Advanced Helicopter Electromagnetic Lab of Arizona State University, Tempe, AZ.

JOURNAL PUBLICATIONS

1. B. Yang and C. A. Balanis, "An isotropy-improved nonstandard finite-difference time domain method," *IEEE Trans. Antennas Propagat*, vol. 54, pp. 1935-1942, Jul., 2006.

2. B. Yang and C. A. Balanis, "Least square method to optimize the complex finite-difference space stencils," *IEEE Antenna and Wireless Propagation Letters*, vol. 5, No. 1, pp. 450-453, Dec, 2006.

3. B. Yang and C. A. Balanis, "Divergence properties of the nonstandard finite difference method," *IEEE Microwave and Wireless Components Letters*, vol. 17, no. 2, pp. 88-90, Feb. 2007.

4. B. Yang, C. R. Birtcher, and C. A. Balanis, "The effects of passengers on PED mutual coupling in a simplified fuselage: simulations and measurements." *IEEE Trans. Electromagn. Compat.*, submitted.

5. B. Yang and C. A. Balanis, "Dielectric interface conditions for the general fourth-order finite difference," *IEEE Microwave and Wireless Components Letters*, submitted.